UNIVERSITY OF OSLO
Department of Geosciences
MetOs section

Impacts of fine scale variability on large scale atmospheric chemistry

Master thesis in Geosciences Meteorology and oceanography

Øivind Hodnebrog

02.06.2008

Abstract

The effect of tropospheric ozone as an air pollutant is normally simulated using regional or urban scale computer models, while global models often are used to study the role of ozone as a greenhouse gas. The chemical transformations involved in the ozone chemistry occur on all scales, and are often related nonlinearily to each other. Due to the relatively coarse spatial resolution used in global Chemistry-Transport Models (CTMs), inaccuracies will arise when emissions and chemical processes are averaged in a grid box. Additionally, meteorological small-scale processes (e.g. convection) impact the chemistry, and inaccuracies may increase if parameterizations are implemented on a coarse scale. The problem of neglecting urban scale processes is particularly important in climate studies because of the rapid urbanization that we experience today.

In this thesis we have applied the WRF-Chem (Weather Research and Forecasting with Chemistry) model to study scale interactions in the ozone photochemistry, and to quantify inaccuracies in terms of effective emissions. The model is run for a three week summer period in 2003 over Europe, zooming in on the London metropolitan area using square horizontal grid resolutions of 81 km, 27 km, 9 km, 3 km, and 1 km. We use the RADM2 chemistry scheme, and as input data we apply a 1 km $\times$ 1 km anthropogenic emission inventory for the UK (DEFRA, 2007), and a $0.5^\circ \times 0.5^\circ$ anthropogenic emission inventory for the rest of Europe (RETRO, 2006), together with assimilated meteorology from ECMWF as initial and boundary conditions. We have focused on column values of ozone and related chemical components in the London area, caused by London emissions, and results from the different resolutions have been compared.

The results show an increase in the average net ozone column caused by London emissions when horizontal grid spacing is reduced from 81 km to 27 km. Most likely, these changes are caused by increased transport of chemical species out of the London area due to better representation of winds and boundary layer height in the latter case. There were only minor changes in the results between the scales 27 km, 9 km, and 3 km, while the 1 km resolution results gave an increase in ozone column values due to London emissions, causing a shift from net negative to net positive ozone in the London area. The changes from 3 km to 1 km probably arise because of higher resolution in emissions, so that the model better accounts for nonlinearities in the ozone chemistry. However, comparisons with measurements of chemical species show that there are uncertainties related to our results, implying that caution should be used when drawing conclusions. The agreement between model results and measurements were relatively good in the first half of the simulation period, but lack of vertical distribution in the emissions data caused large discrepancies during the last ten days.

Acknowledgements

First of all I would like to thank my supervisor, Professor Frode Stordal, for his excellent guidance during the work on my thesis. I would also like to thank my co-supervisor, Terje Berntsen, for valuable discussions, especially regarding the analysis of the results.

At the MetOs section there are many incredibly helpful people who have contributed to this study in one way or another. In particular I would like to mention Gunnar Wollan for help on Fortran and setting up the WRF model, Stig B. Dalsøren for answering all my emissions-related questions, and Erik Nordborg for introducing me to the WRF model. Many thanks to Bjørn Egil Nygaard as well (now at the Meteorological Institute), for fabulous help with Matlab and WRF. My fellow students have contributed both intellectually and socially through many nice chats and fun social events.

My friends and family also deserve thanks for their support and encouragement, and to be there for me when I needed a break from studying. Last but not least, thanks to Siri for proofreading, and especially for listening to my complaints during times of frustration.

Oslo, June 2, 2008
Øivind Hodnebrog

Contents

Chapter 1

Introduction

In addition to the large increase in the world's population during the last century, there has also been rapid urbanization throughout the globe. According to UN (2006), 13 percent of the world's population lived in cities in 1900, and in 2005 this number was 49 percent. Future projections confirm this trend and predict an increase to 60 percent by 2030. The increase in population leads to an increase in the amount of energy consumed and thus more fossil fuel combustion. Nitrogen oxides and hydrocarbons are some of the compounds emitted from e.g. power plants and the transport sector, and they are the most important precursors to ozone formation in the troposphere. Especially in urban areas, the concentrations of pollutants resulting from anthropogenic emissions may become very large and this could be a threat to human health.

While ozone abundance in the stratosphere is favourable, ozone in near-surface air has several negative impacts. High values of ozone are harmful for humans, animals, and vegetation, but also important is the role of tropospheric ozone as a greenhouse gas. According to the latest climate change report from IPCC (2007), anthropogenic ozone in the troposphere contribute approximately 0.35 W m^{-2} to the net radiative forcing (Figure 1.1). However, there are uncertainties related to this value, especially because of the short lifetime of ozone and the complex photochemical reactions involved during tropospheric ozone formation and destruction. Another important aspect of ozone as a greenhouse gas is its ability to cause regional forcing, and hence regional climate change. Long-lived greenhouse gases, e.g. CO_2 and CH_4, are well-mixed and do not cause regional forcing.

Numerical computer models have been developed in order to simulate the atmosphere and all of its meteorological and chemical processes. Most of these models divide the atmosphere into grid boxes and complex equations are solved for each box. To get the most realistic picture of the state of the atmosphere at a given time, an infinite amount of grid boxes would be needed in order to resolve processes on all scales. Since the amount of computer power is limited, however, modelers use a coarser partitioning of the

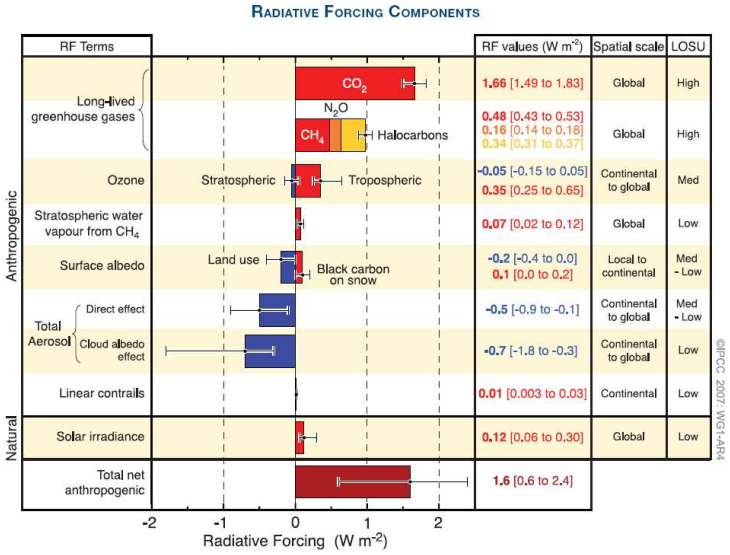

Figure 1.1: *Global average radiative forcing estimates and ranges in 2005 (IPCC, 2007).*

model domain and they parameterize the processes occuring on scales smaller than the size of a grid box. When distributions and changes in tropospheric ozone are calculated on a global scale, Chemistry-Transport Models (CTMs) are normally used. Usually, the CTMs have rather coarse resolution, e.g. is the T42 resolution ($2.8° \times 2.8°$) frequently used in climate studies.

In a numerical grid box model, differential equations have to be approximated by finite difference equations in order to solve the equations describing the atmospheric motions. These difference equations only describe the processes that occur on scales larger than twice the grid length, and ignore all subgrid scale processes. Even though parameterizations are made to partially correct this problem, errors increase with coarser resolution. Coarser spatial resolution is usually associated with a longer time step, and hence coarser temporal resolution. This could also contribute to errors.

When it comes to photochemistry and emissions, there will be errors when values are averaged over a grid box. Additionally, photochemical production of ozone is to a large extent related nonlinearly to its precursors. Meteorological factors are also important; for instance is water vapor fundamental in producing hydroxyl radical (OH), the number one scavenger of the atmosphere. Cloud cover is another important meteorological factor, mainly because it controls the amount of sunlight available for subcloud photochemical reactions. Accordingly, inclusion of subgrid scale processes is important in coarse resolution models.

1.1 Background

Gillani and Pleim (1996) addressed the issue of subgrid scale effects in regional models, and concluded that there are important differences in concentrations of ozone and related chemical species when inhomogeneities are represented more accurately with higher resolution. The concept of effective emissions were introduced by Petry et al. (1998). They used a one-dimensional box model representative for mesoscale volume and three different plume models to estimate the chemical conversion of emissions from a subsonic aircraft. Transformation of NO_x emissions into reservoir species, mainly HNO_3 and HNO_4, and production of ozone were studied. Then, effective emission indices were calculated to correct expanding plume effects in global or mesoscale models. They found that when aircraft emissions were instantaneously mixed in the box model, ozone perturbations were overestimated compared to the time evolution of ozone calculated with a plume model.

Similar to Petry et al. (1998), Kraabøl et al. (2000a) also studied the impact of NO_x emissions from subsonic aircraft, but they used a three-dimensional model covering Europe, North America, and the North Atlantic. CTM simulations were made both with and without considering plume chemistry from an aircraft plume model. The chemical conversion of NO_x to reservoir species was calculated as a function of time of emission, latitude, and background concentration of ozone and NO_x under summer conditions. When NO_x emissions from the aircraft were instantaneously mixed over the model grid area, monthly averaged NO_x were found to increase by up to 70 parts per trillion over the midwest United States and over England in July 1998. Monthly averaged NO_x contribution from aircraft was reduced by $\sim$ 40 % or less when plume processes were taken into account. The increase in ozone concentration when NO_x emissions were instantaneously mixed, was lowered by up to $\sim$ 30 % when plume processes were considered.

In Kraabøl et al. (2002), the impact of NO_x emissions from subsonic aircraft were studied for a global three-dimensional chemistry transport model, including plume processes. The modified emissions now varied as a function of time of day of emissions, latitude, season, temperature, atmospheric turbulence and background concentrations of NO_x and ozone. Similar to Kraabøl et al. (2000a), it was found that the use of modified aircraft emissions had a significant influence on the estimated NO_x and ozone increases. Kraabøl et al. (2002) calculated a 25-35 % decrease in NO_x perturbations over the eastern U.S., the North Atlantic Ocean, and Europe, compared with an unmodified NO_x emission from aircraft. For ozone, the corresponding decrease in perturbation was 15-18 % at northern middle and high latitudes.

When an aircraft exhaust plume is released, the chemical conversions take place at different rates depending on the distance from the core of the plume.

Kraabøl et al. (2000b) and Kraabøl and Stordal (2000) have studied this effect by applying a model containing several circular or cylindrical layers. Model results were compared to observations of NO, HNO_3, HNO_2 and CO_2, and these were in broad agreement. When sensitivity tests were performed at 50°N under summer conditions, it was found that the rate of chemical conversion of NO_x to reservoir species was highly dependent on the number of sunlight hours. Also, different levels of ozone and NO_x in the background atmosphere had a strong influence on the NO_x conversion rate.

The articles presented above discuss the impact of NO_x emissions from aircrafts. Similarly, emissions from other local sources, such as ships, highways or large industrial factories, are also often implemented as homogenously distributed emissions in a global chemistry model. A more recent study is Cohan et al. (2006) who have focused on differences in ground-level ozone concentrations due to changes in grid resolution of a regional air quality model. Ozone sensitivity to NO_x emissions from both an urban area (the Atlanta region) and a large point source (Scherer power plant) are considered. For all cases examined in the study, finer grid scales better resolve the texture of small-scale inhomogeneities in ozone response. However, the authors suggest that model error for simulating regional ozone formation is driven by factors other than grid resolution, at least over the range of resolutions considered in the study (36 km, 12 km, and 4 km).

Calbó et al. (1998) have derived a computationally efficient parameterization of urban subgrid scale processes in global atmospheric chemistry models, based on results from an urban chemistry model. Compared to our study, they have taken more of a mathematical approach using probability density functions to approximate the response of the urban model to its input. Some of the input values include time of year, latitude, cloud cover, boundary layer height, and emission data, while effective emissions are output from the parameterization. According to the authors, comparisons between parameterization and urban model results show generally good correlations.

Results from a reduced-form urban air chemistry model have been incorporated in a chemistry-climate model in Mayer et al. (2000). The reduced-form urban air model is derived using a method similar to the one described in Calbó et al. (1998). Simulations were carried out for the time period from 1977 to 2100, both with and without including the reduced-form urban model. When urban subgrid scale processes were included in the climate model, the authors found that more ozone was produced in urban domains, but global tropospheric NO_x, O_3, and OH concentrations were lower than without considering plume scale chemistry. There were only small changes in the overall radiative forcing, however, because the predicted decrease in O_3 was offset by an increase in CH_4. These results show that subgrid scale effects in an urban area do impact chemistry on regional and global scales, and suggest that further investigation of these effects is meaningful.

1.2 Description of this study

The purpose of this study is to apply a computer model which can resolve fine-scale processes, WRF-Chem[1], and estimate factors that correct the errors that arise when emissions and meteorological processes are averaged over a grid box in a regional or global model. These correction factors will later be used to estimate effective emissions for use in Oslo-CTM2. Oslo-CTM2 is a three-dimensional global chemical transport model developed at the University of Oslo, and is continuously being used to study chemistry in both the troposphere and the stratosphere (Berntsen and Isaksen (1997), Gauss et al. (2003), Søvde et al. (2008)).

Calculations of ozone formation from the ozone precursors, NO_x, CO, and VOC, will be performed using results from a fine-scale WRF-Chem simulation. The results will then be compared to a simulation with coarser grid, and differences will be studied and quantified in terms of preliminary effective emission factors. These factors will include the impacts of processes on subgrid scales, taking into account e.g. transformation of NO_x to reservoir species and formation of ozone that take place on smaller scales before diluted and transported to larger scales.

This method of calculating effective emissions that include plume scale processes is much like the previous studies of aircraft emissions described in Section 1.1. The main difference between the aircraft studies and this study is that we quantify the effect of emissions from an urban area instead of only aircraft emissions. Even though the problem at hand is somewhat similar, there are additional factors that have to be taken into account in our study. For instance are hydrocarbons more important for ozone production over an urban area at ground level. Also, cloud cover and both wet and dry deposition could play an important role for ozone abundance near the surface.

In the next chapter (Chapter 2) we describe atmospheric processes that may lead to subgrid scale effects, while Chapter 3 gives a description of the WRF-Chem model and our input data. In Chapter 4 our results are presented and discussed, in addition to proposals for further research. Finally, summary and conclusions are given in Chapter 5.

[1]Description of the model is given in Chapter 3

Chapter 2

Theory

Processes in the atmosphere, both meteorological and chemical, occur on many different spatial and temporal scales. Figure 2.1 shows examples of processes taking place on scales ranging from the size of a molecule to the size of the globe. As already mentioned, coarse-resolution numerical models average processes occuring on scales less than approximately the size of a grid box. In this chapter, subgrid scale processes that are important for ozone formation and destruction will be described, while processes occuring on larger scales will be given less attention. The theory presented here is mainly based on Jacobson (2005), Jacob (1999), and Stordal and Hov (1993).

2.1 Atmospheric processes

When chemical species are emitted from various sources there are several processes that influence its distribution over time. Figure 2.2 shows examples of emissions from a smokestack and an automobile, and the dispersion due to advection. The emissions are further subject to chemical transformations and deposition. In the atmosphere, the processes controlling the abundance of chemical species can be divided into four categories:

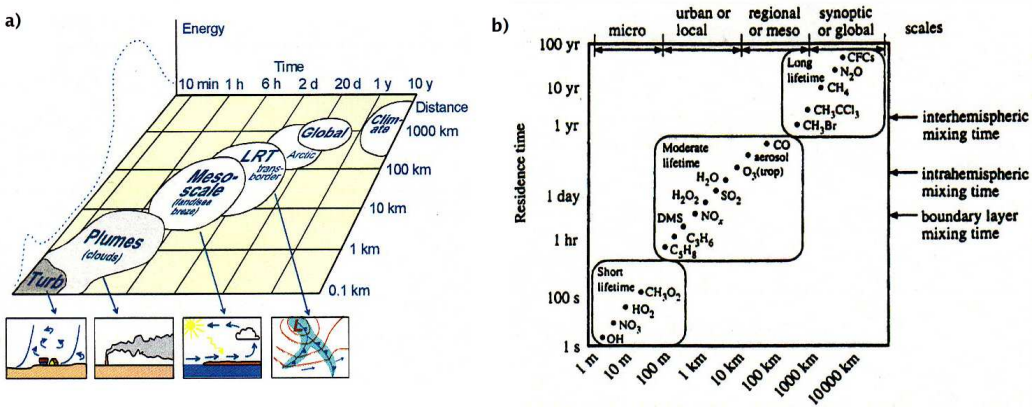

Figure 2.1: *Different spatial and temporal scales for (a) meteorological processes (Hov, 2007) and (b) chemical components (Junge, 1963).*

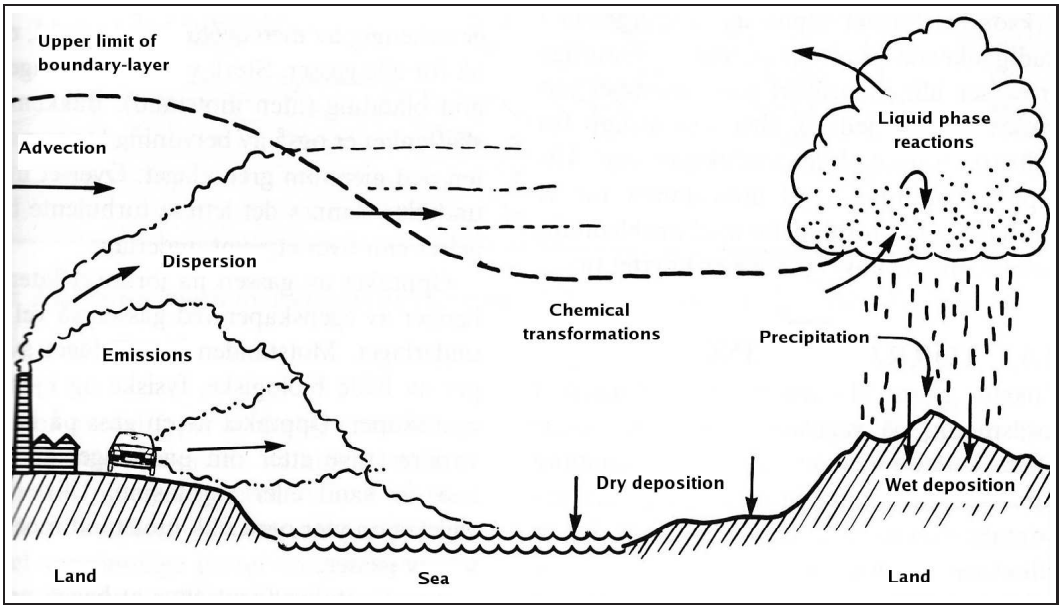

Figure 2.2: *The different processes influencing the life cycle of a tracer in the atmosphere (modified from Stordal and Hov (1993)).*

- **Emissions**. There are three types of emission sources in the atmosphere: anthropogenic (e.g. fossil fuel combustion), biogenic (e.g. photosynthesis), and non-biogenic (e.g. volcanoes). Usually, molecules are released from sources near the ground, but some sources are elevated (e.g. aircrafts and lightning).

- **Chemistry**. Chemical reactions in the atmosphere result in production and loss of species. In the context of this study, the most important types of reactions are bimolecular reactions, termolecular reactions, and photolysis.

- **Transport**. Atmospheric motions result in transport of species away from their sources. Three types of transport are advection, turbulence or convection. The latter two forms occur on small spatial and temporal scales and are therefore essential in this study.

- **Deposition**. There are two types of deposition: dry deposition and wet deposition. In particular, wet deposition is important because it is a rapid process that occur on small spatial scales.

Numerical models that divide the atmosphere into grid boxes are called Eulerian models. In such a model, the rate of change with time in the abundance of a chemical species within a grid box must equal the difference between sources and sinks. If c is the concentration of a chemical species, the rate of change of c with time may be written

$$\frac{dc}{dt} = \sum \text{sources} - \sum \text{sinks} = E + P + F_{in} - L - D - F_{out} \qquad (2.1)$$

where E is emissions, P is chemical production, L is chemical loss, D is deposition, and the terms F_{in} and F_{out} refer to the flow of the species into and out of the grid box, respectively, due to transport.

The atmospheric lifetime τ of a species is the average time it takes for a molecule to decrease by a factor $1/e$ and is hence referred to as an "e-folding time". τ is useful for measuring the time it takes for a system to reach steady state. Following the notation above, τ may be calculated as

$$\tau = \frac{c}{\sum \text{sinks}} = \frac{c}{F_{out} + L + D} = \frac{1}{k} \tag{2.2}$$

where k is the overall rate constant for the loss processes.

2.2 Urban photochemistry

Ozone is an important greenhouse gas in the troposphere and its abundance is harmful to humans, animals and vegetation when exposed to large quantities. For these reasons, and because ozone is an indicator of the abundance of other pollutants, ozone is the most recognized gas-phase product of photochemical smog reactions. As will be shown in the following text, ozone in the troposphere is produced from the oxidation of carbon monoxide and volatile organic compounds by OH when NO_x is present. In regions where there are large emissions of ozone precursors, especially in urban areas, high concentrations of ozone could lead to an air pollution problem. Since the reactions producing ozone are rapid, nonlinear, and occur on small spatial scales, coarse-resolution models are not able to simulate these high concentrations accurately.

From Figure 2.3 we see an increase in NO_x, CO, and O_3 concentrations in most of the troposphere since preindustrial times. The latitudinal distributions reflect the largest anthropogenic emissions near the ground in the northern hemisphere. In most of the troposphere, concentrations of NO_x, CO, and O_3 have increased by factors of 2-8, 3-4, and 1.5-2, respectively. Changes in OH concentrations, however, are more difficult to predict, but according to the model results the net effect of human activity was to increase OH in most of the lower troposphere and to decrease OH elsewhere.

2.2.1 Hydroxyl radical (OH)

The hydroxyl radical is a so-called free radical because it has one unpaired electron. This property makes it highly reactive and it breaks down many other gases in the atmosphere, hence it is referred to as a scavenger. OH is not emitted into the atmosphere, but forms chemically. In the free-troposphere the main source of OH is

$$O(^1D) + H_2O \rightarrow 2OH \tag{2.3}$$

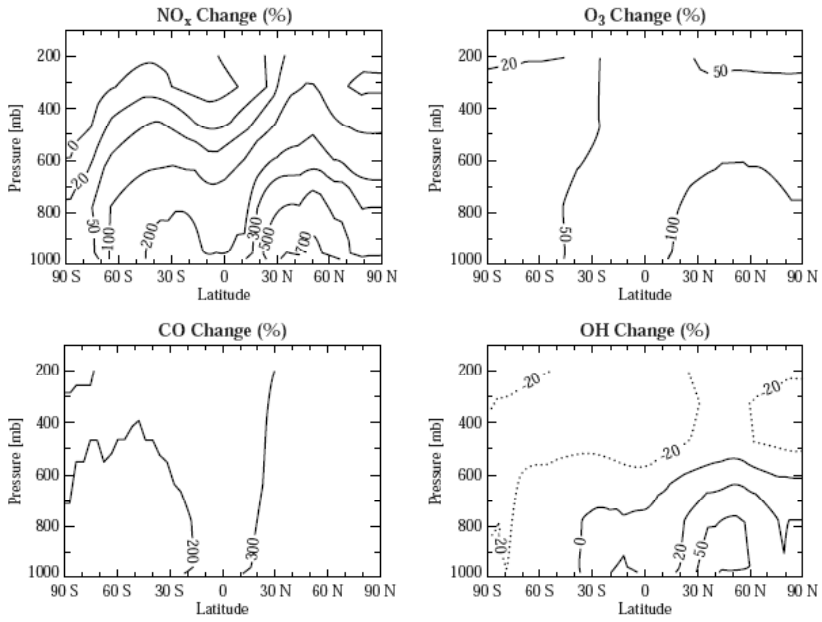

Figure 2.3: *Global tropospheric chemistry model simulation that shows the relative increases of NO_x, CO, O_3, and OH concentrations from preindustrial times to year 1999 (Jacob, 1999).*

In urban air there are three major reaction mechanisms that produce OH: photolysis of HNO_2, aldehyde photolysis and oxidation, and ozone photolysis. Since photolysis is required for all sources of OH, and its lifetime against chemical destruction is less than a second, OH only exists during the day.

2.2.2 Carbon Monoxide (CO)

The abundance of carbon monoxide in the free troposphere enhances ozone production, but CO is also an important pollutant itself. Mainly, there are three types of processes controlling the abundance of CO in the troposphere; emissions, chemical loss and transport. CO has a chemical lifetime of about two months, which is long enough for contribution to both regional and global air pollution. Additionally, CO is directly emitted from surface sources and this has a great impact on the abundance, especially in urban areas where emissions are large.

When there is an excess of carbon during combustion, CO is formed in preference of CO_2. Table 2.1 shows that most of the CO emitted into the troposphere is anthropogenic, and its largest emission sources are fossil fuel combustion and biomass burning. There are also biogenic emissions of CO from vegetation and oceans, but these are minor compared to the anthropogenic emissions.

	Range of estimates (Tg(CO) yr^{-1})
Sources	**1800-2700**
Fossil fuel combustion /industry	300-550
Biomass burning	300-700
Vegetation	60-160
Oceans	20-200
Oxidation of methane	400-1000
Oxidation of other hydrocarbons	200-600
Sinks	**2100-3000**
Tropospheric oxidation by OH	1400-2600
Stratosphere	∼100
Soil uptake	250-640

Table 2.1: *Global budget of CO (Jacob, 1999).*

Oxidation of methane and other hydrocarbons are large chemical sources of CO. The most important sink is tropospheric oxidation by OH, and together with methane, CO is a principal sink for OH. Soil uptake and transport to the stratosphere also act as sinks in the CO budget.

Tropospheric oxidation by OH gives CO a mean lifetime of approximately 2 months. CO is not well-mixed in the troposphere due to this relatively short lifetime, and mixing ratios range from 50-150 ppbv[1] in remote regions to several ppmv[2] in urban areas. Figure 2.3 shows that CO has increased the most in the lower troposphere and in the northern hemisphere due to increased emissions in these regions.

When CO is oxidized by OH and NO_x is present, this leads to ozone production by the cycle

$$CO + OH \rightarrow CO_2 + H \tag{2.4}$$

$$H + O_2 \xrightarrow{M} HO_2 \tag{2.5}$$

$$NO + HO_2 \rightarrow NO_2 + OH \tag{2.6}$$

$$NO_2 + h\nu \rightarrow NO + O \qquad \lambda < 420 \text{ nm} \tag{2.7}$$

$$O + O_2 + M \rightarrow O_3 + M \tag{2.8}$$

$$\text{Net: } CO + 2O_2 + h\nu \rightarrow CO_2 + O_3 \tag{2.9}$$

As seen from the net reaction above, one O_3 molecule and one CO_2 molecule are produced for each CO molecule oxidized by OH.

	Source, Tg N yr^{-1}
Fossil fuel combustion	21
Biomass burning	12
Soils	6
Lightning	3
NH_3 oxidation	3
Aircraft	0.5
Transport from stratosphere	0.1

Table 2.2: *Estimated sources of tropospheric NO_x (Jacob, 1999).*

2.2.3 Nitrogen Oxides (NO_x)

NO_x consists of NO + NO_2 and is a principal precursor to ozone. The processes controlling its distribution are chemistry, transport and emission. NO_x has a chemical lifetime of only 1-2 days at the surface, so its distribution is controlled largely by emissions. This is confirmed by Figure 2.3 where the largest increase in NO_x concentrations are located close to the sources of large anthropogenic emissions.

Nitrogen oxide is formed when oxygen molecules in the air are heated to high temperatures, then decomposed, and subsequently react with molecular nitrogen. This explains why fossil fuel combustion, biomass burning, and lightning are major sources of NO_x in the troposphere, as shown in Table 2.2. Fossil fuel combustion and biomass burning combined account for more than 70 percent of the global NO_x sources, reflecting the large human contribution to the NO_x budget. Emissions from the surface are clearly the largest source, but some NO_x is generated in situ in the atmosphere (e.g. lightning).

Most of the nitrogen oxides are emitted as NO, but there is a rapid cycling between NO and NO_2 by the reactions

$$NO + O_3 \rightarrow NO_2 + O_2 \tag{2.10}$$

$$NO_2 + h\nu \xrightarrow{O_2} NO + O_3 \tag{2.11}$$

and the daytime cycle

$$HO_2 + NO \rightarrow OH + NO_2 \tag{2.12}$$

$$NO_2 + h\nu \xrightarrow{O_2} NO + O_3 \tag{2.13}$$

which has a time scale of only a minute. At night, Reaction (2.11/2.13) ceases and NO_x is only present as NO_2 because of (2.10).

[1] ppbv = parts per billion volume
[2] ppmv = parts per million volume

	Gg yr^{-1}
Stationary Combustion	67
Road Transport	119
Transport	31
Extraction & Distribution of Fossil Fuels	201
Production Processes	65
Processes in wood, paper pulp, food, drink industries	79
Solvent & Other Product use	398
Agriculture / Waste	18
Total	**977**
Natural Emissions (forests and accidental biomass fires)	92

Table 2.3: *UK emissions of NMVOCs for the year 2005 (Dore et al., 2007).*

Sinks of NO_x include dry deposition of NO_2, and reaction between NO_2 and OH:

$$NO_2 + OH + M \rightarrow HNO_3 + M \tag{2.14}$$

which is the most important sink. In the stratosphere, nitric acid (HNO_3) is converted back to NO_2, however, this is not the case in the troposphere. Nitric acid is highly soluble in water and is therefore removed from the troposphere by wet deposition (see Section 2.3.5). Still, the lifetime of NO_x against wet deposition can be a few days and hence represents both a local and regional air pollution problem.

2.2.4 Volatile Organic Compound (VOC)

Volatile Organic Compounds include hydrocarbons and many other carbon-based molecules. According to the definition, methane is included in VOC. Methane contributes to ozone formation, but this is on a global scale rather than on local or regional scales. For this reason, methane is of minor importance in this study and we will therefore focus on the Non-Methane Volatile Organic Compounds (NMVOCs).

The least reactive NMVOCs have a lifetime of several days and may be important in regional air pollution. However, most high-molecular-weight organic gases have a lifetime of only a few hours to a few days, so they are broken down before they reach the free troposphere. In urban areas, NMVOCs are close to the emission sources and contribute to ozone formation when NO_x is present.

In Table 2.3, UK emission sources of NMVOC are given for the year 2005. The largest anthropogenic sources include emissions from the transport sector, other fossil fuel combustion, and solvent use. On a global scale, biogenic

	Tg O_3/yr
Sources	3400-5700
Chemical production	3000-4600
HO_2+NO	(70 %)
CH_3O_2+NO	(20 %)
RO_2+NO	(10 %)
Transport from stratosphere	400-1100
Sinks	3400-5700
Chemical loss	3000-4200
$O(^1D)$+H_2O	(40 %)
HO_2+O_3	(40 %)
OH+O_3	(10 %)
others	(10 %)
Dry deposition	500-1500

Table 2.4: *Global budget of tropospheric O_3 (Jacob, 1999).*

emissions are important as well; isoprene which is a by-product of photosynthesis contributes considerably to ozone production. According to Jacob (1999), isoprene emissions in the United States are larger than the sum of all anthropogenic hydrocarbon emissions.

There are six major processes that break down NMVOCs: photolysis and reaction with OH, HO_2, O, NO_3, and O_3. OH and O are present during the day only, while NO_3 is present only during the night. The breakdown of NMVOCs produces free radicals that lead to ozone formation, but the amount of ozone produced from each compound is quite variable. Alkanes are often emitted in relatively large amounts in urban air, but the reactivity in producing ozone is low (Geng et al., 2007). More important than alkanes, with respect to ozone formation, are aromatics, alkenes, and ethenes.

2.2.5 Ozone (O_3)

Ozone is a toxic gas and its abundance strongly depends on the concentrations of ozone precursors. It is not emitted directly but is produced chemically in the atmosphere and thus called a secondary pollutant. In the tropospere, O_3 is an important greenhouse gas that has the ability to cause regional radiative forcing. As indicated in Figure 2.3, ozone is not well-mixed in the troposphere. The inhomogenous distribution in the change of O_3 concentration is a result of large anthropogenic emissions of ozone precursors. Concentrations of ozone in clean surface air range from 5 to 30 ppbv, but may exceed 100 ppbv in urban air.

A major difficulty in modeling tropospheric ozone is the complexity and nonlinearity involved in its production and destruction. An increased amount

of ozone precursors does not necessarily lead to increased levels of ozone. In addition, NO_x and some hydrocarbons can be transported hundreds of kilometers away from their origin before they are involved in ozone production. For this reason, and because ozone may be transported far before depletion, ozone causes a regional air pollution problem as well as an urban problem.

Sources and sinks

Table 2.4 lists the estimated global budget of tropospheric ozone, and we see that Reaction (2.12) followed by (2.13) clearly is the largest source. Reaction (2.12) is both a result of the rapid cycling between NO and NO_2, and of CO oxidation by OH as shown in the reaction sequence (2.4)-(2.8). The reaction between NO and an organic peroxy radical RO_2, combined with the CH_3O_2+NO reaction, only constitute 30 % of the chemical production of ozone on the global scale. However, over urban areas this portion could increase considerably due to larger emissions of NMVOCs eventually leading to RO_2 and CH_3 formation. Transport from the stratosphere is another source of tropospheric ozone, but is less significant than chemical production.

One of the main sinks of tropospheric ozone is

$$O_3 + h\nu \rightarrow O_2 + O(^1D) \qquad \lambda < 310 \text{ nm} \tag{2.15}$$

$$O(^1D) + H_2O \rightarrow 2OH \tag{2.16}$$

In remote regions of the troposphere, additional loss of ozone is caused by reactions with HO_2 and with OH. At the Earth's surface, O_3 is lost through dry deposition, but this is a relatively minor sink compared to chemical loss.

In many regions of the troposphere, the ozone mixing ratio is controlled by the so-called photostationary-state relationship which includes the reactions

$$NO + O_3 \rightarrow NO_2 + O_2 \tag{2.17}$$

$$NO_2 + h\nu \rightarrow NO + O \qquad \lambda < 420 \text{ nm} \tag{2.18}$$

$$O + O_2 + M \rightarrow O_3 + M \tag{2.19}$$

The mixing ratios of ozone are higher than of NO or NO_2 in the free troposphere. In urban areas, however, mixing ratios of NO often exceed O_3 mixing ratios and (2.17) may deplete ozone.

A major difference between the free troposphere and urban areas is that (2.17) is not the only reaction that convert NO to NO_2 in urban air. NMVOCs compete with O_3 by the reaction

$$NO + RO_2 \rightarrow NO_2 + RO \tag{2.20}$$

where RO_2 indicates organic peroxy radicals. Hence, the photostationary-state relationship is usually not valid in urban air, and the net effect when NMVOCs are present is formation of ozone. An exception is in the afternoon when concentrations of organic gases in urban air decrease, and the photostationary-state relationship holds better.

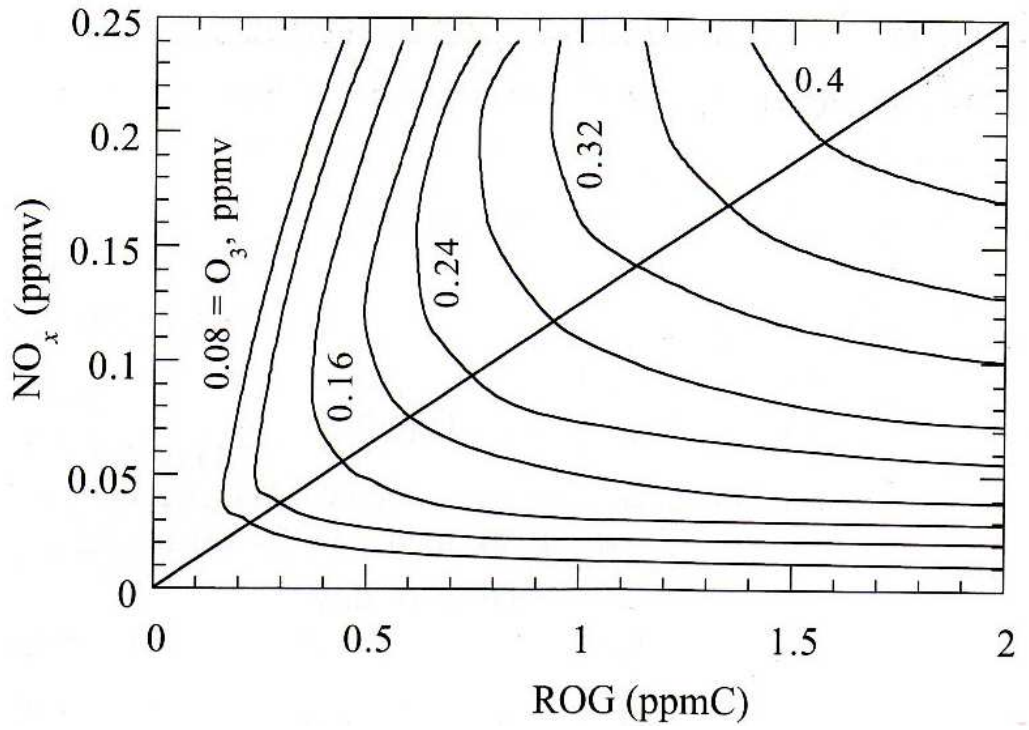

Figure 2.4: *Ozone isopleth showing peak ozone mixing ratios resulting from different initial mixing ratios of NO_x and reactive organic gases (ROGs). ROGs are defined as total organic gases minus methane. (Jacobson, 2005).*

NO_x- and VOC-limited regimes

The ozone isopleth in Figure 2.4 shows the nonlinear relationship between ozone mixing ratios and different mixtures of NO_x and ROGs ($\sim$ NMVOCs). When the initial mixing ratio of NO_x is low, an increase in the abundance of VOCs does not affect the amount of ozone. When NO_x levels are high, an increase in VOC mixing ratios causes increasing ozone values. In the latter case, ozone production is limited by the abundance of VOC, and hence it is called the VOC-limited regime.

At low VOC levels, the isopleth shows that an increase in NO_x could decrease the amount of ozone. The reason is that (2.17) is the main reaction converting NO to NO_2 and when (2.18) ceases at night, the net reaction is ozone loss. When VOC levels are high, an increase in NO_x causes increasing ozone values, and we call this case the NO_x-limited regime. The isopleth only considers chemistry, but in the real atmosphere, meteorology also impacts the level of ozone.

2.3 Meteorological factors

It is well known that meteorological processes impact the chemistry in a number of different ways. E.g. cloud cover has an effect on the photochemistry through the photodissociation rates, and turbulence plays an important role in dispersion of pollutants. In this section, a description of some of the most important meteorological factors in urban scale chemistry is given. Strictly speaking, deposition is more of a chemical process, but is included here because of the strong link between precipitation and wet deposition.

2.3.1 Transport

Advection

Horizontal propagation of the mean wind is called advection. When advection is calculated, the wind is averaged over a certain time, Δt, neglecting rapid fluctuations. The choice of Δt determines the importance of advection versus diffusion. For synoptic-scale motions, the mean wind in the vertical, $\bar{w}$, is typically of the order of a few centimeters per second, which is very slow relative to the fluctuating component, w'. The reason is that turbulence in the atmosphere applies equally to upward and downward motions so that the time averaged value will balance around zero. In the horizontal, however, the situation is turned to the opposite. Mean horizontal winds are $\sim$1000 times faster than vertical winds, and they are more organized.

In Equation (2.1), the transport terms, $\sum F = F_{in} - F_{out}$, may be divided into advection and diffusion, $\sum F = F_A + F_D$. The time rate of change in concentration by advection may be given for a tracer as

$$F_{A,x} = -n_a u \frac{\partial \mu}{\partial x}, \quad F_{A,y} = -n_a v \frac{\partial \mu}{\partial y}, \quad F_{A,z} = -n_a w \frac{\partial \mu}{\partial z} \tag{2.21}$$

where $F_{A,x}$, $F_{A,y}$ and $F_{A,z}$ express concentration changes due to wind in x-, y-, and z-directions, respectively. u, v, and w are wind components, n_a is the number density of air, and μ is the mixing ratio of the tracer. As seen from (2.21), there must be a spatial change in the mixing ratio of the tracer if the advection is to contribute to the time rate of change of the tracer concentration. When a tracer is transported by advection, its concentration increases on the leeward side of the mixing ratio maximum, and decreases on the windward side.

Diffusion

Diffusion in the troposphere is largely dominated by turbulence. Molecular diffusion is slow and can generally be neglected except in a shallow layer near the surface. In opposition to laminar flow which is smooth and steady, turbulence is recognized as random fluctuating motions. As indicated in Figure

2.1a, turbulent flow has a time scale ranging from seconds to a few minutes, and a length scale ranging from a few meters to a few hundred meters. In most models, turbulence is a subgrid scale process that has to be parameterized and represented as statistical effects on the mean flow.

There are two types of turbulence; mechanical and thermal. When horizontal winds are slowed due to friction at the ground, a vertical wind shear is developed near the surface. Eddies mix heat and chemical species both horizontally and vertically, and this is called mechanical turbulence. Thermal turbulence arise when the surface is heated by the sun and the lowest part of the atmosphere becomes unstable.

As for advection, transport by diffusion may be divided into the three spatial directions and be expressed as

$$F_{D,x} = -n_a K_x \frac{\partial^2 \mu}{\partial x^2}, \quad F_{D,y} = -n_a K_y \frac{\partial^2 \mu}{\partial y^2}, \quad F_{D,z} = -n_a K_z \frac{\partial^2 \mu}{\partial z^2} \tag{2.22}$$

where K_x, K_y, and K_z are diffusion coefficients. The second derivative of the tracer mixing ratio along each direction determines how fast the concentration changes due to diffusion. Generally, diffusion results in dispersion from high towards low mixing ratios. The set of equations in (2.22) shows that diffusion is independent of advective wind direction. Hence, tracers are transported in all directions leading to a dampening in the spatial variations.

Convection

The troposphere is usually heated from below and cooled from above due to efficient absorption of incoming radiation at the ground, and because there is net radiative cooling in the middle and upper troposphere. In addition, latent heat is released during condensation of water vapor, and this effect also contributes to destabilization of the troposphere. When the potential virtual temperature decreases with height in unsaturated air, the atmosphere is statically unstable. The motion of an air parcel will then grow exponentially with time and cause convection, which is a process where the troposphere stabilizes itself. On a global scale, the atmosphere is statically stable, but there are regions of unstable air masses.

In the context of this study, convection is of great importance due to rapid mixing of air masses, and because convection usually occurs on small spatial scales. Deep convective clouds are essential since they often transport air masses, and consequently trace gases, from the boundary layer to the free atmosphere. Common spatial scales for convection are a few square kilometers in small cumulus clouds typical on a summer day, to several thousands of square kilometers. In the tropics and in large organized convection systems, convection may extend vertically from the surface to the tropopause. Away from the tropics, mixing is usually on a local scale where the upward

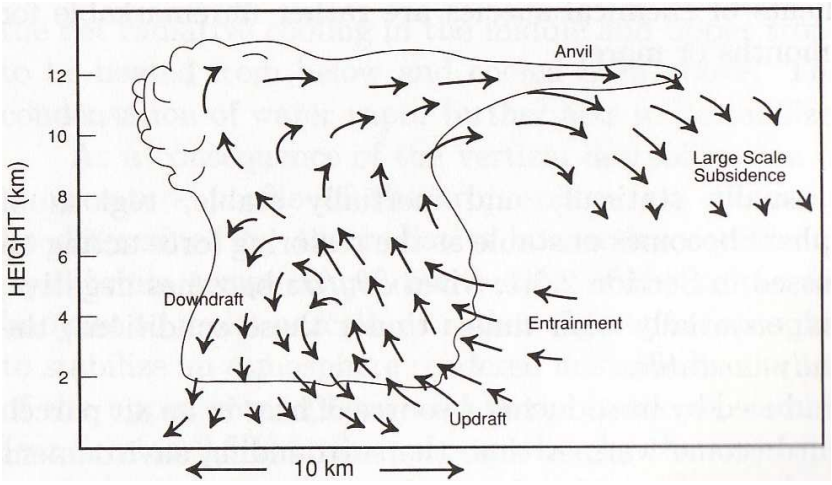

Figure 2.5: *Mass fluxes in a convective cloud (Brasseur et al., 1999).*

convective motion is balanced locally by downward motions.

The mass fluxes involved in a convective cloud are illustrated in Figure 2.5. In addition to the rapid upward motion during convection, a slower downward motion, or subsidence, takes place on larger spatial scales outside the cloud. As shown in the figure, there are also downdrafts inside the convective cloud due to large downward buoyancy forces created by the evaporative cooling of falling rain. Chemical species are rapidly transported downward due to these downdrafts.

There are two ways that convection can arise, either by mechanical means or by buoyancy. In the first case, the vertical motion produced is called forced convection, which occurs when vertical motions in the boundary layer are dominated by mechanical turbulence, when air rises due to topography or a weather front, or when horizontal winds converge and rise. Figure 2.6 shows the complex transport processes in and around a convective cloud associated with a front system. When the production of vertical motion is caused by buoyancy, it is called free convection. This form of convection occurs most often over land during fair weather and light winds. Under these conditions the sun heats the ground differently causing thermal turbulence. The result is the production of thermals which are parcels of air that rise buoyantly.

2.3.2 Planetary Boundary Layer (PBL)

The boundary layer depth varies in both time and space, and is typically between 100-3000 meters deep. In the context of urban air pollution, the boundary layer is important for two reasons. First, when pollutants are emitted within the boundary layer they usually mix rapidly. The rate of

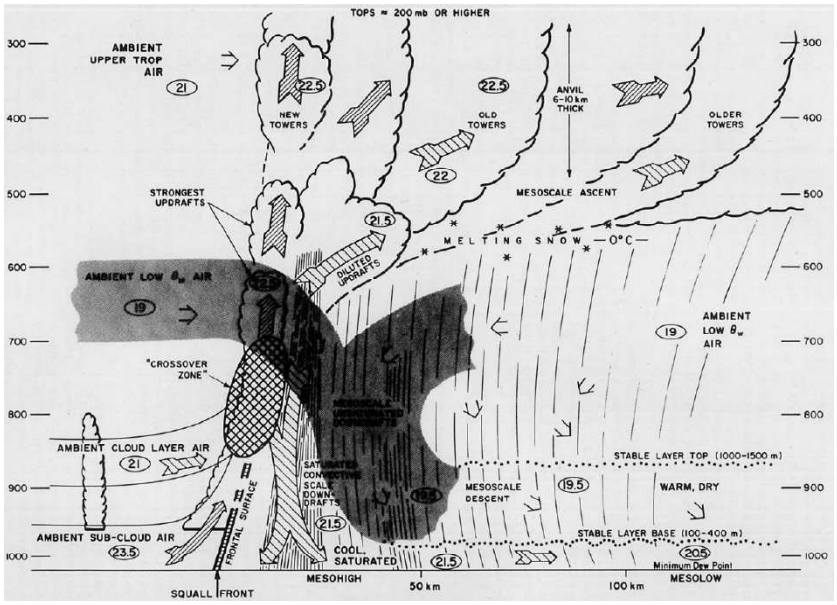

Figure 2.6: *Schematic cross section through a class of squall systems. All flow is relative to the squall line from right to left. (Zipser, 1977)*

mixing depends on weather conditions and topography, and in an unstable turbulent boundary layer it may only take a few hours before a pollutant has been distributed uniformly. Second, there is a strong inversion on top of the boundary layer, making it almost impermeable. It could take several days before a gas emitted from a surface source is transported into the free troposphere. For these two reasons, it is critical to know whether emissions take place below or above the top of the boundary layer.

Calculations in Jacob (1999) show that vertical mixing of air in the PBL takes 1-2 days, while ventilation of the PBL with air from the middle troposphere takes about one week on average. Mixing of the whole troposphere takes about one month on average, resulting in large vertical differences of short-lived species. Figure 2.7 shows an example of the large diurnal variation in the PBL height. At night, the PBL is relatively shallow due to a weak heat transport towards the surface. When the sun heats the ground during the day, strong heat transport from the surface leads to unstable conditions and increasing PBL height. After sunset, the heat flux will again be directed towards the ground and the mixing layer height decreases rapidly. In addition to the diurnal variations, there are also geographical and seasonal differences in the height of the boundary layer.

Boundary layer processes are rapid and take place on small scales. Together with the surface parametrization, the PBL parameterization determines the surface fluxes, which influence the budgets of momentum, heat, and moisture. The boundary layer processes also interact with other small-scale processes,

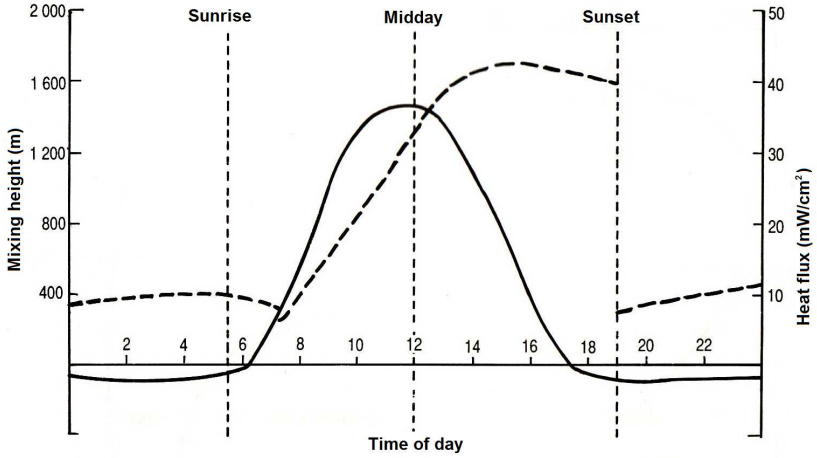

Figure 2.7: *Diurnal variation in PBL height (dashed line) and vertical heat flux at the ground (solid line, upward is positive) for a summer day over England (modified from Stordal and Hov (1993)).*

e.g. clouds and convection. When long time periods are simulated with a large-scale model, the effects of subgrid scale flow on the mean flow become particularly important, and it is therefore essential to have the most realistic representation of these subgrid processes.

2.3.3 Sunlight and cloud cover

The cloud cover clearly impacts the photochemistry through photolysis rate coefficients, but it also has an effect on the PBL height. When a cloud layer is present, it has a greenhouse effect during night, resulting in a relatively large PBL height. During the day, the cloud layer reflects some of the incoming sunlight and the PBL height is lower than in clear sky conditions.

Photolysis reactions, e.g. the tropospheric loss of O_3 to $O(^1D)$ and Reaction (2.18), are all initiated by sunlight. A cloud layer will impact the amount of sunlight that reach different parts of the troposphere. When clouds scatter incoming sunlight, the actinic flux will be changed. This results in an increased flux above the clouds, a decreased flux below, and complex changes within the clouds. In turn, photodissociation rates of oxidant species will be altered and hence the concentrations of chemical species will change (Tie et al., 2003).

2.3.4 Water Vapor

We pointed out in Section 2.2.1 the importance of OH as a scavenger in the atmosphere. Oxidation of water vapor (Reaction (2.3)) is the major source of OH in the troposphere, and thus it affects the ozone budget. Another characteristic of water vapor is its influence on the atmospheric stability due

to transport and release of latent heat. In the troposphere, the distribution of water vapor varies considerably with meteorological conditions, but also with geographical location and height.

The definite major source of water vapor in the air is evapotranspiration, which is the sum of evaporation and transpiration. Evaporation from the ocean surface constitutes approximately 85 % of the water in the atmosphere, and in addition there is evaporation from lakes, rivers, and soils. Sublimation from glaciers, sea ice, and snow also contribute to water vapor in the air, as well as transpiration from plant leaves. Other sources of water vapor include chemical reactions and fuel combustion. Sinks of water vapor are condensation, ice deposition, and chemical reactions.

Higher temperatures increase the amount of water vapor that air can hold before condensation occurs. This fact clearly impacts the geographical distribution of water vapor at the Earth's surface. Near the poles, where temperatures are low, water vapor condenses to liquid and consequently mixing ratios are close to zero. In the tropics, however, mixing ratios may reach 4 % or more due to the high temperatures causing evaporation. During the passage of a frontal system, relative humidities are often high because of convection. When air becomes saturated, clouds form and may cause precipitation. Both the increased humidity and the increased cloud cover near a weather front will affect the ozone chemistry.

2.3.5 Deposition

As shown in Figure 2.2, atmospheric species are subject to wet and dry deposition. These removal processes become extremely important in regional air quality, but are also important on an urban scale. Wet deposition often occur on small scales due to the convective activity that is usually associated with precipitation scavenging. Dry deposition depends largely on the type of surface and is thus expected to differ when grid resolutions are changed.

Wet deposition occurs only when there is precipitation. Trace gases and particulates are removed from the atmosphere when they get absorbed into water droplets, ice particles and snow flakes, and then deposited onto the Earth's surface during precipitation. It is the physical and chemical properties of the precipitation element and of the trace gas that determine the amount of absorption. The balance between the gas phase and the liquid phase of the species concentration is given by Henry's law:

$$c_a = k_H \cdot p_g \tag{2.23}$$

where c_a is the concentration in liquid phase, which is proportional to the partial pressure p_g, which is again proportional to the concentration of the species in the gas phase, c. The Henry's law constant k_H, determines the

Gas		k_H [M atm^{-1}]
HNO_3	Nitric acid	2.1×10^5
CH_2O	Formaldehyde	3.2×10^3
OH	Hydroxyl radical	3.0×10^1
CH_3CHO	Acetaldehyde	1.4×10^1
NO_3	Nitrogen trioxide	1.8×10^0
NO_2	Nitrgoen dioxide	1.2×10^{-2}
O_3	Ozone	9.4×10^{-3}
NO	Nitrogen monoxide	1.9×10^{-3}
C_2H_6	Ethane	1.9×10^{-3}
O_2	Oxygen	1.3×10^{-3}
CO	Carbon monoxide	9.9×10^{-4}
N_2	Nitrogen	6.1×10^{-4}

Table 2.5: *Solubility of gases at 298 K given by Henry's constant k_H (Sanders, 1999).*

solubility of the species, where a higher value means higher solubility. Table 2.5 gives k_H values for some of the gases in the atmosphere. Of the species listed in the table, HNO_3 has clearly the largest solubility. Formaldehyde is also quite soluble, while e.g. O_3, NO and CO do not easily get absorbed by cloud droplets.

Some components are deposited to the Earth's surface even when precipitation is not present. This is known as dry deposition. The time rate of change in concentration due to dry deposition may be given as

$$\frac{dc}{dt} = -\frac{v_d}{h}c \tag{2.24}$$

where c is the average concentration of the gas in the boundary layer, h is the PBL height, and v_d is the deposition velocity. The transfer of a gas from the atmosphere to the surface can be divided into two forms; transport from the atmosphere to the surface, and uptake at the surface. The deposition velocity is usually expressed as the inverse of a resistance r:

$$\frac{1}{v_d} = r = r_g + r_s \tag{2.25}$$

where r_g is the resistance in the process that transports the gas to the ground, and r_s is the resistance in uptake by the soil, vegetation or water surface. The first resistance depends on meteorological factors while the latter depends on the characterizations of both the gas and the surface. Dry deposition is an important sink for e.g. CO, NO_x, and O_3.

Chapter 3

Model and methodology

3.1 The WRF model

The model applied in this study (WRF-Chem) is based on the Weather Research and Forecasting model, WRF. The WRF model is a numerical weather prediction system that can be used for both operational forecasting and atmospheric research on mesoscale, regional scale, and local scale. Several agencies have collaborated on developing the WRF model, principally the National Center for Atmospheric Research (NCAR), the National Oceanic and Atmospheric Administration (NOAA), the National Centers for Environmental Prediction (NCEP), the Forecast Systems Laboratory (FSL), the Air Force Weather Agency (AFWA), the Naval Research Laboratory (NRL), Oklahoma University, and the Federal Aviation Administration (FAA). It is an Eulerian non-hydrostatic and fully compressible model. The principal components of the WRF system are WRF Pre-Processing System (WPS), two dynamic solvers (ARW and NMM), and WRF variation data assimilation (WRF-Var). A more detailed outline of the various components is shown in Figure 3.1.

3.1.1 Dynamics in WRF

The Advanced Research WRF (ARW) is the default dynamics solver and is developed primarily at the National Center for Atmospheric Research (NCAR). The solver uses a time-split third-order Runge-Kutta scheme for integration of the governing equations in the atmosphere, and some of the variables it calculates include winds (u, v, and w), perturbation potential temperature, perturbation geopotential, and perturbation surface pressure of dry air.

The vertical coordinate used in the ARW solver is η, which is similar to the σ coordinate used in many hydrostatic atmospheric models. This terrain-following hydrostatic-pressure vertical coordinate varies from a value of 1 at

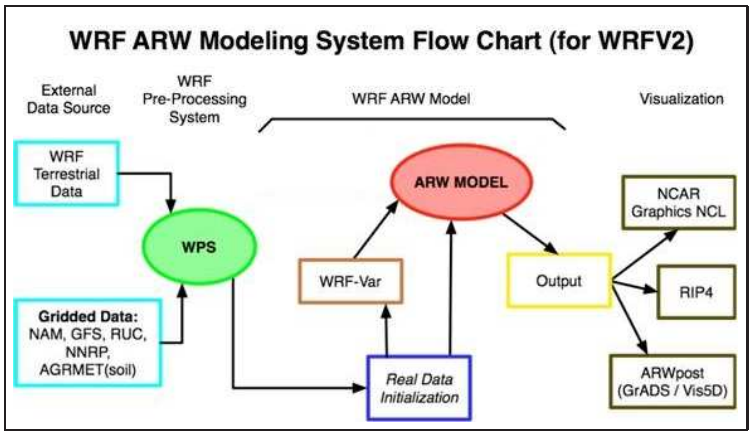

Figure 3.1: *The data flow between the different components in the WRF system (modified from Wang et al. (2007)).*

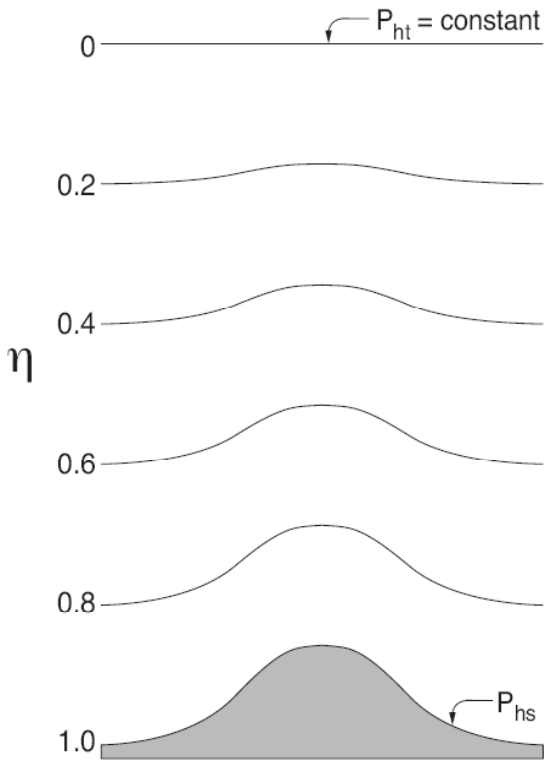

Figure 3.2: *The vertical η coordinate used in the ARW (Skamarock et al., 2007).*

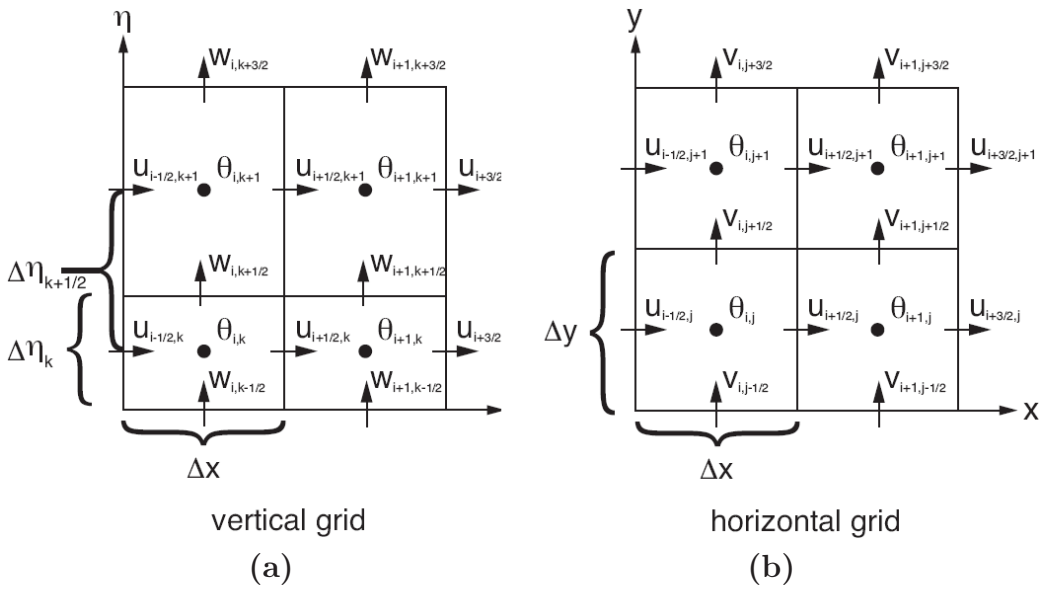

Figure 3.3: *Arakawa C is used for (a) vertical and (b) horizontal grids (Skamarock et al., 2007).*

the surface to 0 at the upper boundary of the domain (Figure 3.2). The coordinate is defined as

$$\eta = \frac{p_h - p_{ht}}{\mu} \quad \text{where} \quad \mu = p_{hs} - p_{ht}. \tag{3.1}$$

p_h is the hydrostatic component of the pressure, p_{hs} refers to the value along the surface, and p_{ht} is the value on the top boundary. Optionally, the user can specify the number of vertical levels and the η-value of each level, as long as the η-values decrease monotonically from the surface to the constant pressure top level. The vertical velocity and the geopotential is calculated for all these levels of equal η value, which is referred to as full levels in a staggered grid (Figure 3.3a). The half levels, or mass levels, are in an unstaggered grid, and this is where the thermodynamic variables are calculated.

As for the vertical grid, Arakawa C is also used for the horizontal grid (Figure 3.3b). For easier calculation of advection between the grid boxes, the normal velocities in this grid are staggered one-half grid length from the thermodynamic variables. The grid lengths Δx and Δy are constants in the model, but the Earth's spherical shape has to be accounted for. This problem is solved by introducing a map scale factor defined as

$$m = \frac{(\Delta x, \Delta y)}{\text{distance on the earth}}. \tag{3.2}$$

The mass per unit area within the column at (x, y) in the model is represented by $\mu(x, y)$. The flux form variables can then be defined as

$$\mathbf{V} = \mu\mathbf{v} = (U, V, W), \quad \Omega = \mu\dot{\eta}, \quad \Theta = \mu\theta, \tag{3.3}$$

where $\mathbf{v}$ is the three-dimensional velocity vector, $\omega = \dot{\eta}$ expresses the vertical velocity, and θ is the potential temperature. The six prognostic Euler equations on flux-form can be written as

$$\partial_t U + (\nabla \cdot \mathbf{V}u) - \partial_x(p\phi_\eta) + \partial_\eta(p\phi_x) = F_U \tag{3.4}$$

$$\partial_t V + (\nabla \cdot \mathbf{V}v) - \partial_y(p\phi_\eta) + \partial_\eta(p\phi_y) = F_V \tag{3.5}$$

$$\partial_t W + (\nabla \cdot \mathbf{V}w) - g(\partial_\eta p - \mu) = F_W \tag{3.6}$$

$$\partial_t \Theta + (\nabla \cdot \mathbf{V}\theta) = F_\Theta \tag{3.7}$$

$$\partial_t \mu + (\nabla \cdot \mathbf{V}) = 0 \tag{3.8}$$

$$\partial_t \phi + \mu^{-1}[(\mathbf{V} \cdot \nabla\phi) - gW] = 0 \tag{3.9}$$

where $\phi = gz$ is the geopotential and p is the pressure. The diagnostic relation for the inverse density, $\alpha = 1/\rho$, can be written

$$\partial_\eta \phi = -\alpha\mu, \tag{3.10}$$

and the equation of state is

$$p = p_0 \left(\frac{R_d\theta}{p_0\alpha}\right)^\gamma. \tag{3.11}$$

Here, $\gamma = c_p/c_v = 1.4$ is the ratio of the heat capacities for dry air, R_d is the gas constant for dry air, and p_0 is a referance pressure. The terms on the right-hand-side, F_U, F_V, F_W, and F_Θ are the forcing terms. In the system of equations above, the subscripts x, y, and η denote differentiation,

$$\nabla \cdot \mathbf{V}a = \partial_x(Ua) + \partial_y(Va) + \partial_\eta(\Omega a), \tag{3.12}$$

and

$$\mathbf{V} \cdot \nabla a = U\partial_x a + V\partial_y a + \Omega\partial_\eta a, \tag{3.13}$$

for a generic variable a.

As mentioned earlier, a time-split Runge-Kutta scheme is applied to solve the flux-form Euler equations. This means that two time steps will be used; one for the meteorologically significant low-frequency modes, and one smaller time step for the meteorologically insignificant acoustic high-frequency modes. If the same time step is used for both modes, numerical instability would occur. An RK3 time step (in seconds) of approximately 6 times the grid distance (in kilometers) would be a safe choice to avoid instability.

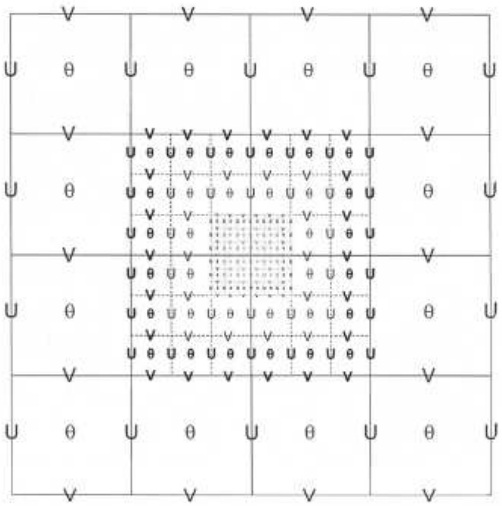

Figure 3.4: *Example of the Arakawa C grid when three nested grids are telescoped to increase the resolution (Skamarock et al., 2007).*

3.1.2 Nesting

Nesting is the implementation of an additional grid with finer spatial and temporal resolution into a parent grid with coarser resolution. Horizontal nesting is supported in the ARW, but no vertical nesting option is included in the current version. An advantage of the nesting technique in the ARW is the efficiency when doing nested simulations on parallel computer systems, and the support for moving nested grids.

There are two ways that information can be exchanged between the grids: either 1-way or 2-way nesting. In a 2-way nest simulation, the coarse grid is integrated first to produce boundary conditions for the fine grid. Then the fine grid integration takes place and the solution replaces the coarse grid values for those points that are inside the fine grid. If 1-way nesting is used, the procedure is the same as for 2-way nesting except there is no feedback from the fine to the coarse grid.

There are two possible nest configurations in the ARW. With the so-called telescoping nests, which we use in this study, the resolution is increased by implementing several grids in a telescope shape. Figure 3.4 shows an example of telescoping nests with a grid ratio of three between the parent and the child nests. The grids may be telescoped to a resolution of a few hundred meters, but usually there will be computational restraints before this limit is reached.

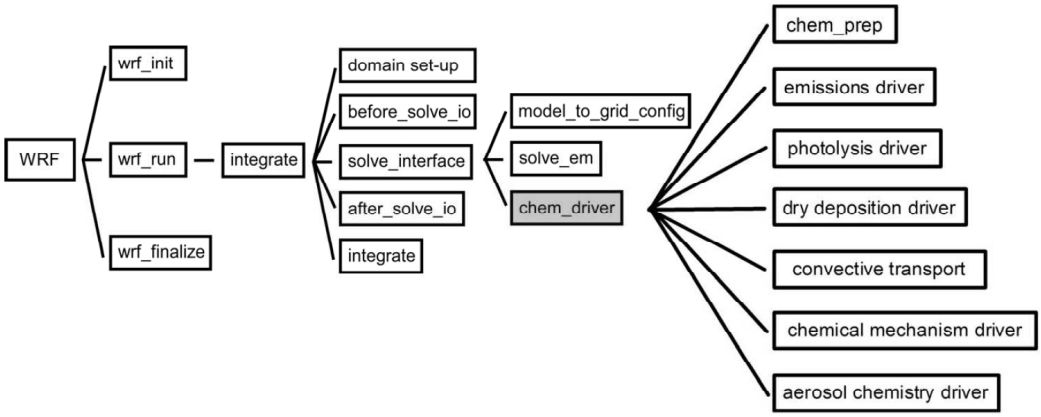

Figure 3.5: *The data flow in WRF-Chem, and the different chemistry routines (modified from Peckham et al. (2006)).*

3.2 WRF-Chem

In the WRF-Chem model, chemistry is fully coupled with the dynamical calculations in WRF. It is an "online" model where the transport scheme, the horizontal and vertical grid, and the physics schemes for subgrid-scale transport are the same for both the meteorological and the chemical components. A detailed description and a statistical evaluation of the model is given in Grell et al. (2005).

The principal contributors to developing WRF-Chem are NOAA, NCAR, the University Corporation for Atmospheric Research (UCAR), the Cooperative Institute for Research in Environmental Sciences, the Max Plank Institute, and the University of Chile. The first version of WRF-Chem was released in 2002, while the latest version became available for download in March 2008[1]. For this study we use version 2.2 which was released in March 2007. The model source code is mainly Fortran 77 and Fortran 90, but some C coding has also been used. Because of the coupling between meteorology and chemistry, WRF-Chem may be used to simulate the release and transport of chemical compounds as well as prediction of O_3, UV radiation, and particulate matter (PM).

Figure 3.5 shows the flow of the WRF-Chem code with focus on the chemistry driver and its routines. The chemistry scheme and the photolysis scheme that we use are discussed in Section 3.3.3. Dry deposition in WRF-Chem is calculated by multiplying the concentrations in the lowest model layer by the spatially and temporally varying deposition velocity, v_d, to give the flux of trace gases and aerosols to the surface. v_d is proportional to the sum of the aerodynamic, sublayer, and surface resistance. The parameterization of

[1]Version 3.0 is available at http://www.mmm.ucar.edu/wrf/users/downloads.html

	Horizontal res.	Horizontal dim.	Vertical layers	Δt
Domain 1	81 km × 81 km	39 × 39	27	405 s
Domain 2	27 km × 27 km	39 × 39	27	135 s
Domain 3	9 km × 9 km	39 × 39	27	45 s
Domain 4	3 km × 3 km	51 × 51	27	15 s
Domain 5	1 km × 1 km	99 × 99	27	5 s

Table 3.1: *Overview of the resolutions, dimensions, and time steps for each of the five domains.*

the surface resistance is developed by Wesley (1989), and depends on the resistances of soil and plant surfaces, the diffusion coefficient, the reactivity, and water solubility of the reactive trace gas.

According to Grell et al. (2005), the prognostic equations integrated for a conserved variable consist of a mass conservation equation and a scalar conservation equation of the form

$$\mu_t + \nabla \cdot (\mathbf{V}\mu) = 0 \tag{3.14}$$

$$(\mu\phi)_t + \nabla \cdot (\mathbf{V}\mu\phi) = 0 \tag{3.15}$$

where μ is the column mass of dry air, $\mathbf{V}$ is the velocity (u, v, ∇), and ϕ is a scalar mixing ratio. The model conserves mass and scalar mass because the equations are discretized in a finite volume formulation. Also, the discrete model transport is consistent and preserves tracer correlations. A description of the time integration scheme and the advection scheme is given in Wicker and Skamarock (2002).

3.3 Model setup

In this study we have carried out WRF simulations for a summer situation with potentially high levels of ozone. The model simulations start on the 22nd of July 2003 and ends on the 12th of August 2003, whereof the first 24 hours are considered spin-up time and are not part of the analysis.

We have chosen to focus on a megacity, London, because of the high emissions and active ozone chemistry that are usually associated with large urban areas. Even though London has decreasing levels of air pollutants, the availability of a detailed emission data set makes it ideal for the purpose of our study. Additionally, observations of air pollutants are available for several stations in London, and this makes it possible for us to validate the model results.

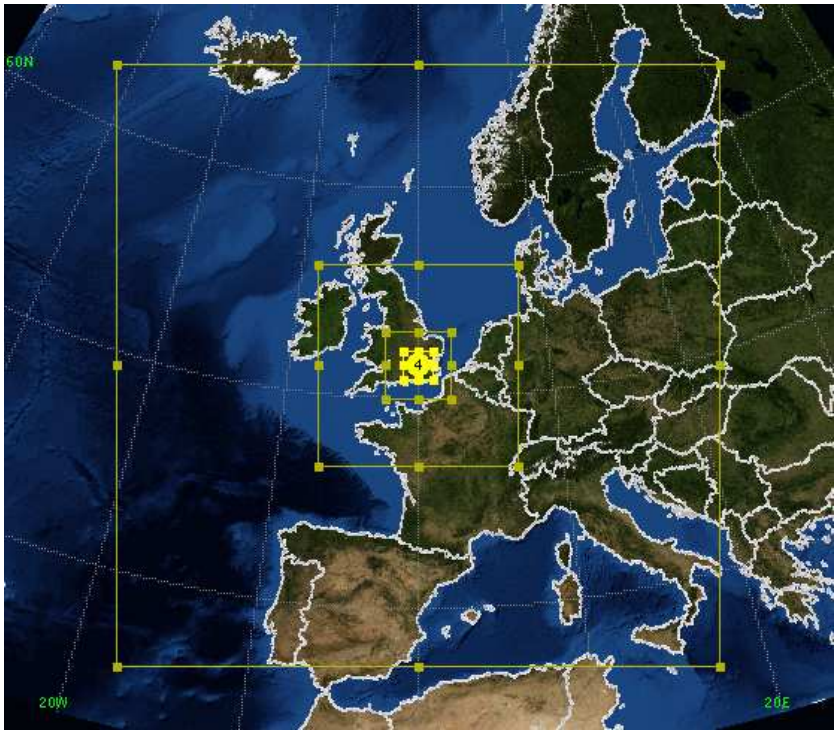

Figure 3.6: *Four of the five nested domains that are used in all simulations. All domains are centered over London at approximately (51.5° N, -0.128° W). (Figure from WRF Domain Wizard).*

3.3.1 Domain setup

Figure 3.6 shows four of the five nested domains used in the WRF simulations. The largest domain covers most of Europe and has a square horizontal grid resolution of 81 km (Table 3.1). Then we zoom in on the United Kingdom and the London Metropolitan area in four successive nesting levels, namely 27 km, 9 km, 3 km, and 1 km. The horizontal dimensions of each domain is shown in Table 3.1. In the vertical there are 27 layers stretching from the ground and up to 50 hPa, which is normally right above the tropopause.

The rather coarse resolution of 81 km in domain 1 is chosen because it corresponds to approximately the size of a CTM grid box when a $1^\circ \times 1^\circ$ resolution is used. London is located on a latitude of $\sim 51.5^\circ$, so that a CTM grid box will have an area of

$$A_{CTM} = dx \cdot dy \approx (R_E d\lambda \cos\phi) \cdot (R_E d\phi) \tag{3.16}$$

$$= \left(R_E \cdot 1^\circ \frac{\pi}{180^\circ} \cos 51.5^\circ\right) \cdot \left(R_E \cdot 1^\circ \frac{\pi}{180^\circ}\right) \tag{3.17}$$

$$= 69.2 \text{ km} \cdot 111.2 \text{ km} \tag{3.18}$$

$$= \underline{7694.5 \text{ km}^2} \tag{3.19}$$

if $R_E = 6.37 \cdot 10^3$ km is the Earth's mean radius, $d\lambda$ is the longitudinal distance expressed in radians, $d\phi$ is the latitudinal distance expressed in radians, and ϕ is the latitude. A grid box in domain 1 in the WRF simulation has an area of $A_{WRF} = 81 \text{ km} \cdot 81 \text{ km} = \underline{6561 \text{ km}^2}$, just a little lower than in the CTM. Although many CTM simulations are carried out with coarser resolution, we believe that the $1^\circ \times 1^\circ$ resolution will be used more frequently in the future as the computer capacity increases.

3.3.2 Initialization and boundary conditions

For the meteorology, results from the global ECMWF[2] model serve both as initialization and as lateral boundary conditions in the outer domain. These data have a horizontal resolution of $0.25^\circ \times 0.25^\circ$, and contain analysed fields every 6th hour. The nested domains (2, 3, 4, and 5) are still initialized by ECMWF data, but the boundary conditions are calculated from each domain's parent.

When it comes to chemistry, we use an idealized vertical profile for each chemical species as both initialization and lateral boundary conditions in domain 1. The idealized profile is based on results from a numerical chemistry model, NALROM, and assumes clean environment conditions at mid-latitudes in the northern hemisphere.

3.3.3 Chemistry and photolysis

There are two choices for gas-phase chemical reaction calculations; CBM-Z and RADM2[3] (Stockwell et al., 1990). We use RADM2 which has the advantage of a good balance between detail, accuracy, and computer resources. The reactions included in RADM2 are listed in Appendix B. Among the inorganic species, there are 14 stable species, 4 reactive intermediates, and 3 abundant stable species (oxygen, nitrogen and water) included in this mechanism. Organic chemistry is represented by 26 stable species and 16 peroxy radicals. A reactivity aggregated molecular approach (Middleton and Stockwell, 1990) is used to group together similar organic compounds in a limited number of model groups. To predict chemical production and loss, a quasi steady-state approximation is used (Hesstvedt et al., 1978).

WRF-Chem gives two choices for photolysis scheme; either Madronich (Madronich, 1987) or Fast-J (Wild et al., 2000). Both are coupled with hydrometeors, aerosols, and convective parameterizations. We use Fast-J which is a flexible and accurate scheme, and also computationally efficient. The actinic flux is calculated under both clear and cloudy sky conditions. Photolysis rates may be determined for any species if data describing the absorption cross sections and quantum yields are available.

[2]ECMWF = European Centre for Medium-Range Weather Forecast
[3]RADM2 = Regional Acid Deposition Model, version 2

Acronym	Model simulations	Emission resolution	Domains
AF	All emissions included	Fine	1, 2, 3, 4, 5
NF	No emissions in LMA	Fine	1, 2, 3, 4, 5
AC	All emissions included	Coarse	1, 2, 3, 4, 5
NC	No emissions in LMA	Coarse	1, 2, 3, 4, 5

Table 3.2: *Overview of the different WRF-Chem simulations. London Metropolitan Area (LMA) is defined here as the innermost 81 km x 81 km in the domains. When the emission resolution is set to "fine" it means that the anthropogenic emissions have the same resolution as the domain resolution (domain 1: 81 km, domain 2: 27 km, domain 3: 9 km, domain 4: 3 km, domain 5: 1 km). "Coarse" emission resolution means that the anthropogenic emissions are represented as 81 km x 81 km grid squares in all five domains.*

3.3.4 Simulations

An overview of the different model runs is shown in Table 3.2. All runs are performed using 1-way nesting, so that we are able to quantify the different results due to changes in resolution. Simulation AF is the most realistic, and for that reason the results from this run will be used in the comparison with observations. For simplicity, the London Metropolitan Area (LMA) is defined in this study as the innermost 81 km $\times$ 81 km in the model area. Since the anthropogenic emissions in simulation NF are set to zero inside the LMA, a comparison of AF vs. NF gives the effect of London emissions only. Similarly will AC vs. NC give the impact of London emissions, but with coarse resolution of anthropogenic emissions. This way we can qualitatively say what effects are due to changes in meteorology, and what effects are due to changes in emission resolution.

Input data are prepared with the WRF Pre-processing System (WPS). Figure 3.7 shows the data flow between the three main programs in the WPS system: *geogrid*, *ungrib*, and *metgrid*. The static geographical data needed by *geogrid* are downloaded from http://www.mmm.ucar.edu/wrf/src/wps_files/ and has a resolution of less than 1 km. *Ungrib* extracts fields from the ECMWF data and *metgrid* maps the geographical data and the meteorological data onto the model domains.

3.4 Emissions

3.4.1 Anthropogenic

In this study, high-resolution emissions data are required to see the differences in the results when different grid resolutions are used, and thus produce reasonable results. London is chosen as the study area partly because of the availability of a detailed emissions data set. Anthropogenic emissions in this

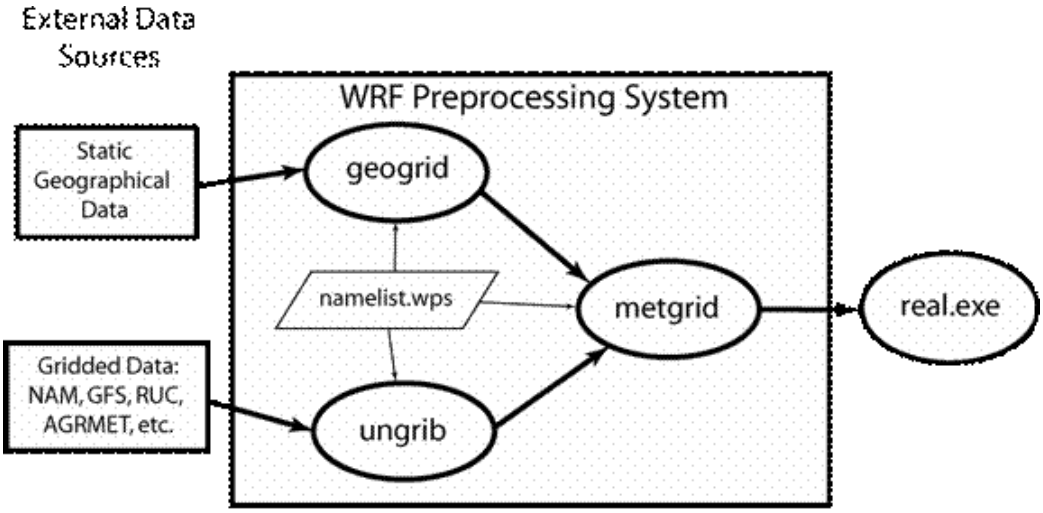

Figure 3.7: *The data flow between the programs in the WPS (Wang et al., 2007).*

study are based on yearly 1 km × 1 km data from the UK National Atmospheric Emissions Inventory (NAEI) (DEFRA, 2007). Outside the United Kingdom, and within the area covered by the largest domain (Figure 3.6), anthropogenic emissions are taken from the 0.5° × 0.5° RETRO inventory (RETRO, 2006).

A Fortran program has been developed to merge the NAEI and RETRO data and to convert the emissions into the lumped RADM2 species needed as input to WRF-Chem. The NAEI data are read as total tonnes from each emission source of the species CO, NO_x and NMVOC for the year 2005. Based on yearly data from Dore et al. (2007), simple factors have been derived to scale the emissions to approximate values for the year 2003. The same report has also been used to calculate source-dependent factors needed to split the NMVOCs into 50 different species.

The RETRO data are taken as July 2000 values, and has not been scaled to 2003 values. However, the RETRO data only serve as boundary conditions to the focus area of this study (the innermost 81 km × 81 km), so we believe the differences from 2003 values do not influence the results significantly.

Both the NAEI and the RETRO data are then converted to the unit of moles km^{-2} hr^{-1} before they are lumped into RADM2 species (Appendix A). An interpolation routine is implemented in the Fortran program to regrid the emissions data to the correct resolution and to the Lambertal coordinate system. To obtain a diurnal variation in the emissions, the values are multiplied by a factor depending on the time of day and the emission source. The emission data are then written to binary files used as input to the WRF

CO	NO_x	VOC
2946.53	1728.45	1063.58

Table 3.3: *UK emission inventory of CO, NO_x, and VOC in ktonnes for the year 2003.*

model simulations.

Table 3.3 shows the total UK anthropogenic emissions of CO, NO_x, and VOC for the year 2003. The spatial distribution of the combined NAEI and RETRO emissions used in WRF-Chem is shown in Figure 3.8 for NO_x at 12UTC. It is evident from Figure 3.8a that the large emission sources in northern England, the Benelux countries, and western Germany will impact the ozone chemistry in the London area. In Figure 3.8b we see clearly that the regions of large NO_x emissions reflect the location of major roads in the London area, with the orbital road in particular.

3.4.2 Biogenic

We have chosen to use a biogenic emission module, included in WRF-Chem, to calculate the biogenic emissions online in the model. The emissions are estimated based on land usage and meteorological conditions according to Guenther et al. (1993, 1994), Simpson et al. (1995), and Schoenemeyer et al. (1997). Emissions of isoprene, monoterpenes, other biogenic VOC (OVOC), and nitrogen emissions by the soil are treated in the module. The emissions of monoterpenes and OVOC are split into the species classes in the RADM2 scheme. Isoprene emissions by the forest are computed as a function of temperature and photosynthetic active radiation, while isoprene emissions from agricultural and grassland areas, and emissions of monoterpenes, OVOC, and nitrogen are computed as functions of temperature only.

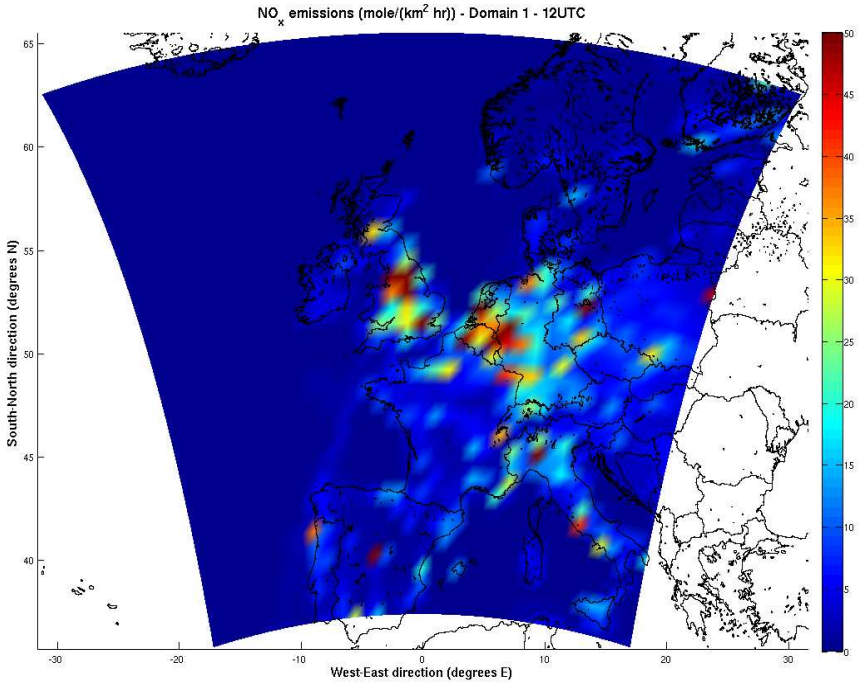

(a)

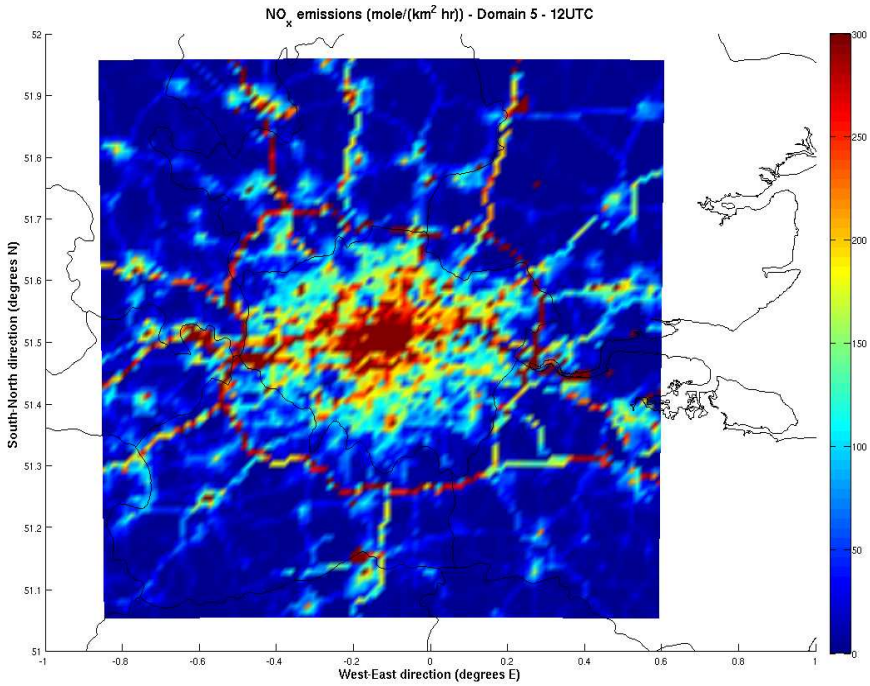

(b)

Figure 3.8: *Estimated emissions of NO_x (moles $km^{-2}hr^{-1}$) used in (a) domain 1, and (b) domain 5 in simulation AF.*

Chapter 4

Results and discussion

Results from the WRF-Chem simulations over London will be presented and discussed in this chapter. The focus will be on changes in ozone chemistry caused by differences in model resolutions, and the reasons for these changes. In addition, preliminary effective emission factors are calculated, and proposals for further research are listed. First, a brief overview of the weather situation during the simulation period is given, and then model results are compared with observations to reveal possible elements of uncertainty.

4.1 Meteorological conditions

Figure 4.1 shows analysis charts at four different times during the simulation period. Generally, the first half of the time period is a typical summer situation with a few episodes of rain and some periods of fair weather in the UK. The second half of the time period is a highly unusual situation with a high pressure area leading to a heat wave in many parts of Europe. Stedman (2004) estimates that the elevated ozone and PM_{10} concentrations associated with the heat wave during the first two weeks of August 2003 lead to an excess of between 423 and 769 deaths in England and Wales.

On July 25 (Figure 4.1a), a low pressure system brings rain over the UK. In the London area, the WRF-simulations gave a total precipitation of 54 mm, whereof 98 % fell during the first 10 days. This means that scavenging by precipitation has most likely occured in the first time period. The UK is still characterized by some unstable air masses on July 31 (Figure 4.1b), but a high pressure area is gradually building up over Europe.

At midday on August 5 (Figure 4.1c) there is a strong high pressure area over most of western Europe. Since the air is moving in a clockwise direction around the high, hot and dry continental air masses are brought to the UK at this time. This kind of weather conditions, characterized by hot, stagnant air and little clouds, are ideal for near-surface accumulation of air pollutants and ozone production. Towards the end of the simulation period, on August 10 (Figure 4.1d), the high pressure area is somewhat weakened, but the SYNOPs still show extremely high temperatures many places in Europe.

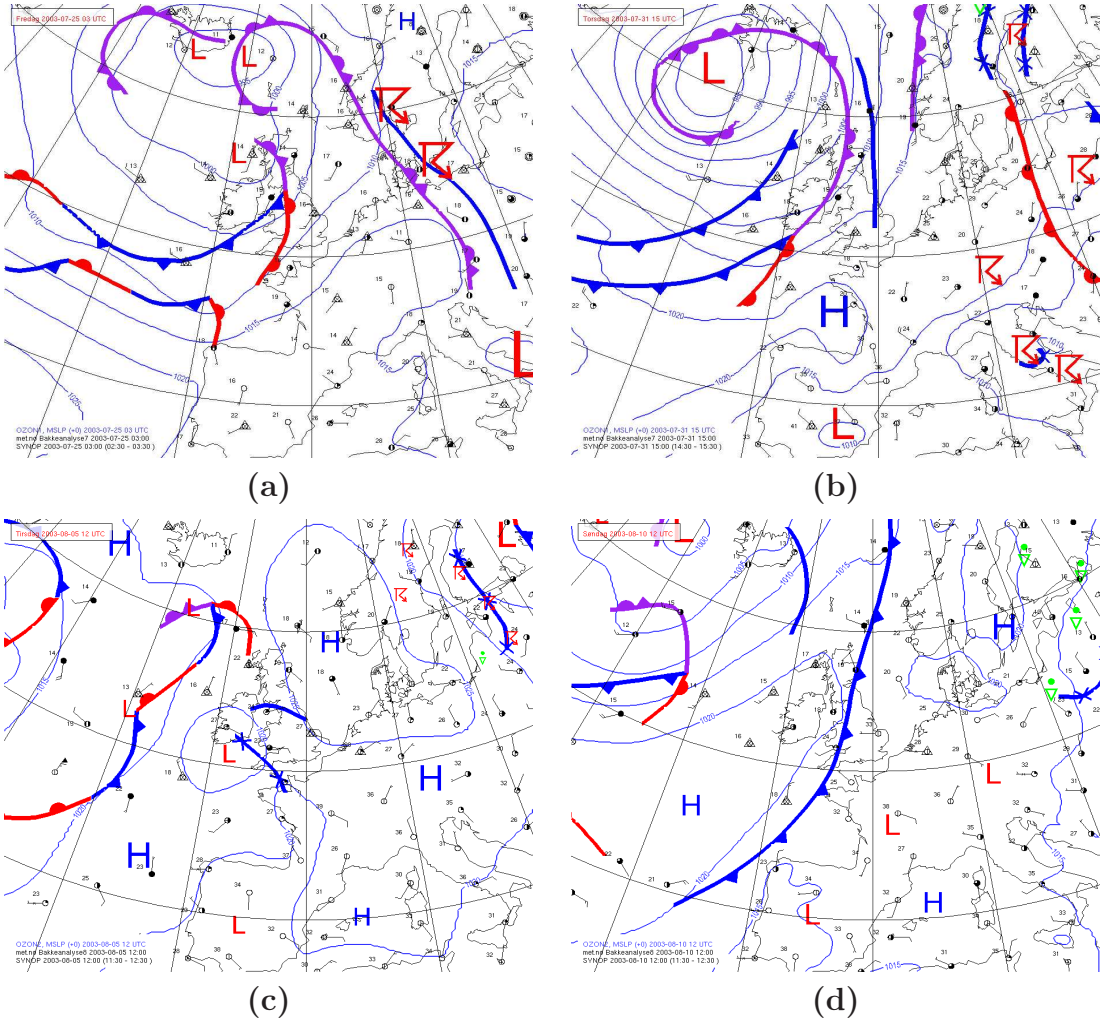

Figure 4.1: *Analysis charts over Europe at times (a) 03UTC 25th of July 2003, (b) 15UTC 31st of July 2003, (c) 12UTC 5th of August 2003, and (d) 12UTC 10th of August 2003. (Source: B. Røsting, The Norwegian Meteorological Institute.)*

4.2 Comparison with observations

An evaluation of the WRF-Chem model is not the aim of this study. Still, we believe that a simple validation of the model results is useful in determining how realistic our results are. For that reason we present comparisons with some observations from London, and a discussion of the model performance. Figure 4.2 shows the location of the observation sites. All the model results used in the comparisons are taken from the finest grid (domain 5) and the most realistic simulation (AF).

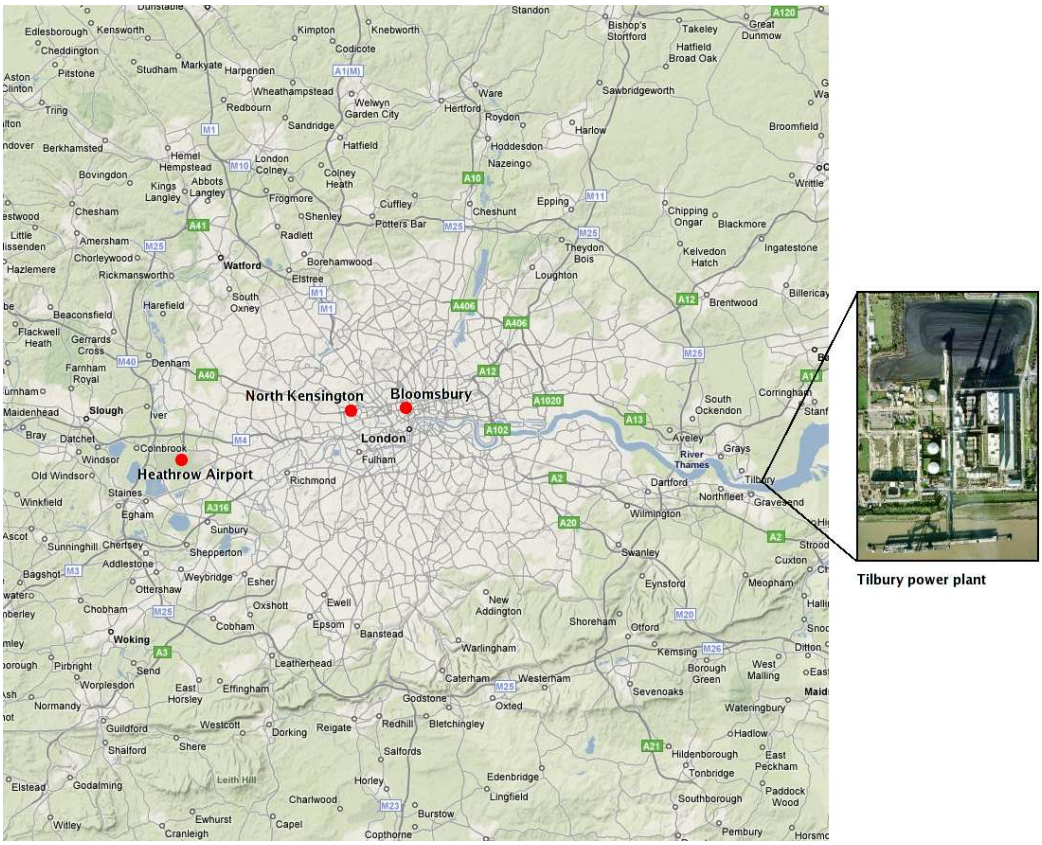

Figure 4.2: *Map of the London Metropolitan Area (LMA), as defined in this study, and the location of the observation sites North Kensington, Bloomsbury, and Heathrow Airport. The location of Tilbury power plant is also shown on the map. (Source: http://maps.google.com.)*

4.2.1 Meteorological variables

In Figure 4.3 we have compared model results and observations of both 2 m temperature and sea level pressure. It seems that the model and the observations are in good agreement, except for a small underestimation of the temperature. Towards the end of the simulation period, the model also overestimates the pressure at sea level. This mismatch at the end of the simulation period might indicate that the time period is too long, and should perhaps be split into two runs. The model is only controlled by the boundary conditions during the whole time period, and a fresh initial field halfway (minus spin-up time) may lead to a better representation of the weather conditions.

Table 4.1 shows the calculated mean and standard deviation of 2 m temperature, sea level pressure, and wind speed for both the model results and the observations at Heathrow Airport. To see the differences in weather conditions more easily, the values are calculated for each of the two time periods;

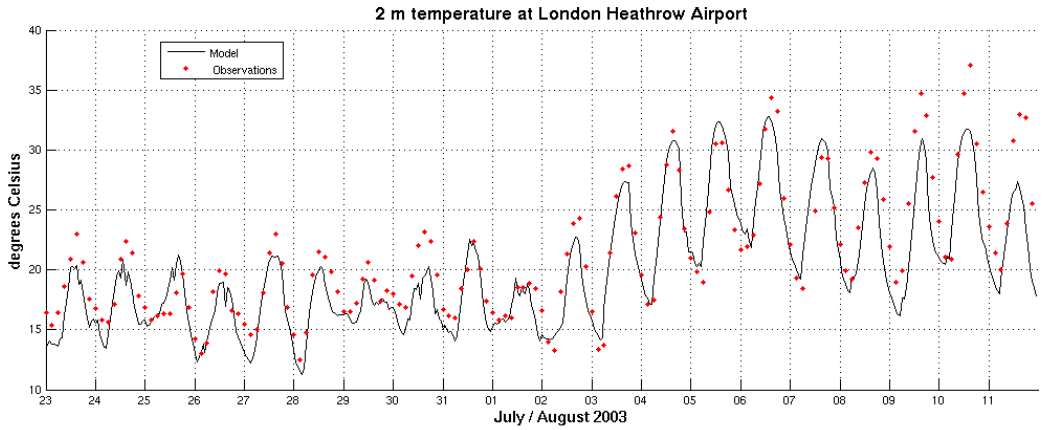

(a)

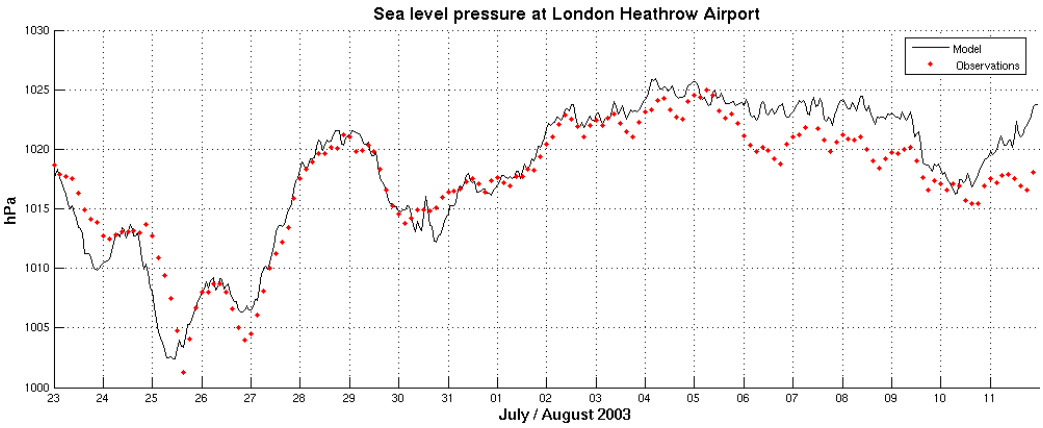

(b)

Figure 4.3: *Model results vs. observations of (a) 2 m temperature and (b) sea level pressure at Heathrow Airport, London.*

	Time period 1				Time period 2			
	Model		Observations		Model		Observations	
	Mean	St.d.	Mean	St.d.	Mean	St.d.	Mean	St.d.
Temp. (°C)	16.8	2.37	18.0	2.46	23.4	4.99	24.6	5.57
SLP (hPa)	1013.8	5.06	1014.2	4.81	1022.5	2.17	1020.4	2.46
W. speed (m/s)	4.35	1.48	4.98	1.85	2.60	1.10	3.29	1.59

Table 4.1: *Calculated mean and standard deviation of model results and observations of 2 m temperature, sea level pressure, and wind speed at Heathrow Airport, London. Time period 1 refers to July 23 - August 1, 2003, and time period 2 refers to August 2 - August 11, 2003.*

July 23 - August 1, 2003 (from now on denoted TP1), and August 2-11, 2003 (from now on denoted TP2). Both the model results and the observations confirm the large differences between the time periods, as indicated by the analysis charts (Figure 4.1). During TP1, the mean temperature and the mean sea level pressure are lower than in TP2. There is also a shift in wind speed with more advection in the first time period than during the second. Evidently, the second time period should lead to more air pollution and active ozone photochemistry than during the first time period.

4.2.2 Chemical variables

Measurements of chemical species have been obtained from DEFRA (2008), and compared with our model results. Figure 4.4 shows time series of CO, NO_x, NO/NO_x, and O_3 at North Kensington in London. This station is categorized as an "urban background" station which means that it is distanced from sources and broadly represents the city-wide background concentrations.

During TP1, the model results agree fairly well with the measurements, but this is not the case in TP2. On some days, the model severely overestimates CO and NO_x mixing ratios in the morning and in the evening. There could be several reasons for this overestimation, but the error is probably caused by the lack of height information in our emissions data set combined with unrealistically low PBL height. A 3-day time series of the PBL height at North Kensington is shown in Figure 4.5. Due to rush hours, the emissions are estimated to peak at 07 or 08 UTC in the morning and at 16 or 17 UTC in the evening. In the morning, the PBL height calculated in the model is fairly low, and consequently the concentrations of CO and NO_x are quite high. The same situation is evident in the evening for NO_x, large emissions and low PBL height give high concentrations.

We have assumed that all emission sources are located in the lowest vertical model layer, which is between the surface and approximately 60 m height. Some point sources, however, have a stack height above 60 m. One such point source is Tilbury power station located by the river Thames just east of the city centre (Figure 4.2). This coal-fired power station is an enormous emitter of NO_x with 16,500 tonnes in year 2005, while CO and VOC emissions were relatively low with 2,280 and 54.8 tonnes, respectively. The stacks at Tilbury reach 170 m, and considering plume rise, this emission source should be placed at 200-300 m height. Obviously, the surface concentrations of NO_x, and to some extent CO, will be overestimated in the model when this large source is assumed to emit below 60 m. Especially at night, when the PBL height is low, large amounts of NO_x will accumulate near the surface in the model.

Due to the large point source east of London, wind direction will play an important role in determining the NO_x-levels at the North Kensington station.

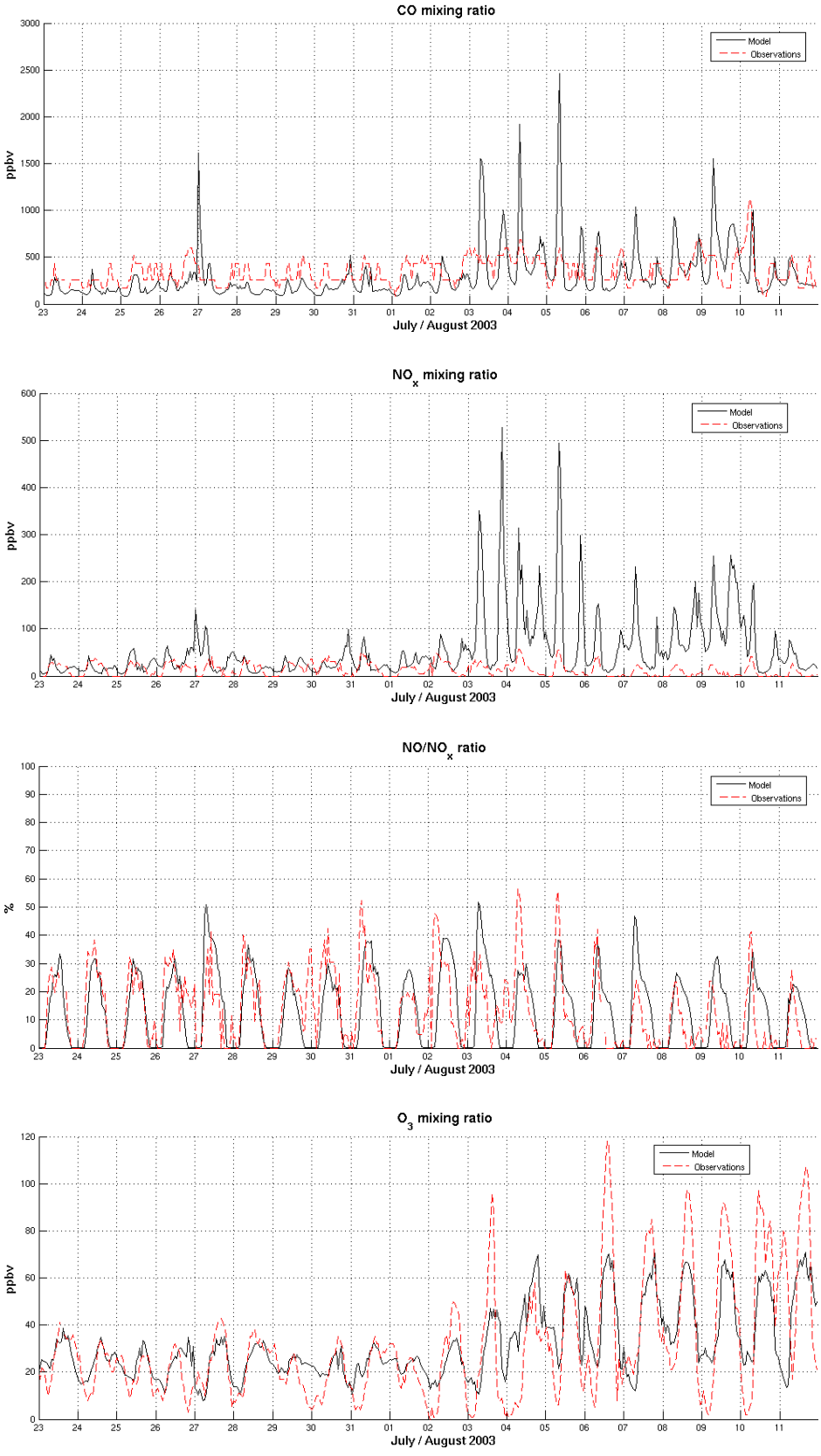

Figure 4.4: *Model results (black solid line) versus observations (red dashed line) of CO mixing ratio (ppbv), NO_x mixing ratio (ppbv), NO/NO_x ratio (%), and O_3 mixing ratio (ppbv) at North Kensington, which is categorized as an "urban background" station.*

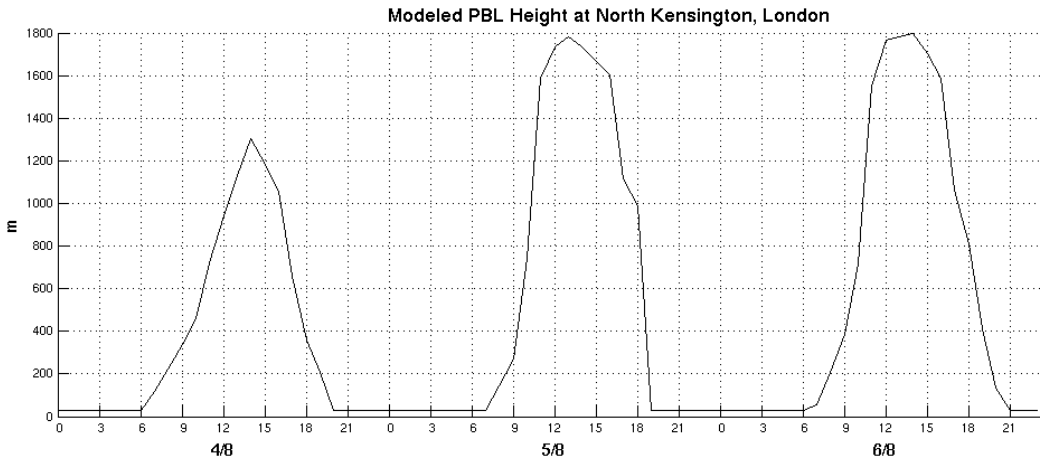

Figure 4.5: *Time series (3 days) of the modeled planetary boundary layer height at North Kensington. Date and UTC hour is shown on the x-axis.*

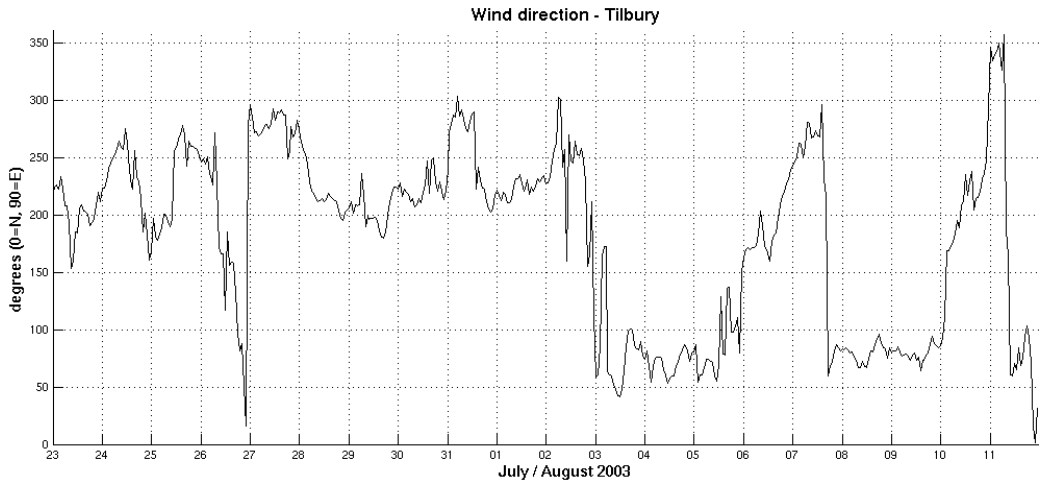

Figure 4.6: *Time series of the modeled 10 m height wind direction at Tilbury.*

Figure 4.6 shows modeled wind direction at Tilbury, and we see a marked shift on the 2nd of August. In TP1, the wind direction is generally from southwest, meaning that emissions from the power station will influence the city centre only slightly. On 6 out of the 10 days in TP2, the wind comes from east. This wind direction causes large amounts of NO_x to be advected from Tilbury towards the city and the N. Kensington station. The NO_x-levels in Figure 4.4 are consistent with the above mentioned wind direction since we have small discrepancies between model and observations in TP1, and very large discrepancies in TP2.

Another factor that could contribute to the deviations between model and observations is the lack of seasonal variation in the UK emissions. August is usually a holiday period associated with less traffic and thus lower emissions of CO and NO_x. This effect is not considered in our emission data set, and could thus explain some of the overestimation of CO and NO_x in the model results. However, we think this factor is minor compared to the lack of vertical height in the emissions.

The ozone levels are fairly well reproduced by the model during the first 10 days. In the second time period, however, the model results show an underestimation of ozone during the day, and an overestimation during the night compared to the measured values. The reason for the underestimation is probably the high levels of NO_x that titrate ozone both during the day and the night. The overestimation at nighttime, however, is more difficult to explain, but may be caused by too much ozone advected into London. Sokhi et al. (2006) did also experience overestimation of ozone during night when comparing model results with measurements in London. They suggested that the discrepancies might be caused by an overprediction of model wind speed when wind speeds were low. According to the authors, the overprediction could be associated with the Monin-Obukhov theory which is used to describe boundary layer stability, and is not strictly applicable for low wind speed conditions (Arya, 1988). Although we have applied a different model and chemistry scheme, the Monin-Obukhov scheme is used in our simulations. The overestimation of ozone was most evident during TP2 when wind conditions were calm. Hence, the reasoning described in Sokhi et al. (2006) could explain some of the discrepancies that we observe in this study.

Accurate predictions of chemical species are dependent on the meteorological parameterizations used. The sensitivity of WRF-Chem predictions to meteorological schemes is investigated in Misenis et al. (2006). They applied the RADM2 chemistry scheme and carried out simulations with different meteorological parameterizations. Compared to observations, modeled O_3 was overestimated at night, and at least part of the reason was a poor representation of the nocturnal PBL by the YSU scheme, which we use in this study. When the MYJ PBL scheme was applied, both daytime and nocturnal PBL height caused better predictions of primary species and O_3. Accordingly,

the overestimation of O_3 at night in this study, may be caused, at least partly, by the poor representation of the PBL height by the YSU scheme. Alternatively, the systematic underestimation may indicate a weakness of the nighttime chemistry in the model.

We have also conducted comparisons of model and observations at other sites in Greater London urban area. All the 8 urban background stations[1] that we compared with model results showed the same trend as in North Kensington. CO and NO_x were overestimated in the morning (and evening for NO_x), and O_3 was underestimated during the day and overestimated at night.

Measurements from an "urban centre" station, Bloomsbury, is shown in Figure 4.7 together with model results. The station is surrounded by a busy road on all four sides, with the nearest road 25 metres away. The overestimation of O_3 at night in the model is even more evident at this station. In the model, the NO/NO_x ratio is zero every night, indicating that all NO-molecules react with O_3 to produce NO_2. According to the measurements, the situation is the opposite. An excess of NO-molecules cause the O_3 mixing ratio to approach zero at night.

It should be noted, however, that a model with 1 km $\times$ 1 km grid resolution is not expected to reproduce measurements at an "urban centre" station exactly. The measurements at Bloomsbury are influenced by NO emissions from the road 25 metres away, while NO emissions in the model are averaged over a grid square. This would lead to lower NO/NO_x ratio in the model than at the measurement site, which is in accordance with our results.

An important question that arise in this context is: will the differences between model results and measurements influence our analysis considering the problem at hand? Although the model results from TP1 are in relatively good agreement with the measurements, the results from TP2 will be affected by the lack of height information in our emission data. Still, we think that certain conclusions can be drawn from our study, but some degree of uncertainty must be taken into account.

4.3 Analysis of ozone chemistry and dependence on grid resolution

When urban scale processes are omitted in a CTM grid box, this will not only impact the level of air pollution within the certain grid box, but also in the surrounding grid boxes. Trace gases with lifetimes longer than a few hours will clearly have a regional effect. In addition to ozone perturbations, subgrid scale processes may also impact global tropospheric concentrations

[1] 5 of the stations did not have CO measurements

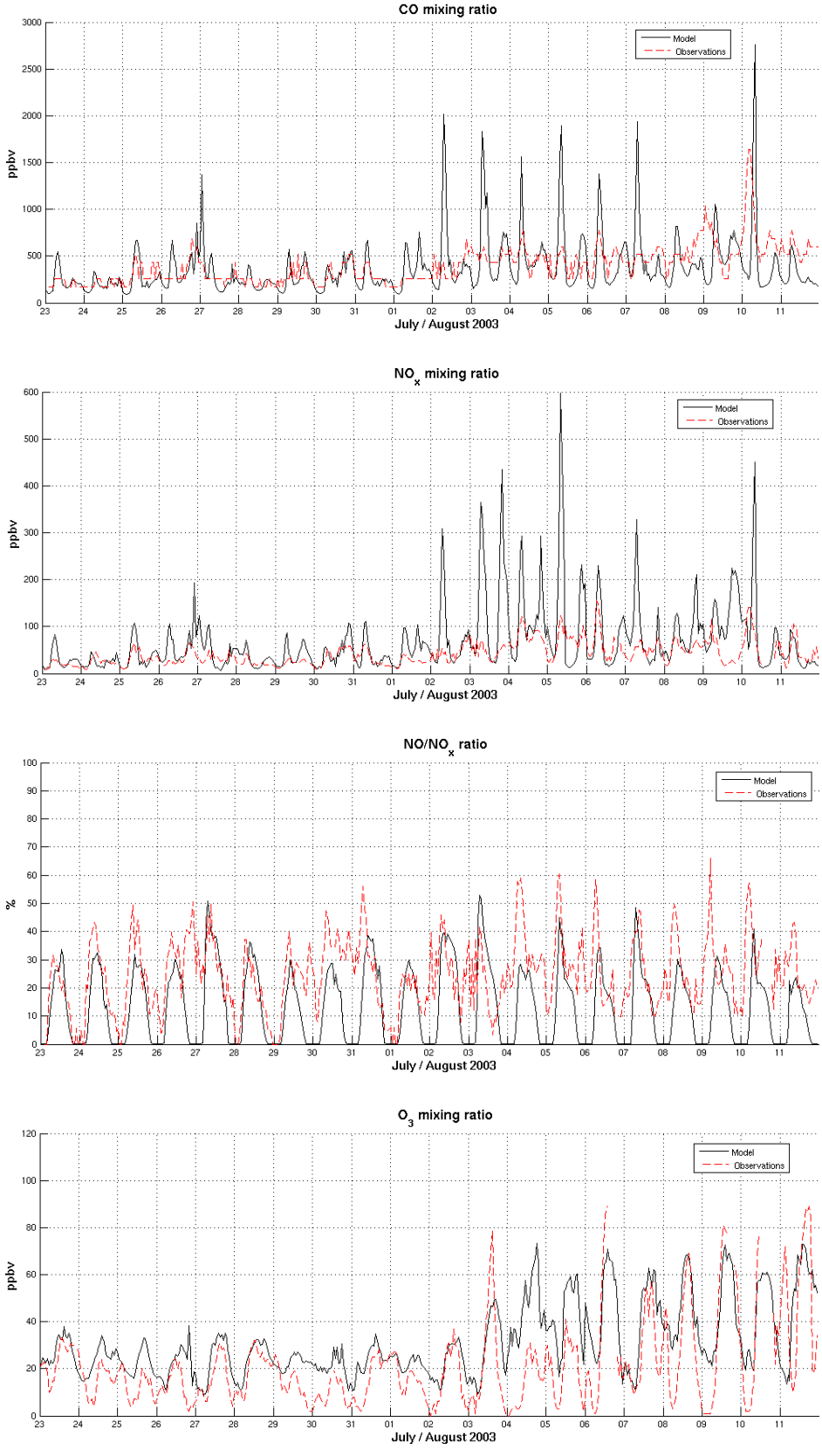

Figure 4.7: *As Figure 4.4, but at Bloomsbury, which is categorized as an "urban centre" station.*

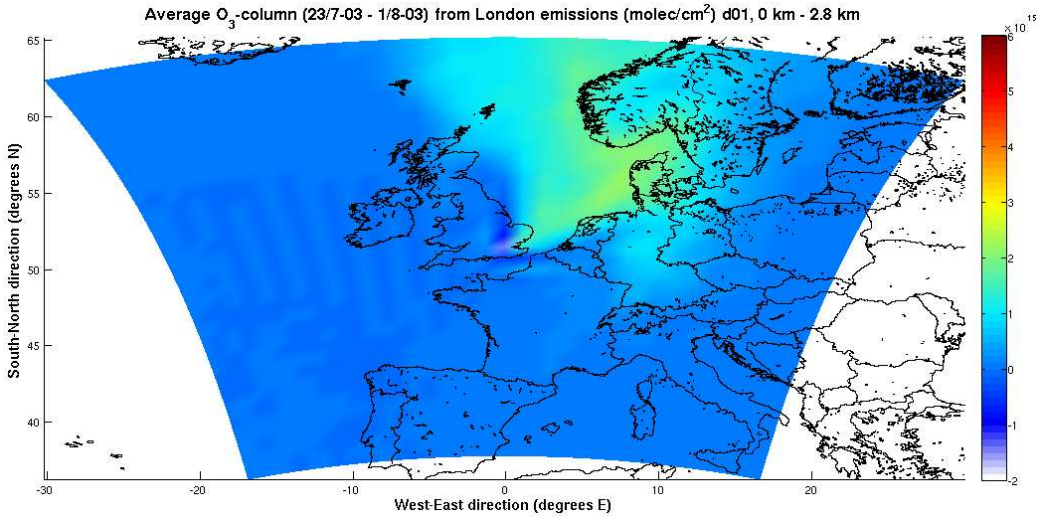

(a)

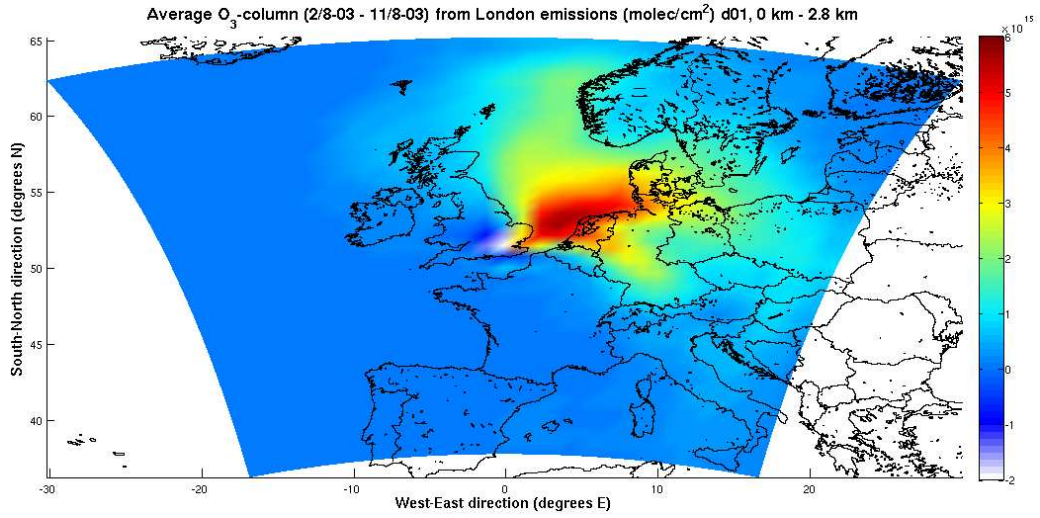

(b)

Figure 4.8: *Average regional impact on ozone column (molec* cm^{-2}*) caused by London emissions (AF - NF) during (a) TP1, and (b) TP2. The column is integrated from the ground to approximately 2.8 km height. The values are calculated from domain 1 results (81 km* $\times$ *81 km), which almost equals the grid resolution of a* $1^\circ \times 1^\circ$ *CTM run.*

of OH and thereby methane (CH_4), but the focus in this thesis is changes in ozone concentrations. As an example, Figure 4.8 shows the regional ozone contribution caused by London emissions (run AF-NF). The ozone column values are averaged over the 10 days in each time period. Due to a shift in weather conditions, there are substantial differences between the two periods. In TP1 (Figure 4.8a), the London emissions contribute to ozone formation far from the source region, and probably outside the domain as well. The largest contributions find place over the North Sea and Skagerrak. Less advection in TP2 (Figure 4.8b) gives a smaller receptor area, but with higher values. The area of largest ozone column contribution is now located just east of the English coast. In the vicinity of London, results from both time periods show a reduction in the ozone column. This is due to high NO_x levels and relatively low levels of VOCs (VOC-limited regime), which could lead to ozone depletion as mentioned in Section 2.2.5.

Sillman (1995) suggests a value of 0.28 for the ratio CH_2O/NO_y (NO_y = NO + NO_2 + HNO_3 + PAN + NO_3 + $2N_2O_5$) as a transition between NO_x and VOC limited regimes in urban locations. Figure 4.9 shows that O_3 production is generally VOC limited in London ($CH_2O/NO_y < 0.28$), but there are differences between the two time periods. During TP1 (Figure 4.9a), wet deposition effectively removes HNO_3, which is the most abundant reservoir species of NO_x. Because precipitation is almost non-existent during the latter 10 days, the ratio of CH_2O to NO_y will be lower in TP2 compared to TP1 (Figure 4.9b). Obviously, the distribution of emissions is also important in determining the regimes. From the plots we see that a large VOC emission source in the southwest leads to a NO_x limited regime ($CH_2O/NO_y > 0.28$) in that area, even during the second time period. It is important to note that the CH_2O/NO_y ratio only gives an indication of the VOC and NO_x limited regimes. Also, in Figure 4.9 we have averaged the values over 10 days, while the instantaneous values could be far from the average.

The horizontal grid resolution used in Figure 4.8 is close to the $1^\circ \times 1^\circ$ resolution often used in CTM simulation, meaning that urban scale processes are neglected. In this study, we will not investigate the regional or global effects when subgrid scale processes are taken into account. Instead, changes within the urban domain will be examined and quantified, and the effective emission factors derived here may later be implemented in the Oslo-CTM2 to study the importance of including urban scale effects in a regional or global model.

Effective emission factors will only be calculated for the innermost 81 km × 81 km, which is approximately the size of a CTM grid square. This is also the area we will focus on in the following analysis and is shown in Figure 4.10a. For the chemical species, we have calculated column values from the surface and up to approximately 2.8 km height. This height is chosen because we want to capture everything inside the PBL. In the model, the daytime PBL height rarely exceeds 2 km, so our column height of 2.8 km will be a safe

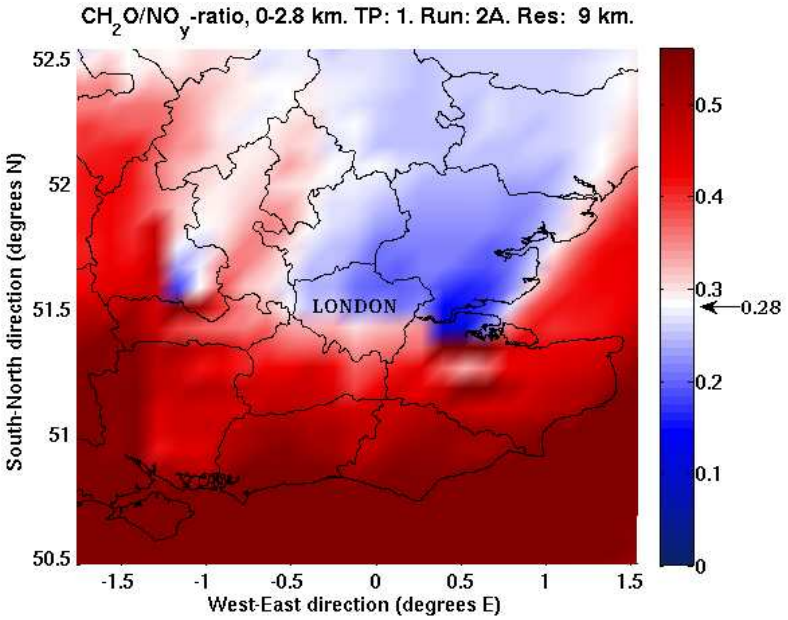

(a)

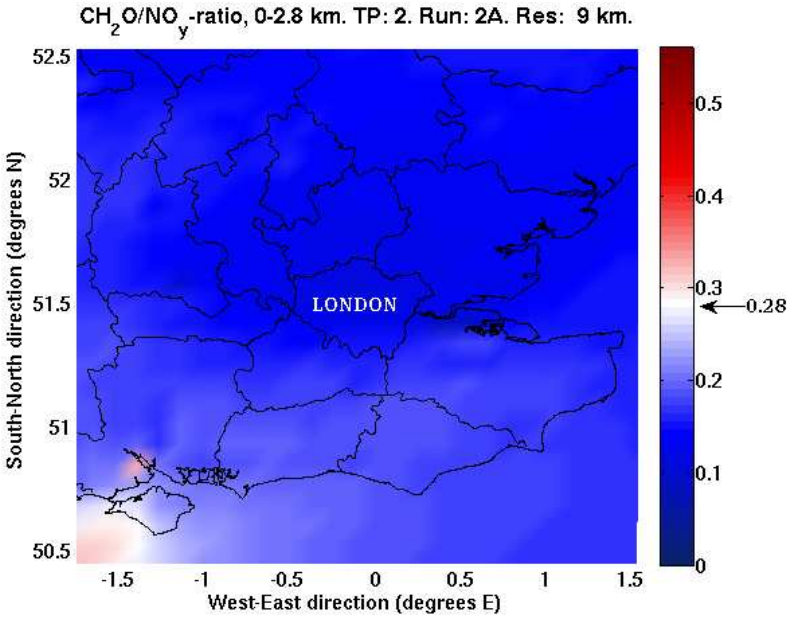

(b)

Figure 4.9: *Calculated CH_2O/NO_y ratio ($NO_y = NO + NO_2 + HNO_3 + PAN + NO_3 + 2N_2O_5$) from column values in the southeast of England during (a) TP1 and (b) TP2.*

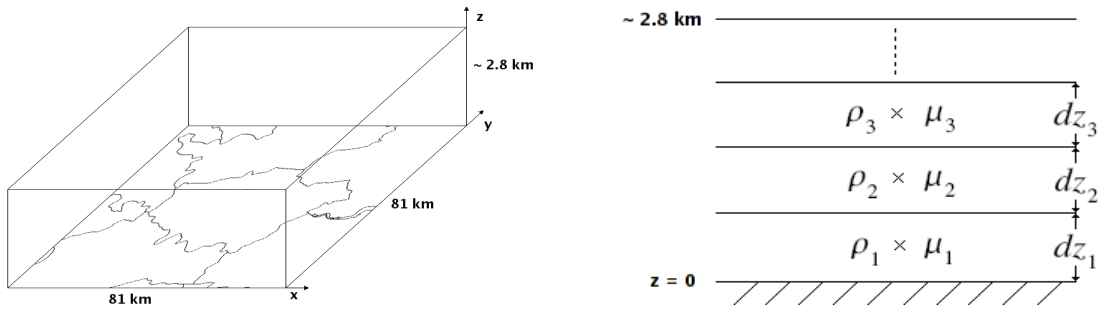

Figure 4.10: *(a) The focus area of the analysis. Column values are calculated from the ground and up to approximately 2.8 km. (b) Model output of air density (ρ) and mixing ratios (μ) in each vertical layer are used in the calculation of column values. (Note: The figures are not to scale.)*

choice. It should be noted that the height of each vertical layer varies in both time and space, meaning that the height of the ninth vertical layer, which we approximate to 2.8 km, is not exactly the same at all times and all locations. However, the difference from our method compared to using an exact height of 2.8 km has been investigated, and proved to be negligible.

The output from the model gives ppmv values of the chemical species in each grid box. We have converted these mixing ratios to concentrations (molecules/cm^3) and then integrated with height to obtain column values (molecules/cm^2). The conversion is illustrated in Figure 4.10b and can be expressed in the following formula:

$$Column = \int_0^{\sim 2.8 \text{ km}} \mu \; n_a \; dz \tag{4.1}$$

where μ is the mixing ratio of a chemical species, and n_a is the number density of air.

Changes in horizontal grid spacing also imply temporal changes. In the following analysis, however, we have not emphasized the impact of reducing the time step, but this effect is included in the presented results. Also, since the meteorological conditions are quite different in the two time periods, we will conduct the analysis for each time period separately.

4.3.1 Time period 1 (July 23 - August 1, 2003)

Figure 4.11 shows the dependence on horizontal grid resolution for column values, due to London emissions, of components that are important in ozone chemistry. The most pronounced changes occur when the grid spacing is decreased from 81 km to 27 km. All of the components shown, except for OH,

have a lower total average value when the resolution is increased to 27 km. Relative decreases from 81 to 27 km are 33.5%, 54.8%, 27.6%, and 24.7% for NO_x, NO_y-NO_x, CH_2O, and CO, respectively. It is difficult to explain these relatively large changes only with chemical reactions since NO_x and all the primary VOCs have lower values. Even CO, which is relatively long-lived compared to NO_x and VOCs, decreases from 81 km to 27 km.

A possible reason to the changes from 81 km to 27 km horisontal resolution is that the distribution of emissions is better in the 27 km case. A comparison of results from the runs with fine emissions versus the runs conducted with coarse emissions in all domains will indicate the importance of emission resolution versus meteorology. Figure 4.12 shows results from the runs with coarse emissions (run AC-NC). Still focusing on the 27 km resolution, we see that the results are almost identical to the simulations performed with finer emission resolution (Figure 4.11). The relative decreases from 81 to 27 km are now 30.8%, 49.7%, 29.0%, and 29.3% for NO_x, NO_y-NO_x, CH_2O, and CO, respectively, which are close to the numbers obtained with the AF-NF simulations. Hence, changes in emission resolution do not explain the column value differences between 81 km and 27 km.

Figure 4.13 shows average values of some meteorological variables and the dependence on grid resolution. As with the chemical values, the differences are largest when the resolution changes from 81 to 27 km. The changes in NO_2 photolysis rate are most probably caused by better representation of cloud cover as the resolution becomes better. Relative humidity, total precipitation and wind speed only change slightly, while the PBL outward flux (m^2/s) shows a relatively large decrease from 81 to 27 km. In Geng et al. (2007), the outflow of the air mass through the PBL (F) is defined by

$$F = W \cdot PH, \tag{4.2}$$

$$W = \sqrt{u^2 + v^2}, \tag{4.3}$$

where W represents the magnitude of horizontal wind speed in the PBL (m/s), u and v represent the wind speeds (m/s) in longitudinal and latitudinal directions, respectively, and PH represents the PBL height (m). Obviously, the change in PBL outward flux is linked to the change in PBL height. Average PBL height decreases from a value of 542 m to 401 m, but this does not explain the large decrease in the chemical column values. A deeper PBL in the 81 km resolution gives a larger air mass outward flux through the PBL and hence, the concentrations of chemical species caused by London emissions should be lower. As seen from Figure 4.11 the 81 km resolution is associated with higher concentrations, and consequently there must be other factors responsible for the changes.

From Figure 4.11 we see that the differences between 27 km, 9 km, and also 3 km horizontal grid resolutions are rather small compared to the changes from

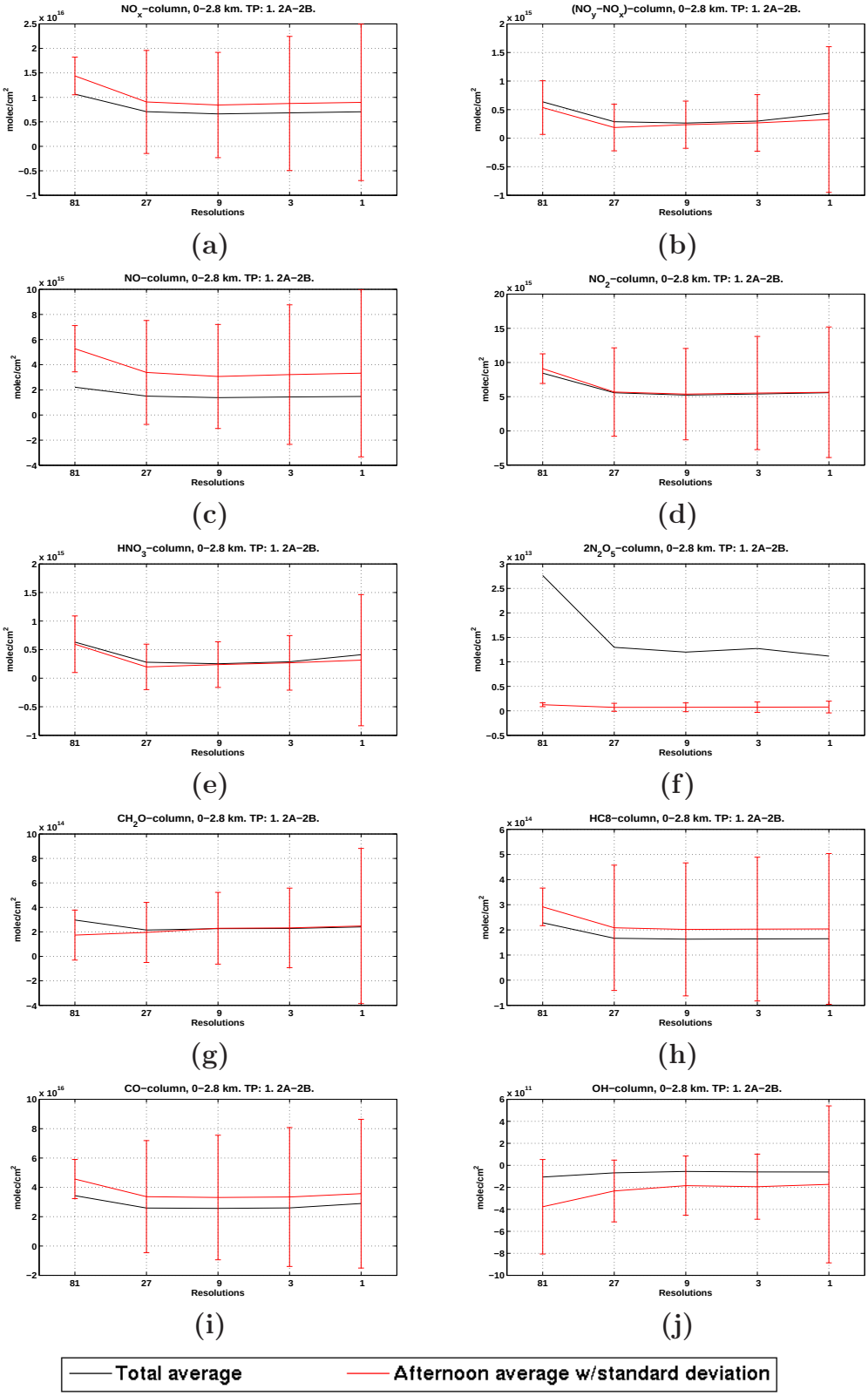

Figure 4.11: *Total average (black line) and afternoon average with standard deviation (red line) of column values of (a) NO_x (=NO+NO_2), (b) NO_y-NO_x (where NO_y=HNO_3+PAN+NO_3+$2N_2O_5$+HNO_2+HNO_4+TPAN), (c) NO, (d) NO_2, (e) HNO_3, (f) $2N_2O_5$, (g) CH_2O, (h) HC8, (i) CO, and (j) OH inside the LMA. Horizontal grid resolutions are shown along the x-axis. All values are calculated from only London emissions (run AF-NF), and are averaged based on hourly output for each grid cell.*

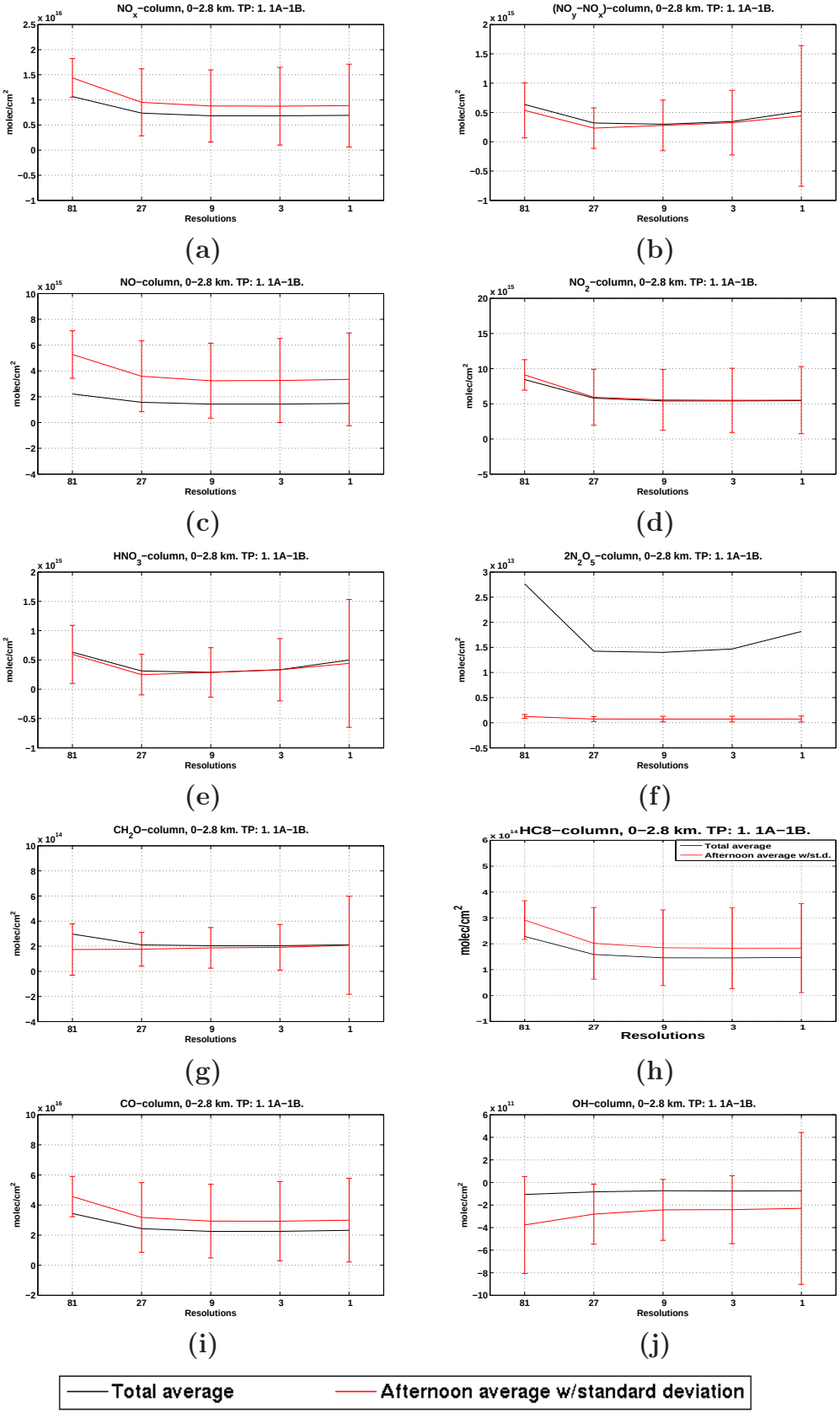

Figure 4.12: *As Figure 4.11, but with coarse emissions (81 km × 81 km) in all domains (run AC-NC).*

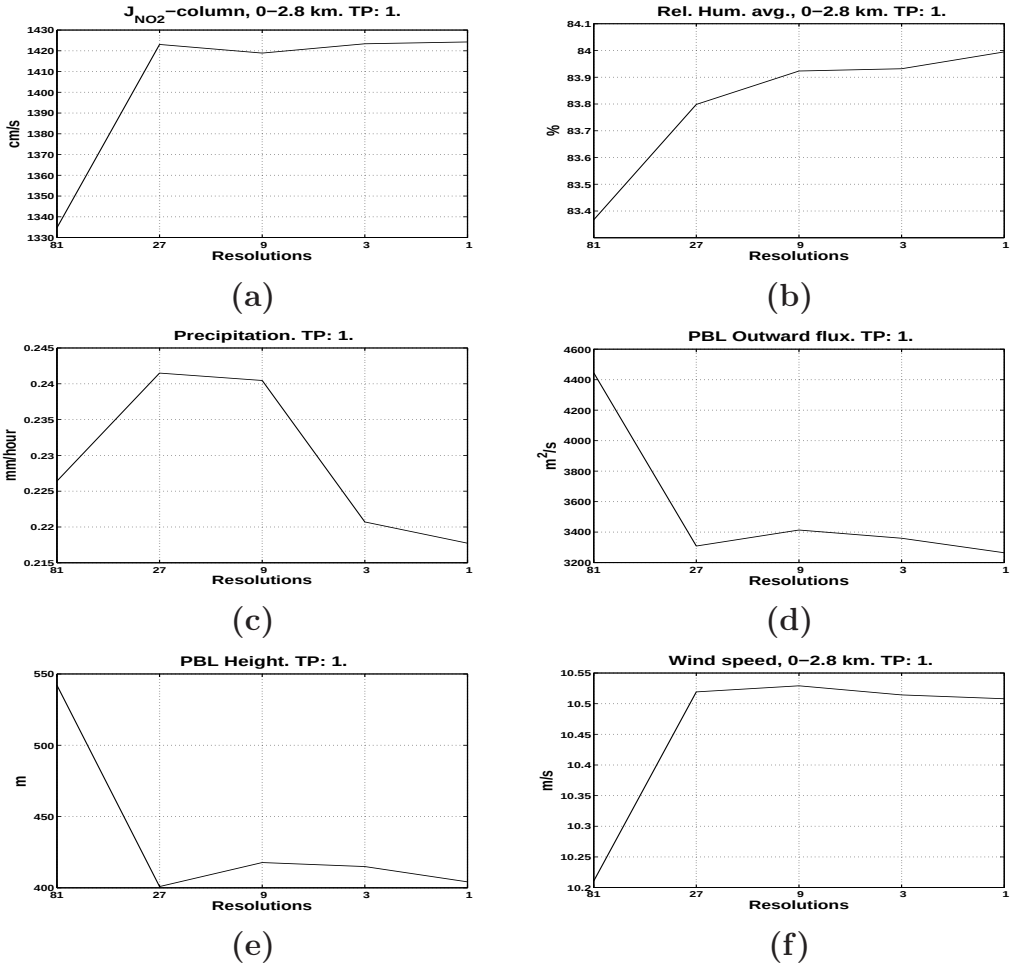

Figure 4.13: *Total average of (a) photolysis rate of NO_2 (column value expressed in cm/s) (b) relative humidity (%), (c) precipitation (mm/hour), (d) air mass outward flux through the PBL (m^2/s), (e) PBL height (m), and (f) wind speed inside the LMA. Horizontal grid resolutions are shown along the x-axis. Average values are based on hourly output for each grid cell.*

81 km to 27 km. Although the average values are almost constant between the 27 and 3 km resolution, the standard deviations of the afternoon average seem to increase for all the components shown in Figure 4.11. The reason is that the number of grid cells inside our study area increases as the resolution becomes finer, causing a larger spread in the column values. When the emissions are coarse in all resolutions, the variations in column values are not as large and consequently the standard deviations are smaller, as indicated in Figure 4.12.

A horizontal grid resolution of 1 km seems to alter the average column values in Figure 4.11 by a small amount. The increase from 3 km to 1 km are 3.3%, 45.9%, 5.8%, and 11.5% for column values of NO_x, NO_y-NO_x, CH_2O, and CO, respectively. The largest increase is by far in the NO_y-NO_x components with

HNO_3 as the major contributor. In the 1 km resolution case, HNO_3 constitute 94.4% of total NO_y-NO_x caused by London emissions. Even though $2N_2O_5$ decrease from 3 km to 1 km, the values are too small to impact total NO_y-NO_x values. There are at least two factors that may explain the increase in HNO_3. First, the precipitation has a better resolution in 1 km and this could possibly lead to a decrease in the scavenging of HNO_3. Second, afternoon values of total OH from all emissions (run AF) increase by 7.3% from 3 km to 1 km and this may enhance the daytime production of HNO_3 by the reaction

$$NO_2 + OH + M \rightarrow HNO_3 + M \tag{4.4}$$

Contrary to the 81 km→27 km changes, the differences between 3 km and 1 km can be explained, at least partly, by changes in emission resolutions. Results from the coarse emission simulations (Figure 4.12) show smaller differences for most components, but an intensification in the HNO_3 changes compared to the simulations with fine emissions. The increases from 3 to 1 km with coarse emissions are 1.3%, 50.6%, 3.5%, and 3.0% for column values of NO_x, NO_y-NO_x, CH_2O, and CO, respectively.

Figure 4.14 shows average column values of ozone caused by London emissions. In 81 km resolution the average net ozone column is $-1.423 \cdot 10^{15}$ molec/cm^2, meaning that London emissions cause ozone titration inside the LMA. The reason for the negative ozone values is an excess of NO_x compared to VOC. When the resolution is increased to 27 km, NO_x values decrease more than VOC values, and hence the titration of ozone is not as strong. Additionally, afternoon values of CH_2O actually increase from 81 to 27 km resolution (Figure 4.11g). This may, at least partly, explain the increase in ozone values due to the fact that ozone photochemistry is most active in the afternoon. The emission resolution do not seem to influence the level of ozone significantly at 27 km resolution. Total average of net ozone with fine emissions (Figure 4.14a) and coarse emissions (Figure 4.14b) are rather similar at 27 km resolution, showing values of $-4.385 \cdot 10^{14}$ molec/cm^2 and $-5.319 \cdot 10^{14}$ molec/cm^2, respectively.

Changes in resolution from 27 km to 9 km, and even to 3 km resolution, do not seem to impact the total average values of net ozone significantly. The values are rather constant and still almost unaffected by changes in emission resolutions. However, results from the 1 km grid resolution show pronounced changes in ozone column values. As seen in Figure 4.14a, the net ozone effect is now positive with an average column value of $1.748 \cdot 10^{15}$ molec/cm^2. Values of other chemical components (Figure 4.11) do not nearly indicate this level of change, so the O_3 results must be a consequence of nonlinear effects within the ozone chemistry, or differences in meteorological factors. We see from Figure 4.14b that the changes are much smaller with coarse emissions, and thus the resolution of the emissions is a key in explaining the ozone changes.

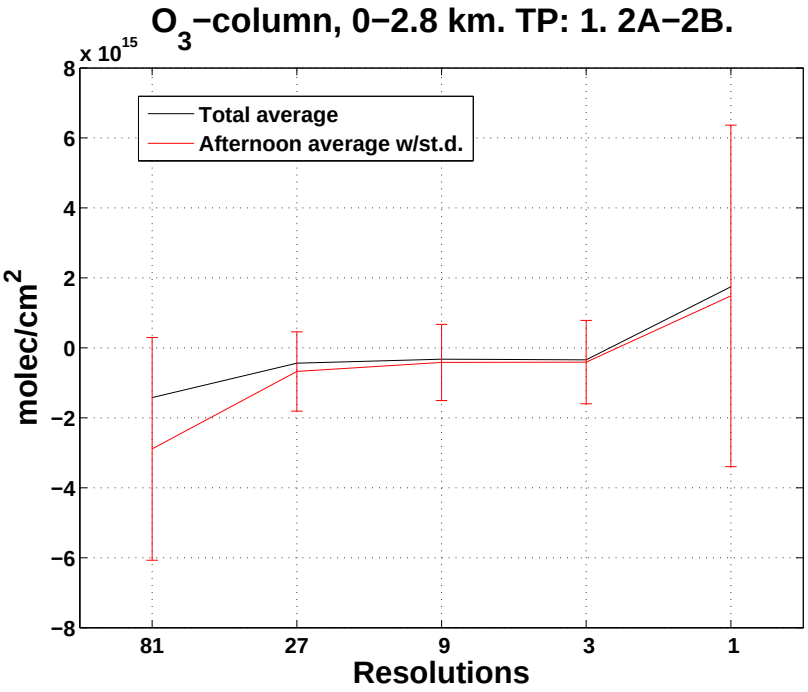

(a)

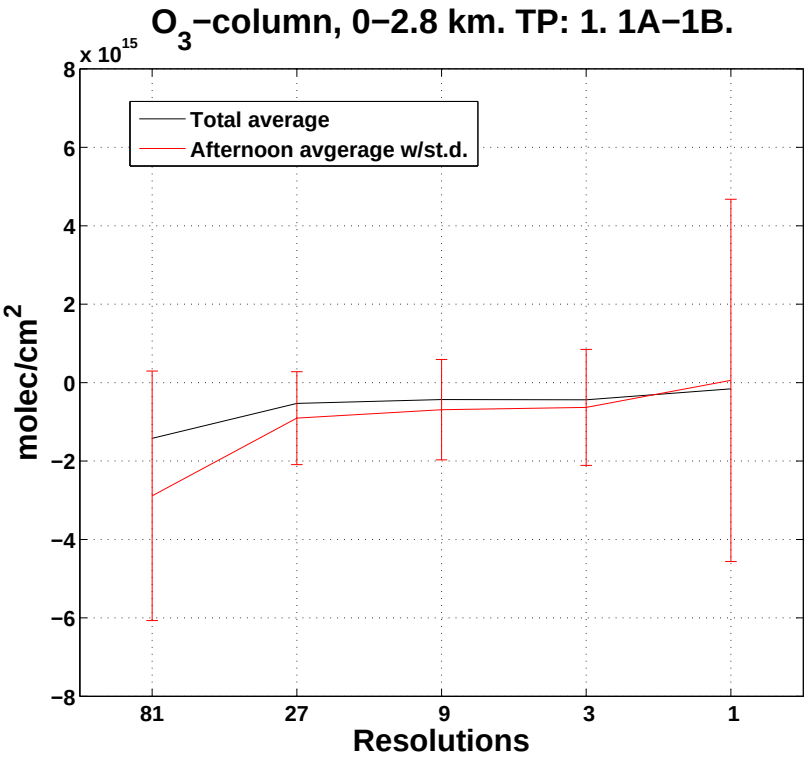

(b)

Figure 4.14: *Total average (black line) and afternoon average with standard deviation (red line) of column values of net ozone caused by London emissions with (a) fine emission resolutions (AF-NF), and (b) coarse emission resolutions (AC-NC) inside the LMA. Horizontal grid resolutions are shown along the x-axis. All values are averaged based on hourly output for each grid cell.*

By rearranging Equation (4.1) and assuming constant air density we get

$$\bar{\mu}_{\Delta O_3} \approx \frac{Col_{\Delta O_3}}{\bar{n}_a \Delta z} = \frac{3.171 \cdot 10^{19}\ [\text{molec m}^{-2}]}{2.288 \cdot 10^{25}\ [\text{molec m}^{-3}] \cdot 2,800\ [\text{m}]} \approx \underline{\frac{1}{2}\ [\text{ppbv}]} \quad (4.5)$$

where $\bar{\mu}_{\Delta O_3}$ is average difference in net O_3 mixing ratio caused by London emissions, $Col_{\Delta O_3}$ is average difference in net O_3 column caused by London emissions, $\bar{n}_a$ is approximate number air density in the column, and Δz is the column height of approximately 2.8 km. We see from (4.5) that the change in horizontal grid spacing from 81 km to 1 km cause an average change in O_3 mixing ratio of $\sim \frac{1}{2}$ ppbv within the LMA. Although this value seems rather insignificant, the global change in O_3 concentrations may still be large if urban scale processes from all megacities are accounted for.

Interestingly, Cohan et al. (2006) found that the average surface ozone concentration in the Atlanta region only differed slightly between the horizontal grid resolutions of 36 km, 12 km, and 4 km, and suggested that model error for simulating regional ozone formation is driven by other factors than grid resolution, at least on these scales. Although we found differences when changing the resolution from 81 km to 27 km and from 3 km to 1 km, their conclusion is in agreement with our analysis if we approximate our results from the resolutions of 27 km, 9 km, and 3 km to their 36 km, 12 km, and 4 km resolution results.

Additionally, our results are in compliance with Mayer et al. (2000) who found that implementing an urban chemistry model into a global chemistry-climate model caused more ozone production in urban domains. It should be noted, however, that their study is only comparable to our results in a certain degree, since they considered a large number of urban areas and a simulation period of more than 100 years. They focused on the long-term impact of urban air pollution on global chemistry and climate, and found that when urban scale processes were included, the global tropospheric ozone mole fraction was lower.

4.3.2 Time period 2 (August 2 - August 11, 2003)

Although the meteorological conditions are different in TP2 compared to TP1, the results show similar trends in both periods. To avoid repetition, we have in this section chosen to focus on the differences between the time periods, and to elaborate on the causes to the model results.

The plots in Figure 4.15 confirm that results from the second time period have the same trend as results from the first time period. However, the scales are quite different because the reduced advection during this period gives a larger impact of London emissions inside London. A lower amount of chemical components is transported out of the LMA, and consequently the trace gases have more time to build up to higher concentrations. Due to this fact, more NO_x will transform into other NO_y components. In TP2, the amount of NO_y represented as NO_x is 84 %, compared to 94 % in TP1.

The impact from London emissions on O_3 column values is given in Figure 4.16. Again, the trend is the same as in TP1 with net ozone destruction on the scales 81 km→3 km, and net ozone production when 1 km resolution is used. Net ozone values from London emissions are now -5.166×10^{15} molec/cm^2 and 4.515×10^{15} molec/cm^2 for the scales 81 km and 1 km, respectively. As with the chemical components shown in Figure 4.15, the absolute values of ozone are much larger in TP2 than in TP1. If the same procedure as in Equation (4.5) is used, we get for TP2 an average change in O_3 mixing ratio ($\bar{\mu}_{\Delta O_3}$) caused by London emissions, within the LMA, of $1\frac{1}{2}$ ppbv, which is three times higher than the corresponding TP1 value.

A meteorological factor that is particularly important in urban ozone chemistry is the PBL height. As seen in Figure 4.17, which shows average PBL height in southeast England, there are significant differences between the 81 km and 27 km resolutions. The PBL height inside the LMA (inner square in Figure 4.17a) is relatively large in the 81 km case with a value of 500 m. Due to better resolution of terrain data in 27 km, the average PBL height in LMA is now 385 m with maximum in the inner square. Probably, the deep boundary layer over London is a result of the urban heat island effect causing temperatures to get higher inside the city compared to surrounding areas. These temperature differences arise principally because the surface types in an urban area (e.g. asphalt and concrete) have different thermal properties than surface types in rural areas (e.g. trees, grass and plants), often leading to higher temperatures in the city. Also, urban areas are associated with less vegetation, and hence, less cooling by evapotranspiration will occur. This warming may generate convective winds within the urban boundary layer, and it is important to have a rather fine model resolution if these winds are to be described accurately.

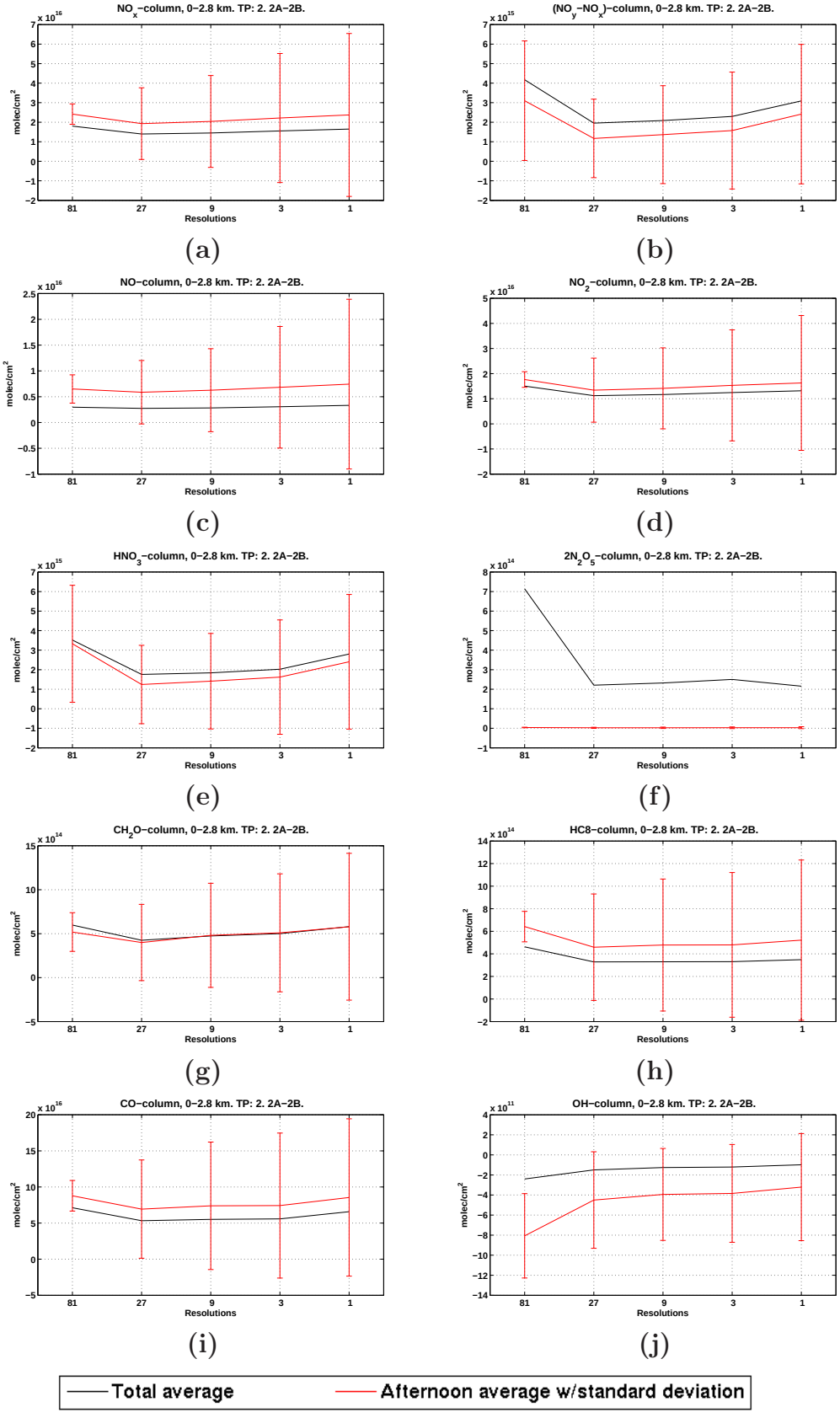

Figure 4.15: *As Figure 4.11, but for TP2.*

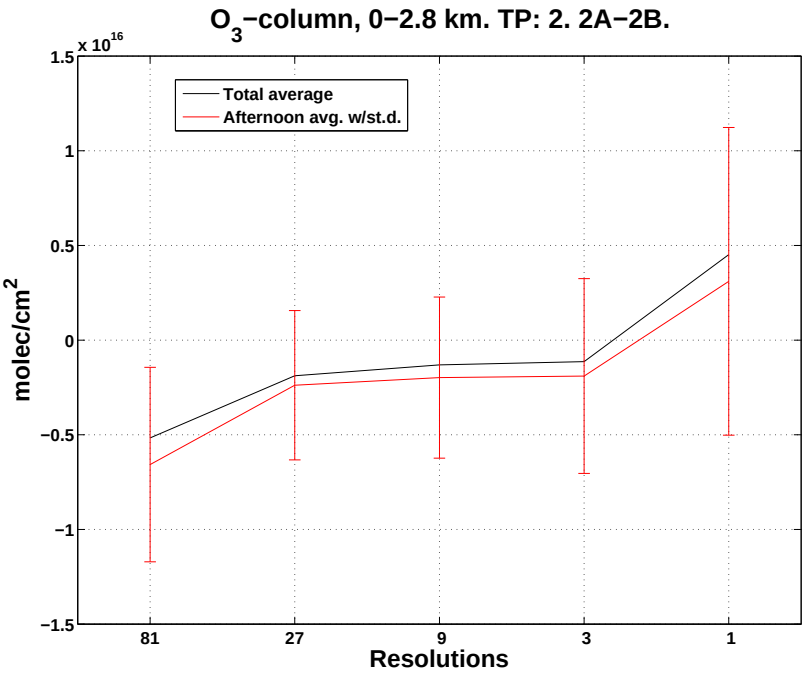

(a)

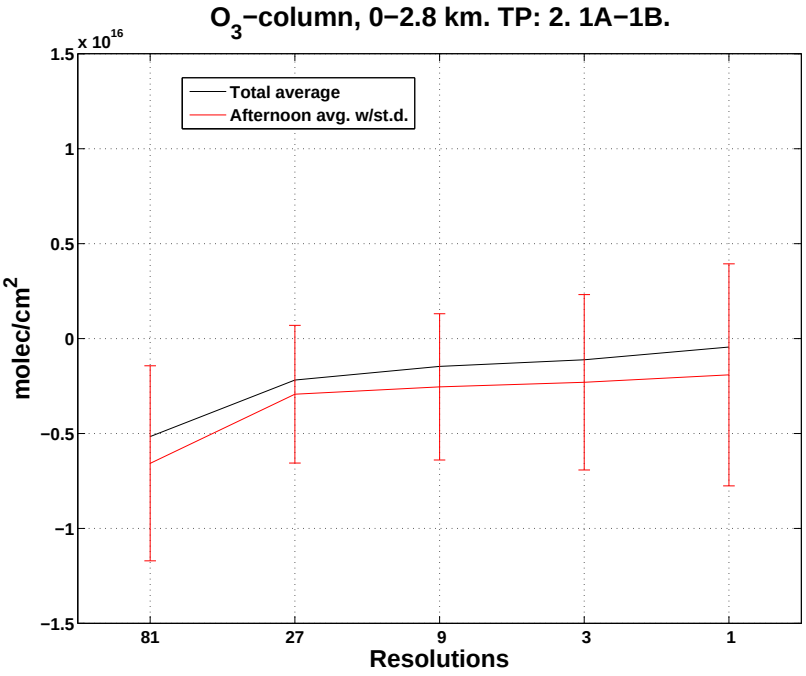

(b)

Figure 4.16: *As Figure 4.14, but for TP2.*

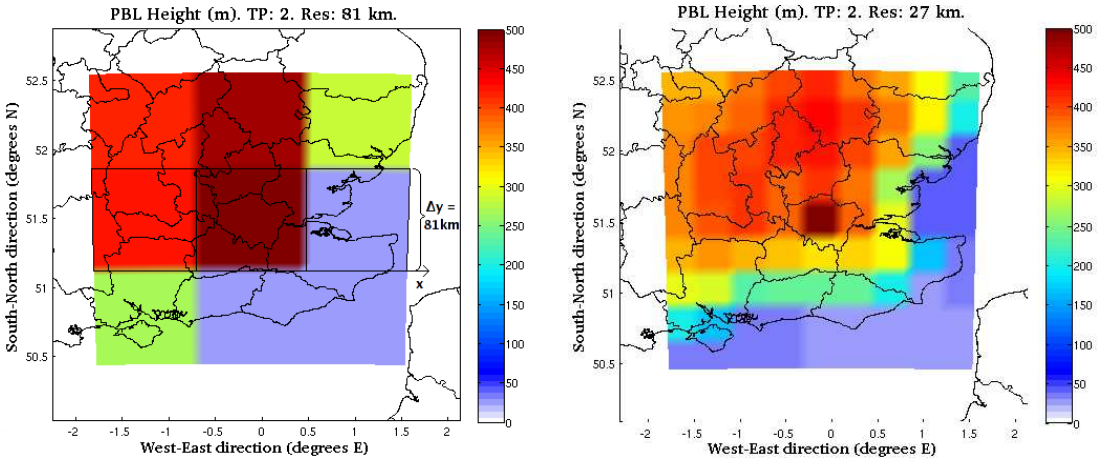

Figure 4.17: *Average PBL height during TP2 in southeast England when (a) 81 km, and (b) 27 km grid resolution is used.*

Another interesting fact in Figure 4.17 is that the surface type in the grid boxes south and east of the LMA is considered to be water in 81 km resolution, and consequently the PBL height is only 30-40 m on average. Again, the better resolution of terrain data in the 27 km case gives a smoother PBL transition from the urban area of London and to the sea. These differences in PBL height could lead to different wind patterns on different scales, and may partly explain the decrease in chemical column values when changing the resolution from 81 km to 27 km (Figure 4.15).

Transport of chemical species is not only governed by the wind, but is also dependent on the concentration gradient of the species. Advection of a trace gas with mixing ratio μ is given by

$$\mathbf{v}_H \cdot \nabla\mu = u\frac{\partial\mu}{\partial x} + v\frac{\partial\mu}{\partial y} \tag{4.6}$$

where $\mathbf{v}_H$ is the horizontal velocity vector, u is the wind component in x-direction, and v is the wind component in y-direction. A possible reason for the decreased transport in 81 km compared to 27 km resolution is that larger gradients of chemical species directed out of LMA may exist near the ground in the latter case. As seen from Equation (4.6), larger gradients ($\nabla\mu$) will cause transport by advection to increase. Trace gas concentrations in the grid boxes surrounding the LMA are generally lower because of less emission activity, but with the 81 km resolution, surface concentrations east and south of London may still be large due to the low PBL height (Figure 4.17).

Figure 4.18 illustrates our theory that could explain the increased transport out of London when 27 km resolution is used. During the day, the shallow PBL east of London in 81 km resolution (Figure 4.18a) causes surface

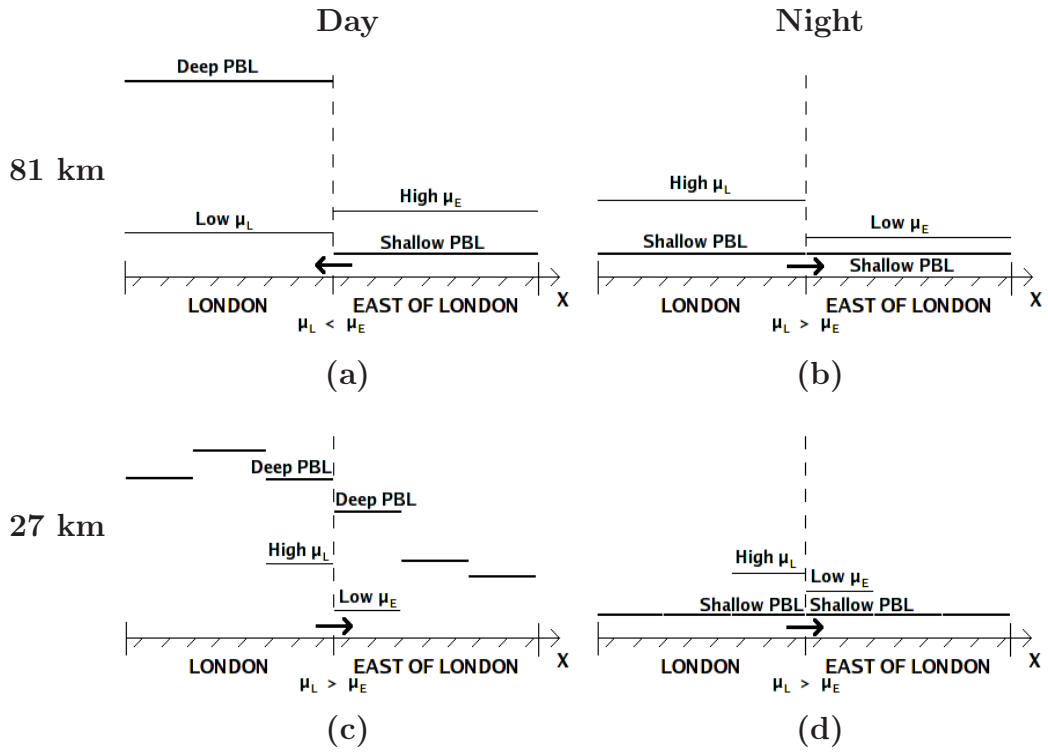

Figure 4.18: *Schematic illustration of PBL height (thick line) and surface mixing ratio (thin line) in the grid boxes closest to the eastern border of LMA. One example is given for each of (a) daytime situation with 81 km resolution, (b) nighttime situation with 81 km resolution, (c) daytime situation with 27 km resolution, and (d) nighttime situation with 27 km resolution.* μ_L *is the mixing ratio of a trace gas in the most eastern grid box within the LMA, and* μ_E *is the mixing ratio in the grid box just east of LMA.*

mixing ratios (μ_E) to become large. Inside the London grid box, pollutants are diluted throughout a deep PBL causing surface mixing ratios (μ_L) to be lower than east of London ($\mu_L < \mu_E$). If this is the case, the direction of the gradient at the surface, where the mixing ratios are highest, is actually directed from the east of London towards the London grid box. When 27 km resolution is used, however, the PBL height just east of London is relatively deep (Figure 4.18c). As a consequence, pollutants are diluted over a larger vertical area, and because emissions are larger in London we have $\mu_L > \mu_E$. Contrary to the 81 km case, the concentration gradient at the surface is now directed outwards from London. At nighttime, there are no significant differences between the resolutions (Figure 4.18b, d). Since the boundary layer is shallow in both cases, emission is the dominant process, and causes higher mixing ratios inside London compared to east of London.

We have checked our theory on surface mixing ratios of NO_x on August 2, 2003. The values are shown in Table 4.2. At the times when the PBL height

	81 km			27 km		
UTC	μ_L	μ_E	$\nabla\mu$	μ_L	μ_E	$\nabla\mu$
00	42.0	18.4	$\rightarrow$	36.7	30.4	$\rightarrow$
06	49.6	26.5	$\rightarrow$	50.0	34.5	$\rightarrow$
12	9.6	28.1	$\leftarrow$	12.7	5.7	$\rightarrow$
18	14.2	31.2	$\leftarrow$	20.9	15.4	$\rightarrow$

Table 4.2: *Surface mixing ratios of NO_x inside London (μ_L) and just east of London (μ_E), together with the direction of the gradient ($\rightarrow$ is eastward and $\leftarrow$ is westward), on August 2, 2003. Values are taken from the simulation where emissions have coarse resolution in all domains (run AC). In 27 km, μ_L and μ_E is averaged over three grid boxes in latitudinal direction ($\Delta y = 81$ km).*

is low (00UTC and 06UTC), the concentration gradient is similar for both resolutions, and has an eastward direction. When the boundary layer is deep over London (12UTC and 18UTC), the gradient has a westward direction when 81 km resolution is used, while the gradient still has an eastward direction when using the 27 km resolution. These results are consistent with our theory, but it should be noted that we have only checked the results for one component (NO_x) and for one day out of the ten days in the time period. Although we have not quantified the importance of this effect, we believe that it may explain some of the increased transport out of the LMA when 27 km resolution is used.

The same analogy could be used to investigate transport out of London in the north-south direction. We have compared surface mixing ratios of NO_x for the nearest grid boxes south of London on the same day as above (August 2, 2003). Results show that the concentration gradient has a southward direction in all cases except at 12UTC when it is directed northwards from the grid boxes south of London in 81 km resolution. Again, the results are consistent with our theory, but because of lower NO_x emissions south of London, values are smaller in magnitude than at the eastern border of the LMA.

Figure 4.19 shows an example of a time when the wind is different between the resolutions of 81 km and 27 km[2]. Because the differences are largest at the ground, this could have a large impact on pollutant transport since the highest concentration levels usually are found near the surface. At the time and heights shown in the plots, the wind direction is mainly in the longitudinal direction, and more specifically from east to west (Figure 4.19a, b). Near the surface west of London, the x-component of the wind vector is much stronger when 27 km resolution is used compared to 81 km. This is shown

[2]Animations of ΔU, ΔNO_x, and ΔO_3 for the whole simulation period can be found on http://folk.uio.no/oivinho/movies/

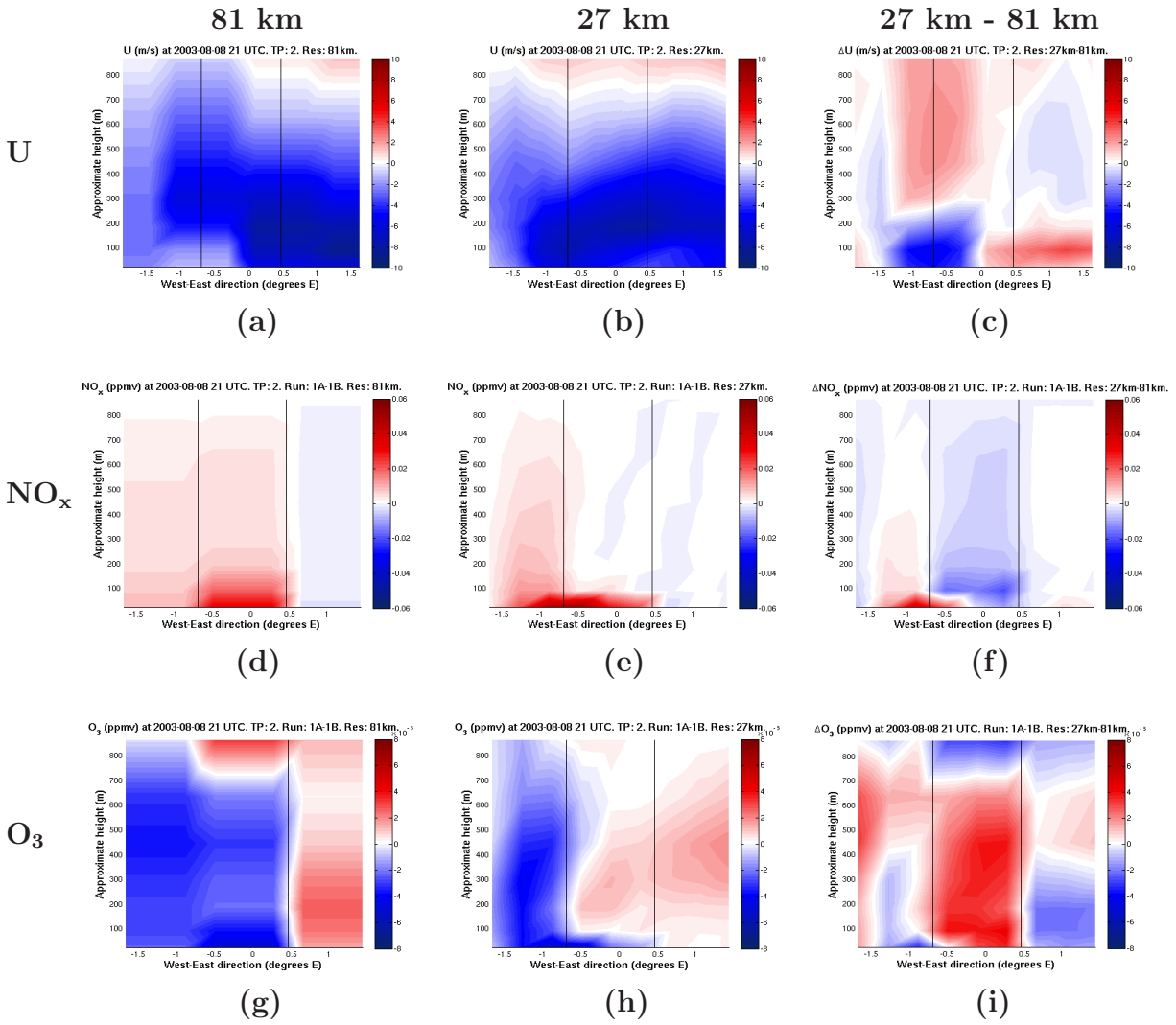

Figure 4.19: *Vertical sections of wind speed in x-direction (m/s) with horizontal grid resolutions of (a) 81 km, (b) 27 km, and (c) 27 km - 81 km (absolute difference); NO_x mixing ratio (ppmv) (run AC-NC) with resolutions of (d) 81 km, (e) 27 km, and (f) 27 km - 81 km; and O_3 mixing ratio (ppmv) (run AC-NC) with resolutions of (g) 81 km, (h) 27 km, and (i) 27 km - 81 km, on the 8th of August at 21UTC. The vertical sections are taken from the area marked in Figure 4.17a, and the values are averaged over $\Delta y = 81$ km in latitudinal direction.*

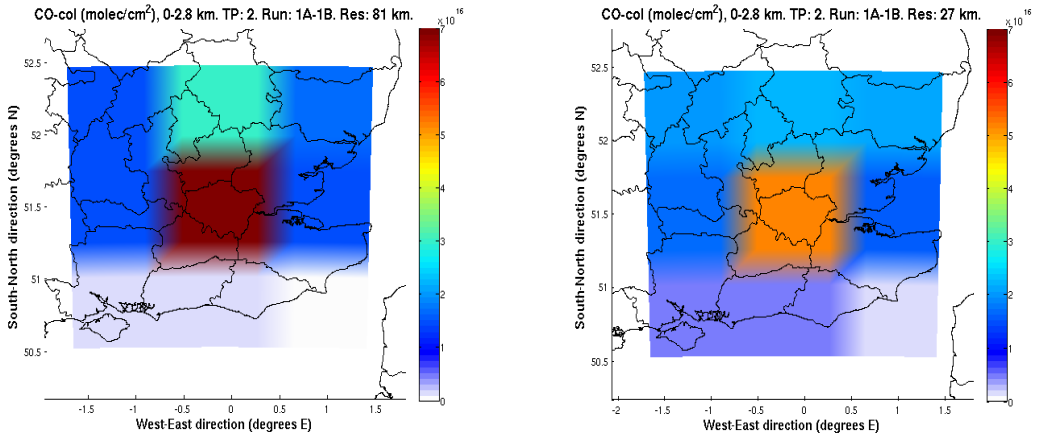

(a) (b)

Figure 4.20: *Column values of CO (molec/cm^2)) from London emissions (run AC-NC) with horizontal grid resolution of (a) 81 km, and (b) 27 km (regridded to 81 km).*

as the dark blue area ($\Delta U < 0$) in Figure 4.19c, and means that, in the 27 km case, larger amounts of chemical species from London emissions will be transported out of the LMA at this time. The dark red area ($\Delta NO_x > 0$) in Figure 4.19f shows that this is the case for NO_x since there is more NO_x near the surface west of London in the 27 km case. Also worth noting is the NO_x column over London in Figure 4.19d, which is almost non-existent above 100 m in Figure 4.19e. The reason is probably the PBL height which is, at this time, higher in 81 km than in 27 km resolution.

From the vertical sections we see that ozone is to a large degree anti-correlated with NO_x, at least near the ground (Figure 4.19g, h, i). More NO_x leads to net loss of ozone and vica versa. Also, the difference in PBL height between the resolutions is more evident in the vertical plots of ozone. Up to $\sim$ 700 m above London, net ozone value is higher in 27 km than in 81 km, shown as the dark red area ($\Delta O_3 > 0$) in Figure 4.19i. From $\sim$ 700 m and above (not shown in the figure), the situation is changed; less NO_x in 27 km leads to less ozone production. We saw the same effect in Figure 4.8 when there was net ozone production downwind of London. Most likely, this results from an increase in the ratio of VOC to NO_x, so that the combination of NO_x and VOCs now leads to net ozone production as shown in the isopleth in Figure 2.4.

Although the vertical sections in Figure 4.19 only represent one time frame of the simulation period, this effect of increased advection out of the LMA in 27 km resolution was found to occur almost every evening when the boundary layer breaks down. As a consequence, the abundance of chemical species

should be higher in the grid cells surrounding the LMA when 27 km resolution is used compared to 81 km. CO, which is relatively inert on an urban scale, is a better indicator of transport than NO_x and VOCs. Figure 4.20 shows average CO column values in and around the LMA when 81 km and 27 km resolution is used. From Figure 4.15i we already know that there is more CO in the LMA when 81 km resolution is used, and in Figure 4.20 we see that the column values in the grid cells surrounding London are larger in the 27 km case (except in the northern grid cell). Total time averaged CO from London emissions (run AC-NC) within the LMA were 4.67×10^{30} molecules and 3.41×10^{30} molecules for the scales 81 km and 27 km, respectively, giving a decrease of 27.0 %. When the eight surrounding boxes of size 81 km × 81 km were included in the calculation, corresponding values were 1.07×10^{31} molecules and 1.05×10^{31} molecules with 81 km and 27 km resolution, respectively. The decrease is now only 2.2 %, indicating that nearly all the "lost" CO in the LMA is captured when increasing the analysis volume in horizontal direction.

When applying the same analogy on NO_y, the result was different than with CO. An increase of the analysis volume in horizontal direction did not capture all the NO_y that was "lost" in the LMA with 27 km resolution. Possible differences in convection should be identified when increasing the volume in the vertical direction, but this did not change total NO_y values even when the height was increased to the top vertical layer of the model (50 hPa). A possible reason for the higher value of NO_y with 81 km resolution is underestimation of dry deposition due to coarse resolution of terrain data.

While the differences in chemical species from 81 km to 27 km resolution likely are caused by changes in meteorology, differences from 3 km to 1 km seem to occur mainly because of chemistry changes. Figure 4.21 shows the spatial distribution of average net ozone column from London emissions at different resolutions in meteorology and emissions. Since the wind direction is mainly from east during this period, the impact from the large NO_x source at Tilbury power plant can easily be seen when emissions have fine resolution (Figure 4.21a, b). When emissions are coarse (Figure 4.21c, d), net ozone is more homogeneously distributed, but some changes still occur between the 3 km and 1 km scales. These changes must be due to meteorological factors, but are minor compared to the changes associated with fine emission resolutions. A common fact in all the plots in Figure 4.21, is that net ozone columns are lower in the west than in the east. The reason is that we only observe the impact from London emissions, and consequently, easterly wind causes more NO_x to accumulate in the west, which again causes more ozone titration in this area.

Although Figure 4.21b gives a positive net ozone column, on average, it does not necessarily imply that more ozone production occurs with 1 km resolution than with 3 km resolution. Figure 4.22 shows that ozone destruction

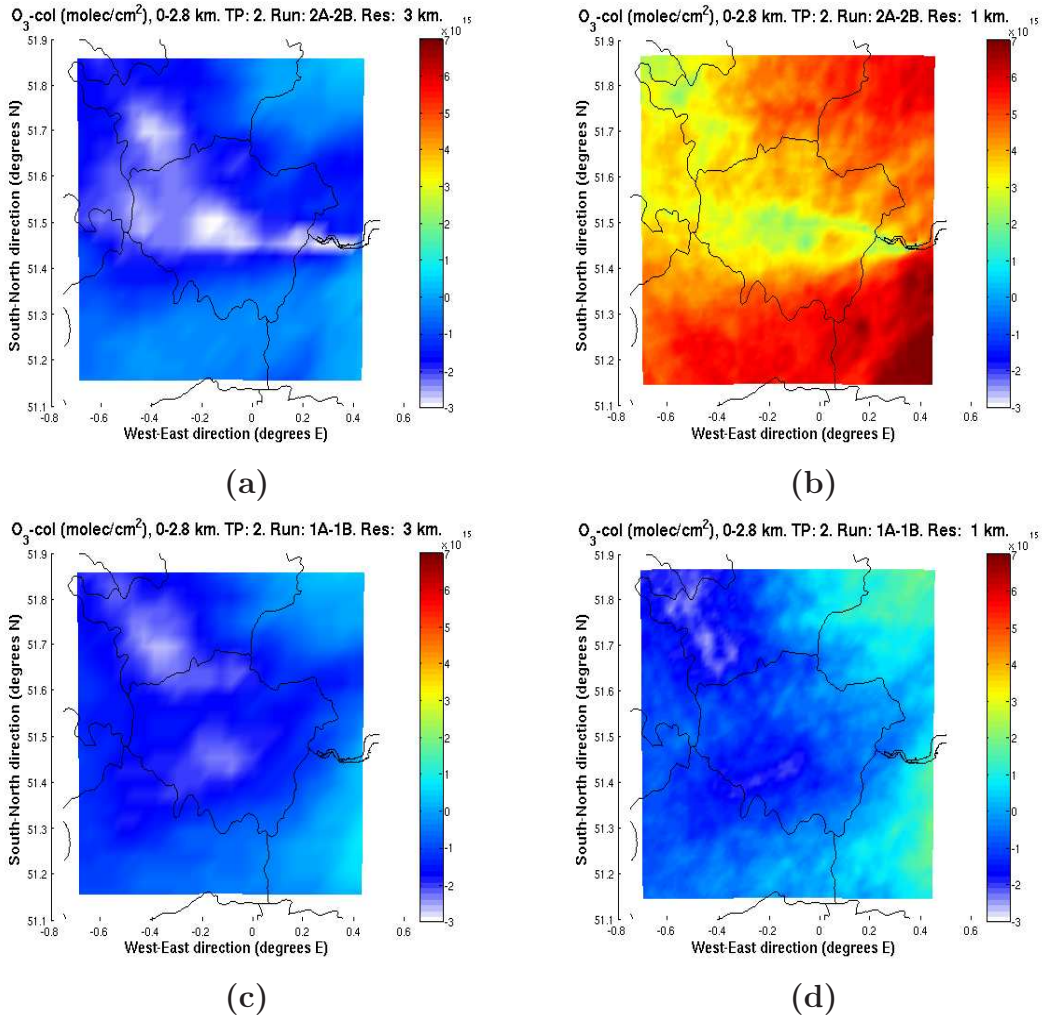

Figure 4.21: *Spatial distribution of average net ozone column (molec/cm^2) from London emissions (AF-NF) in (a) 3 km resolution, and (b) 1 km resolution, and with coarse emissions (AC-NC) in (c) 3 km resolution, and (d) 1 km resolution.*

does occur near the surface, also when 1 km resolution is used. As expected, most ozone titration takes place downwind and in the vicinity of Tilbury power plant. As mentioned earlier, ozone is produced several hundred meters above London. Probably, this production is rather unchanged between 3 km and 1 km resolution, while ozone destruction, however, is reduced when 1 km resolution is used.

Figure 4.23 shows a nighttime example of the difference in ozone titration due to changes in resolution. When the emissions have a resolution of 1 km (Figure 4.23b), the titration near Tilbury power plant is limited because ozone values reach zero ppbv, and hence the reaction

$$NO + O_3 \rightarrow NO_2 + O_2 \tag{4.7}$$

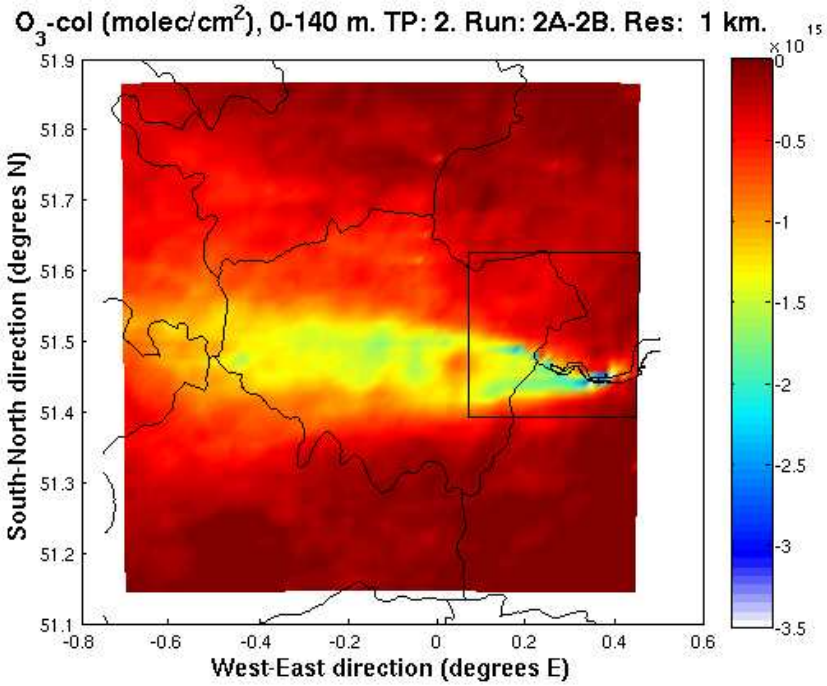

Figure 4.22: *Spatial distribution of average net near-surface (below ∼ 140 m) ozone column (molec/cm^2) from London emissions (AF-NF) when 1 km resolution is used.*

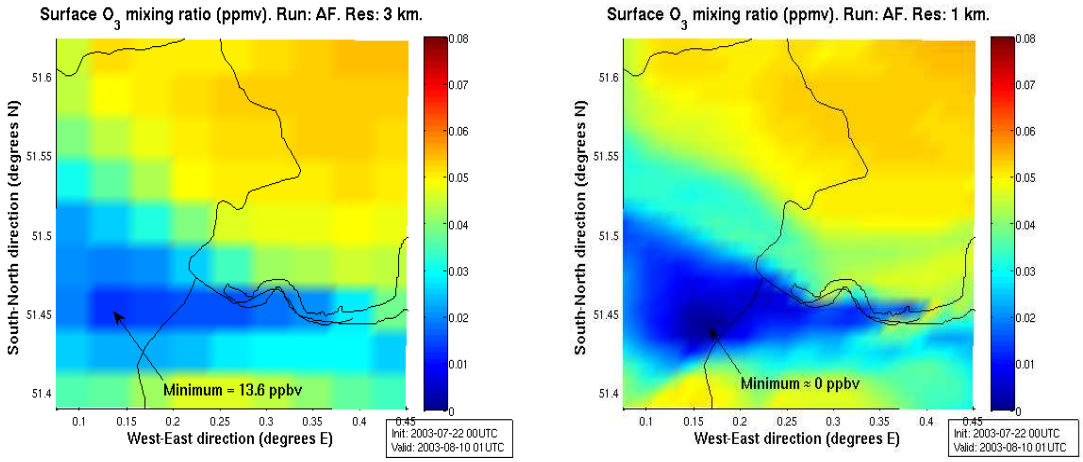

(a) (b)

Figure 4.23: *Distribution of surface ozone (ppmv) at 01UTC August 10, 2003 with (a) 3 km resolution, and (b) 1 km resolution. The results are taken from the lowest vertical layer in the simulation where all emissions are included (run AF). The area shown is marked in Figure 4.22.*

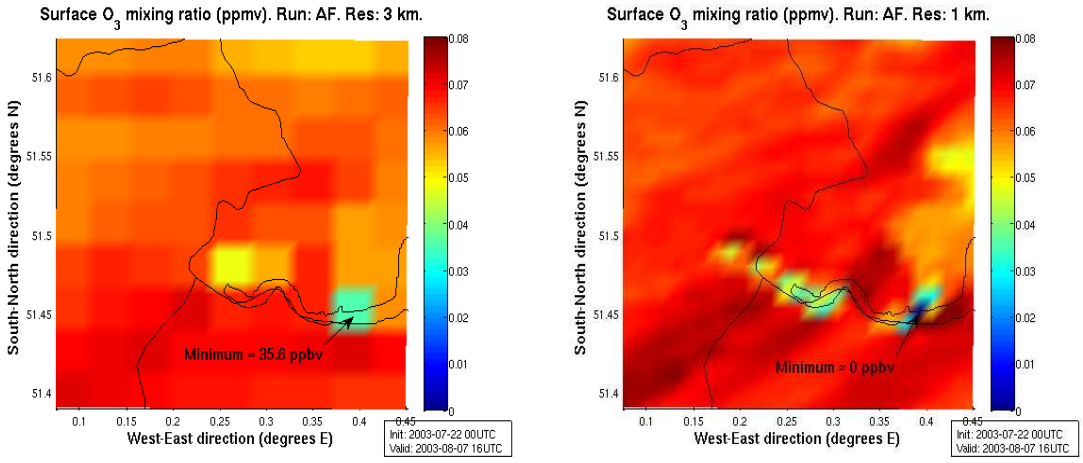

Figure 4.24: *Distribution of surface ozone (ppmv) at 16UTC August 7, 2003 with (a) 3 km resolution, and (b) 1 km resolution. The results are taken from the lowest vertical layer in the simulation where all emissions are included (run AF). The area shown is marked in Figure 4.22.*

breaks down. The minimum value of surface ozone at this time (01UTC August 10, 2003) is only 0.015 ppbv, while results from the 3 km resolution (Figure 4.23a) show a minimum of 13.6 ppbv.

Figure 4.24 shows that ozone titration occurs during the day as well. In 3 km resolution (Figure 4.24a), emissions from the power plant are divided among nine nearby grid cells compared to one grid cell in Figure 4.24b. Since the power plant is a point source, concentrations of NO_x in the one grid cell will be higher than when the emissions are divided among nine grid cells. Consequently, ozone titration occurs over a smaller area when 1 km resolution is used, and O_3 concentrations may reach zero ppbv. At this time (16UTC August 7, 2003), the minimum value of ozone is zero ppbv in 1 km resolution, and 35.6 ppbv in 3 km resolution. Thus, ozone titration still occur in 3 km resolution, while in 1 km resolution, an excess of NO molecules may cause increased loss by reactions with e.g. HO_2 and OH. This fact may explain the increase in NO_y-NO_x components (Figure 4.15b) due partly to the reactions

$$NO + NO \xrightarrow{O_2} NO_2 + NO_2 \tag{4.8}$$
$$NO + HO_2 \rightarrow NO_2 + OH \tag{4.9}$$
$$NO + OH \rightarrow HNO_2 \tag{4.10}$$
$$NO_2 + HO_2 \rightarrow HNO_4 \tag{4.11}$$
$$NO_2 + OH \rightarrow HNO_3 \tag{4.12}$$

Although our results show that there are differences in ozone caused by Lon-

don emissions when the resolution is changed, the results are inaccurate due to the lack of height distribution in the emissions causing too much NO_x to accumulate in the PBL. However, the titration occurs during the day as well when NO_x are diluted throughout a deep PBL. This fact indicates that simulations performed with correct vertical distribution of the emissions would also lead to differences between 3 km and 1 km resolutions, but maybe not to the same extent as we see here. If this is true, it would be interesting to perform simulations with higher emission resolution than 1 km, and find out if the net ozone value caused by London emissions will become even larger.

4.4 Calculations of effective emissions

Preliminary calculations of effective emissions to some of the most important components in the ozone chemistry are presented and discussed in this section. However, the method of how to implement the effective emissions into the Oslo-CTM2 model is not the purpose of this study, and is only discussed briefly. In addition, we need to emphasize that there are large uncertainties associated with the calculated values, due to lack of height information in the emissions data. Also, results from the second time period are not representative as a typical summer situation since the heat wave caused extreme weather conditions at this time.

In Calbó et al. (1998) the effective emission is defined as the sum of the true emission and net chemical production or destruction, and is given by

$$EE_i(t) = E_i(0,t) + R_i(0,t) \tag{4.13}$$

$$= M_i(t) - M_i(0) - F_i^{in}(0,t) + F_i^{out}(0,t) \tag{4.14}$$

where $EE_i(t)$ is the effective emission of species i after t hours, $E_i(0,t)$ is the true emission over time t, $R_i(0,t)$ is the amount of species added or removed in the domain by chemical reactions between $t = 0$ and t, $M_i(t)$ is the total mass of species i in the domain after t hours, $M_i(0)$ is the mass at the beginning of the run, and $F_i^{in}(0,t)$ and $F_i^{out}(0,t)$ are the total amounts of species i that have entered and exited the domain through the boundaries, respectively, over time t.

Effective emissions in this study, however, are represented as factors that are meant to be applied on the true emissions in Oslo-CTM2. In Equation (4.13), $R_i(0,t)$ represents net chemical production and loss, which is influenced by meteorological factors as well as changes in emission resolution. Since improved resolution of meteorology leads to changes in chemistry, we have chosen to take that into account in our calculations. A comparison of run AF-NF with 1 km resolution and 81 km resolution will give the quantity of error that is made when subgrid scale effects are neglected.

	Absolute difference		Relative difference	
	TP1	TP2	TP1	TP2
NO	-4.838×10^{28}	2.318×10^{28}	0.667	1.119
NO_2	-1.873×10^{29}	-1.225×10^{29}	0.662	0.876
NO_x	-2.357×10^{29}	-9.935×10^{28}	0.663	0.916
HNO_3	-1.453×10^{28}	-4.683×10^{28}	0.650	0.797
CO	-3.523×10^{29}	-3.566×10^{29}	0.844	0.924
CH_2O	-3.690×10^{27}	-1.161×10^{27}	0.811	0.970
O_3	2.080×10^{29}	6.352×10^{29}	-1.228	-0.874

Table 4.3: *Absolute differences (molecules) and relative differences (1 = no difference) between 1 km and 81 km results of abundance inside the LMA of NO, NO_2, NO_x, HNO_3, CO, CH_2O, and O_3 caused by London emissions (run AF-NF). The values are averaged over the 10 days in each of the two time periods.*

Table 4.3 gives average values for TP1 and TP2 of absolute and relative differences between the 1 km and 81 km resolution results of the chemical species NO, NO_2, NO_x, HNO_3, CO, CH_2O, and O_3 caused by London emissions (run AF-NF). It is evident from Table 4.3 that there is, with the exception of O_3, a general trend of negative absolute differences. A large part of the differences are probably caused by differences in transport out of the LMA, and, as mentioned in Section 4.3, the differences are largest between the scales 81 km and 27 km. This points to an important issue when effective emissions are to be implemented in the Oslo-CTM2. Mass needs to be conserved, meaning that the excess of molecules within the LMA have to be relocated to the surrounding grid boxes in the CTM. This problem can be solved by deriving net fluxes of chemical species in and out of the LMA volume, represented by the terms $F_i^{in}(0,t)$ and $F_i^{out}(0,t)$, respectively, in Equation (4.14).

The relative difference of e.g. NO may be expressed as

$$f_{NO} = \frac{NO^{1\text{ km}}}{NO^{81\text{ km}}} \tag{4.15}$$

where $NO^{1\text{ km}}$, and $NO^{81\text{ km}}$ are time averages of NO abundance within the LMA caused by London emissions, when resolutions of 1 km and 81 km are used, respectively. The effective emission factor, f_{NO}, can be multiplied with the true NO emission in the CTM to account for subgrid scale processes. However, a new problem arises if this method is to be used. Secondary species, e.g. O_3 and HNO_3, are not emitted directly but are produced from chemical reactions. If the concentration values of these species are to be corrected for subgrid scale effects, this must be done by other means than applying effective emission factors. One possibility is to correct the concentration values by adding the absolute difference directly into the CTM, but due to residence time, which is typically a few hours in the LMA, the time

interval between each correction needs to be considered so that the correction is not overstated. Even more challenging is to find a method of correcting the levels of chemical species that are both primary and secondary (e.g. CH_2O and NO_2).

A method that corrects for subgrid scale effects on the values of both primary and secondary species, is the one used in the studies of subsonic aircraft emissions (Petry et al., 1998; Kraabøl et al., 2000a,b, 2002; Kraabøl and Stordal, 2000). The transformation of emitted NO_x to other NO_y species and to O_3 were quantified as effective emission indices and implemented as either sources or sinks of each species in the CTM. Although this method gives reasonable results when studying emissions from aircrafts, it is probably not applicable in its current form when the ozone effect from megacity emissions is investigated. There are at least two reasons for this to be the case. First, as opposed to emissions from an aircraft which is a mobile source, megacity emissions are continuous over a limited spatial area, meaning that a megacity as a whole may be considered a stationary source. This fact complicates the calculations of effective emission indices since the NO_y species formed from NO_x emitted at a certain time will be affected by emissions at a later time. Second, the composition of emissions from a megacity is quite different than from an aircraft. Most important for ozone formation is that the exhaust from an aircraft engine has a much lower ratio of VOC to NO_x than emissions from a megacity. Accordingly, the transformation from NO_x cannot be considered alone, but VOC emissions must be taken into account as well. The chemistry associated with VOC species is complex and transformations from primary VOC species to secondary species, including ozone, is a difficult task.

Figure 4.25, and Figure 4.26 show average diurnal cycles and effective emission factors for NO, NO_2, NO_x, HNO_3, CO, CH_2O, and O_3 caused by London emissions, for TP1 and TP2, respectively. The diurnal cycles are plotted so that the reasons for different results with changes in resolution can be identified more easily. Effective emission factors are calculated as for NO in Equation (4.15). Generally, abundances of chemical species are determined by a combination of chemistry, meteorological factors, and emissions. When looking at differences between resolutions, total emissions within the LMA are the same, so changes must be due to chemistry or meteorology.

4.4.1 NO_x

The diurnal cycle of NO_x (Figures 4.25e and 4.26e) is largely controlled by emissions. Due to rush hours, the NO_x concentrations peak in the morning and late afternoon. Although NO_x are mostly emitted as NO, the NO concentration has its maximum right before noon (Figures 4.25a and 4.26a) because solar radiation reaches a maximum at midday. This causes NO_2 to be converted back to NO by Reaction (2.11).

There are differences in the NO diurnal cycle between the horizontal grid resolutions used. In TP1 (Figure 4.25a), southwesterly winds cause NO from the large emission source in the east to rapidly advect out of the LMA when 1 km resolution is used. Since the NO emissions are distributed evenly over the LMA when 81 km resolution is used, NO will have a longer residence time, and consequently larger concentrations. In TP2 (Figure 4.26a), however, easterly winds near the ground cause longer residence time with 1 km resolution than with 81 km.

4.4.2 HNO_3

During both time periods, NO_2 concentrations fall in the afternoon (Figures 4.25c and 4.26c). This decrease is caused, as mentioned above, partly by photolysis of NO_2, but also by reaction with OH (Reaction 4.4) to produce HNO_3. The afternoon decrease in NO_2 levels can be seen by a corresponding increase in HNO_3 levels (Figures 4.25g and 4.26g), but the amount of HNO_3 produced differs with a change in resolution. It seems that daytime production of HNO_3 is overestimated with 81 km resolution, especially during TP2 (Figure 4.26g). Some of the overestimation may be explained by the overestimation of NO_2, but probably a large part is caused by other changes in chemistry. At nighttime, OH is absent and HNO_3 is produced by the sequence

$$NO_2 + O_3 \rightarrow NO_3 + O_2 \tag{4.16}$$

$$NO_2 + NO_3 + M \rightleftharpoons N_2O_5 + M \tag{4.17}$$

$$N_2O_5 + H_2O(aq) \rightarrow 2HNO_3(aq) \tag{4.18}$$

where (4.18) is a heterogeneous reaction. According to the figures, differences between the resolutions are much smaller at night compared to the daytime differences in the abundance of HNO_3.

4.4.3 CO

Similar to NO_x, CO concentrations peak during rush hours, as is easily seen for TP1 in Figure 4.25i. The early morning peak is not as evident during TP2 (Figure 4.26i), probably because of less advection causing more accumulation of CO throughout the day. Because of the relatively long lifetime of CO, at least on an urban scale, the differences between resolutions indicate differences in transport. Chemical production of CO from VOCs and chemical loss by reaction with OH (Reaction (2.4)) are additional factors that could cause differences between resolutions.

4.4.4 CH_2O

The diurnal cycles shown in Figure 4.25k, and Figure 4.26k reflect the complex chemistry associated with formaldehyde. CH_2O is both a primary and a

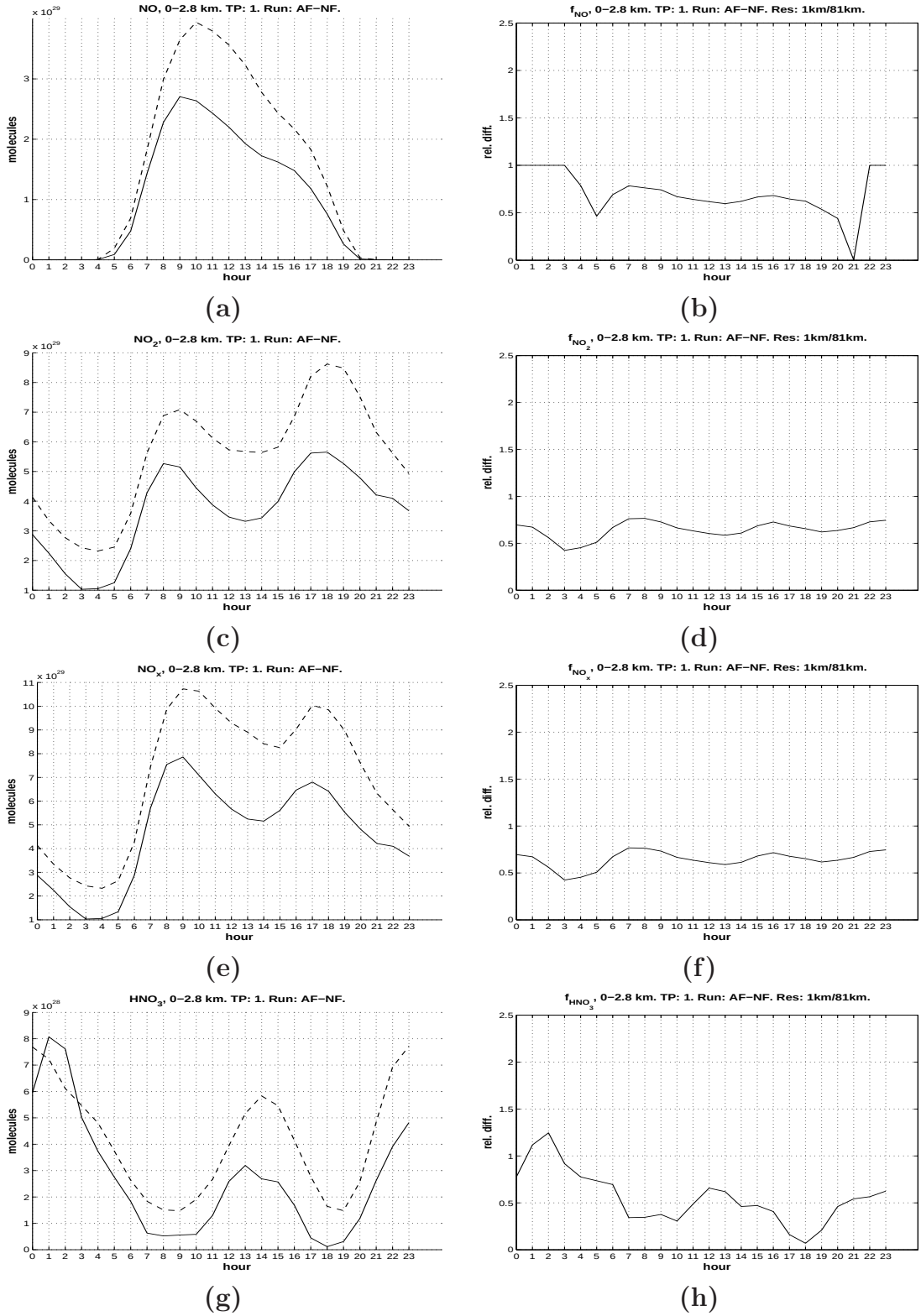

Figure 4.25: *Number of molecules in the LMA with 81 km (thick dashed line) and 1 km resolution (thin solid line) results of (a) NO, (c) NO_2, (e) NO_x, (g) HNO_3, (i) CO, (k) CH_2O, and (m) O_3 caused by London emissions (run AF-NF), and relative differences between 1 km and 81 km of (b) NO, (d) NO_2, (f) NO_x, (h) HNO_3, (j) CO, (l) CH_2O, and (n) O_3. The plots show diurnal cycles averaged over the 10 days in TP1.*

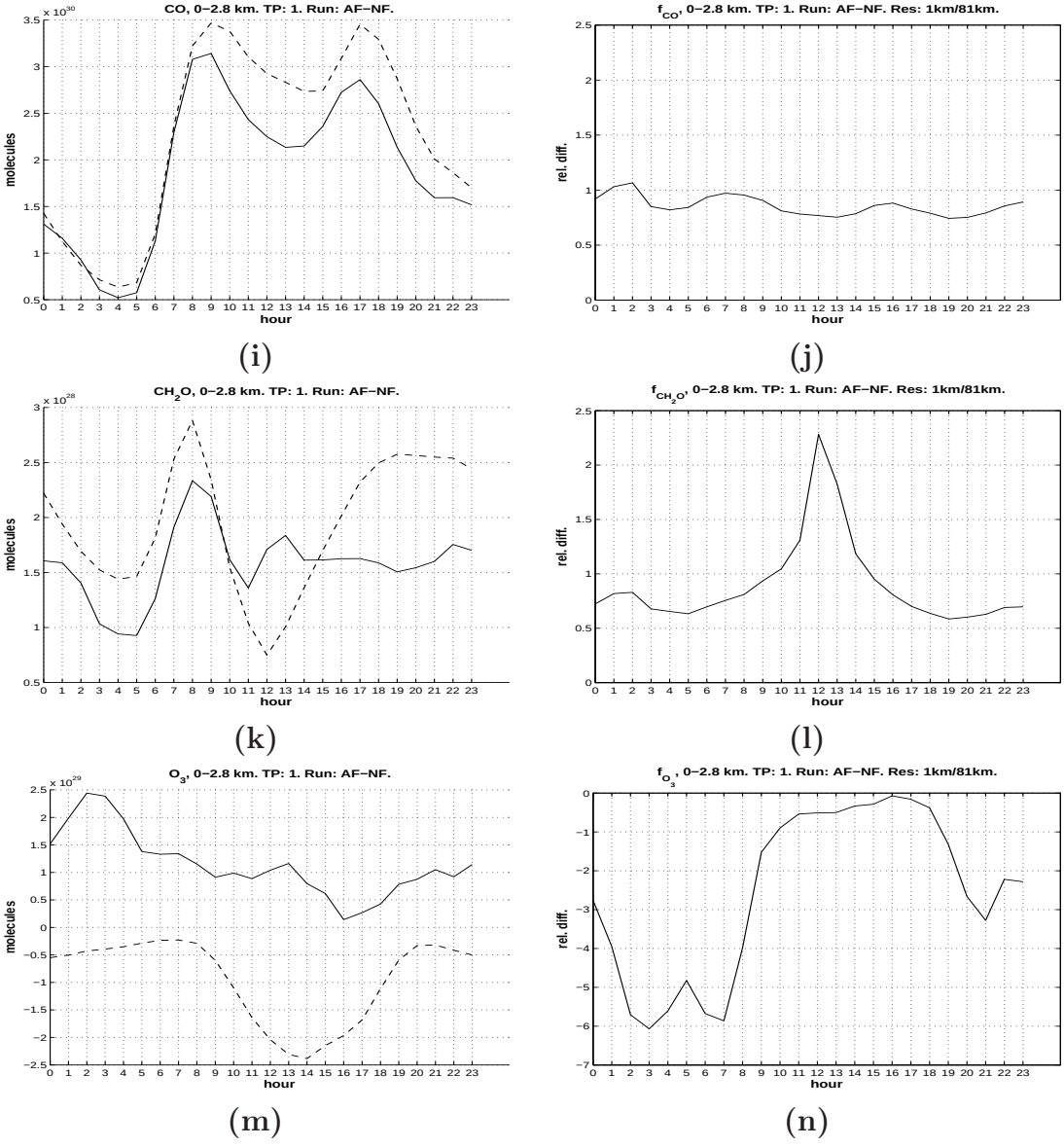

Figure 4.25: *(continued).*

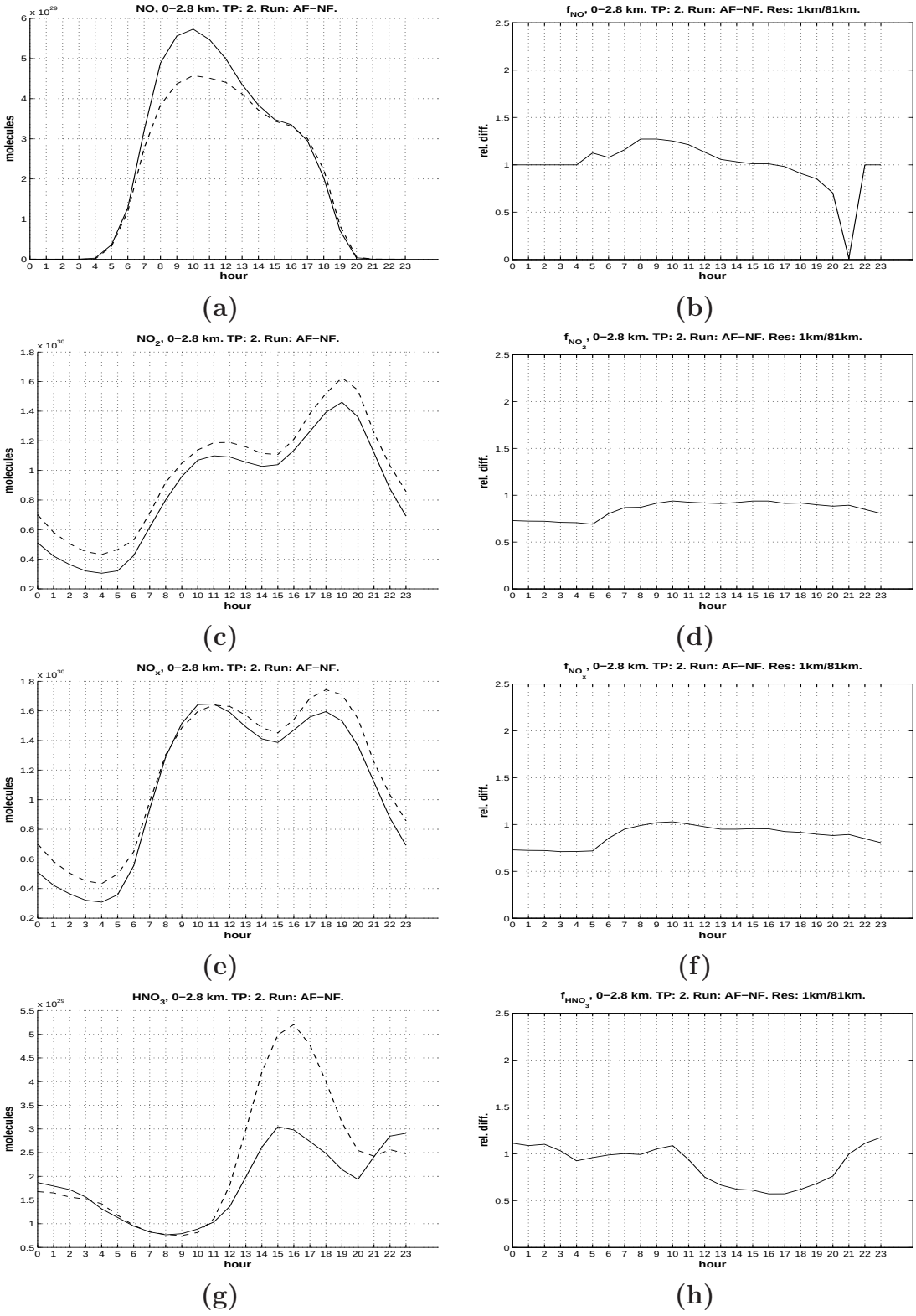

Figure 4.26: *As Figure 4.25, but for TP2.*

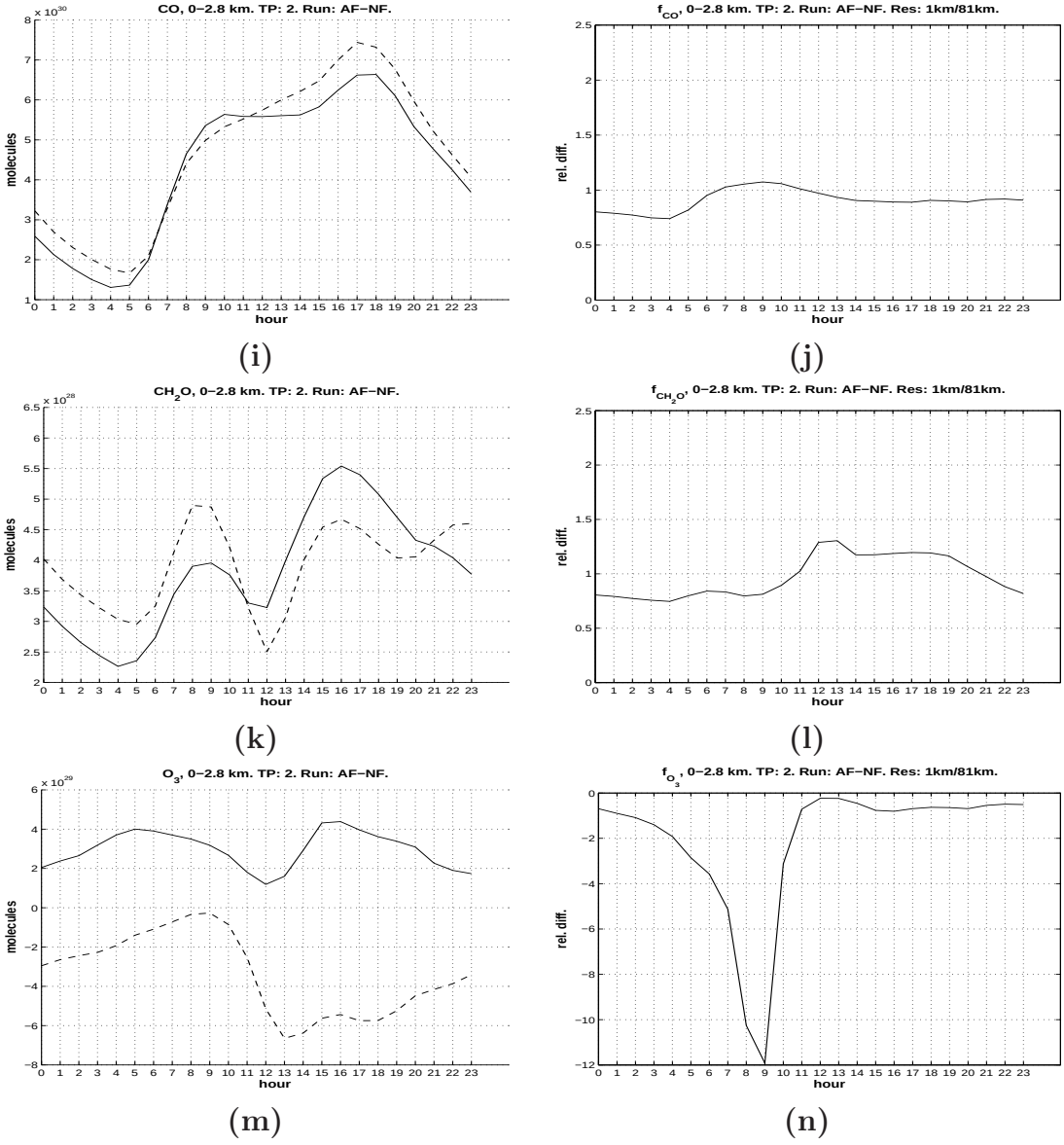

Figure 4.26: *(continued).*

secondary component, and is important as an ozone precursor. Many VOCs react to produce formaldehyde, which in turn produces ozone by a complex set of reactions initiated by CH_2O photolysis. The trend in the diurnal cycle is similar in TP1 and TP2, but the figures show that there are significant differences between the resolutions. Particularly, CH_2O levels at midday, when photochemistry is most active, are considerably larger when 1 km resolution is used compared to the 81 km results, and this difference is easily identified by the effective emission factors in Figures 4.25l and 4.26l. This fact indicates that the O_3 titration effect is not the only cause of higher ozone levels since O_3 production probably is enhanced due to a higher ratio of VOC to NO_x when the resolution is increased to 1 km.

4.4.5 O_3

Figure 4.25m, and Figure 4.26m show that net ozone caused by London emissions is consistently underestimated when 81 km resolution is used. When the resolution is higher, NO_x levels decrease more than CH_2O levels, causing less destruction and more production of ozone. During the day, the discrepancies between the resolutions are most obvious, and is probably caused by the underestimation of CH_2O in the afternoon in addition to the titration effect described in Section 4.3.

4.5 Further research

The purpose of deriving effective emissions for use in global CTM simulations is a relatively new study field, and when it comes to megacity emissions, no extensive research has been performed except in Calbó et al. (1998) and Mayer et al. (2000). As pointed out in Chapter 1, the level of urbanization is predicted to increase, and it is therefore important to investigate the regional and global impact from megacity emissions. It should be noted that the results presented here is only a first step towards improved representation of emissions in a global CTM. More research is needed in order to acquire satisfactory calculations of effective emissions that are applicable on a more general basis.

The composition of emissions vary largely from each city. In this study, the focus area is London which have a relatively large amount of NO_x emissions compared to VOC emissions. Another megacity may have a higher ratio of VOC emissions, and a different spatial distribution than London. Other factors that impact photochemistry in a city are e.g. latitude, time of year, sunlight hours, and wind patterns. It is important to focus on cities that have a growing rate of emissions, for instance in China. Although accurate emissions data are difficult to obtain, emissions from these cities will become increasingly important in the future and an effort should be made to study their impact on the regional and global scale. Obviously, it is not practicable to derive effective emissions for every megacity under all meteorological

conditions, but parameterizations can be made based on results from several WRF-Chem simulations.

While working on this study we have found at least two issues, regarding the input data and the model configuration, that may be handled differently in order to improve the model results. First, an accurate representation of emissions is important if model results are to be realistic. Height information need to be acquired or assumptions have to be made in order to realistically represent the vertical distribution of emission sources. This is especially important when it comes to emissions from point sources, which in London constitute a large amount of total emissions. Again, China is important because of the many coal-fired power plants that are built every year. Second, successful results are also dependent on accurate description of meteorology, and the boundary layer in particular. Based on the study by Misenis et al. (2006), the MYJ scheme should be considered instead of the YSU scheme.

To improve and simplify the analysis of the results there are a few issues that should be considered before model simulations are conducted. The fluxes of chemical species between grid boxes should be quantified at every time step, so that the actual transport is investigated. It would then be easier to identify transport by convection and advection, and perhaps loss by dry deposition. Additionally, more information from the chemistry scheme should be available for post-processing. At least for ozone, chemical loss and production terms should be stored to find out what causes possible changes in ozone concentrations.

Another interesting study would be to look at the effects of changing emission resolution, with the meteorological resolution kept constant at e.g. 1 km. In the study presented here, it seems that differences in meteorology accounts for most of the changes on the scales from 81 km to 3 km. If the meteorological resolution is constant, however, the impact from only chemistry changes will be identified.

Ideally, the total impact of emissions from a megacity should be studied, not only within the urban domain. As seen in Figure 4.8, emissions from London impact ozone levels far from the source region. If a longer simulation period is used, the impact would probably be on a global scale. Due to computational restraints, fine resolution simulations cannot be performed over a large area for a long time. However, if effective emission factors are applied on megacity emissions in a global CTM, this will not only alter concentrations values over the megacity itself, but a more realistic representation of concentrations will be given on the regional and global scale as well. The effective emissions calculated in this study are meant to be applied to the Oslo-CTM2 model. When this is accomplished, the regional and global effect of applying effective emissions in a global CTM can be investigated.

Chapter 5

Summary and conclusion

In this thesis, WRF-Chem simulations have been carried out in order to investigate the importance of using fine temporal and spatial model resolution when studying the effect on ozone caused by emissions from a megacity. The heat wave over Europe in August 2003 is simulated, and London has been chosen as the focus area in the analysis. To quantify the inaccuracies that are made in coarse-resolution models such as a global CTM, effective emission factors have been derived and discussed.

Results show that there are differences in chemical concentration levels associated with changes in horizontal grid resolution. The average net ozone column change due to London emissions is, within the urban domain, negative and underestimated when a square resolution of 81 km is used compared to 27 km resolution. When further decreasing the horizontal grid spacing to 9 km, and also 3 km, there were no significant changes in average column values of the chemical components included in the analysis. However, when 1 km resolution was used, net ozone caused by London emissions increased and showed a positive value in the urban domain.

There is reason to believe that the differences between 81 km and 27 km resolution can be explained by changes in meteorology rather than chemistry. A better representation of winds and boundary layer height with 27 km grid spacing causes increased transport of chemical species outwards from the urban domain. As a consequence, the level of NO_x decreases and less ozone titration occurs. On the other hand, differences between the 3 km and 1 km scales are mainly caused by nonlinearities in ozone chemistry due to better resolution of emissions data. Most likely, these changes results from a combination of at least two factors. First, there is less ozone titration in the 1 km case because O_3 mixing ratio reaches 0 ppbv at some instances, while corresponding values in the 3 km case are several ppbv. Second, the ratio of VOC to NO_x increases with better resolution, moving closer to a NO_x limited regime and thus more ozone production with 1 km resolution.

Only a few studies have been found that address issues similar to ours, and thus comparison with other work is difficult. Nevertheless, a parallel can be

drawn between our results and Cohan et al. (2006), who only found small discrepancies in regional ozone formation when results were aggregated in domains with horizontal grid resolutions of 36 km, 12 km, and 4 km. Our results show the same tendency when considering the scales 27 km, 9 km, and 3 km, while resolutions of 81 km and 1 km gave different average net ozone columns caused by London emissions. Furthermore, Mayer et al. (2000) found that implementing an urban chemistry model into a global chemistry-climate model gave more ozone production in urban domains, which is in agreement with our results for London. However, their focus was long-term climate effect, and the global tropospheric ozone mole fraction was actually lower when urban scale processes were considered in the model.

Comparisons between measurements and model results of CO, NO, NO_2, NO_x, and O_3 have been performed for several stations in London. The model performs relatively well in the first half of the simulation period, while major discrepancies have been revealed for the latter ten days. The deviations are most evident when it comes to the levels of NO_x, and can for the most part be explained by lack of height information in the emissions, especially for one specific point source. A shift in wind direction and lighter wind conditions during the second half of the simulation period cause the discrepancies during this time. Consequently, ozone levels are underestimated during the day, while, due to other factors, nighttime levels of ozone are overestimated in the model. Because of the discrepancies, some level of uncertainty should be considered when drawing conclusions from our model results. Furthermore, the model has been run in forecast mode without any re-initialization since the start of the simulation period, and towards the latter part of the period its predicting ability may be reduced.

For simulations in the London area it seems that a horizontal grid spacing of $\sim$27 km is necessary in order to resolve meteorological processes at a reasonable level. In cities where variations in the terrain may induce local winds, an even better resolution should be considered. Although our results show that the differences in ozone column values with changes in resolutions are relatively small, the errors may become large if a global CTM used for climate predictions several years into the future neglects urban scale processes for every city at every time step. Furthermore, we assume that CTM simulations are carried out using a horizontal grid resolution of $1^\circ \times 1^\circ$, while a resolution of $2.8^\circ \times 2.8^\circ$ is more typically used in climate studies. The inaccuracies are probably even larger if such a coarse resolution is used.

Despite the uncertainties in the model results, we think that our analysis shows the importance of large point sources when it comes to nonlinearities in the ozone chemistry. To include these effects in a global CTM, a parameterization representing the nonlinearities should be made, or point sources should be treated specifically in the model.

The effective emission factors presented in this study are, in a long-term perspective, meant to be implemented in Oslo-CTM2. However, further work remains before the effective emissions can be applied successfully. Most importantly, a method of implementing the effective emissions needs to be prepared, and fluxes in and out of the urban domain must be calculated due to mass conservation.

When a global CTM simulation is carried out, limited computer capacity prevents effective emissions to be calculated directly for every megacity using a three-dimensional urban scale model. Nevertheless, results from this study suggest that urban scale processes should be taken into consideration in coarse-resolution models. We would probably achieve quite good results by increasing the resolution in urban domains to $\sim$27 km, and to treat large point sources specifically. This approach should be a good compromise between computer efficiency and accurate description of subgrid scale effects, and could be a first step towards the goal of accurately describing urban scale processes in coarse-resolution CTMs.

Appendix A

Organic chemistry classes in RADM2

The organic chemistry in RADM2 is represented through a reactivity aggregated molecular approach (Middleton and Stockwell, 1990). Organic compounds with similar reactivity are grouped together into a limited number of classes in the RADM2 chemistry scheme. The emissions categories for each RADM2 class are shown in Table A.1 for the most emitted NMVOCs.

RADM2 Class	**Emissions Category**	
ETH	Ethane	
HC3	Propane	Alkanes (0.25-0.50)
	Acetylene	Haloalkenes
	Others (<0.25 react)	Others (0.25-0.50 react)
HC5	Alkanes (0.50-1.00)	Others (0.5-1.0 react)
HC8	Alkanes (1.00-2.00)	Alkanes (>2.00)
	Alkane/Aromatic Mix	Others (>1.00 react)
OL2	Ethene	
OLT	Propene	Alkenes (Primary)
	Alkenes (Prim/Inter Mix)	Styrenes
OLI	Alkenes (Internal)	Alkenes (Prim/Inter Mix)
TOL	Benzene, Halobenzenes	Aromatics (<2 react)
	Styrenes	
XYL	Aromatics (>2 react)	Alkane/Aromatic Mix
CSL	Phenols and Cresols	
HCHO	Formaldehyde	
ALD	Higher Aldehydes	
KET	Acetone	Higher Ketones
ORA2	Organic Acids	

Table A.1: *Middleton and Stockwell (1990)*

Appendix B

Reactions in RADM2

The reactions listed below are included in the RADM2 chemistry scheme which we use in WRF-Chem. Organic chemistry is represented by 26 stable species and 16 peroxy radicals. The RADM2 classes for the most emitted NMVOCs are shown in Table A.1.

Photolysis reactions

$NO_2 + h\nu \rightarrow O(^3P) + NO$
$O_3 + h\nu \rightarrow O(^1D) + O_2$
$O_3 + h\nu \rightarrow O(^3P) + O_2$
$HONO + h\nu \rightarrow OH + NO$
$HNO_3 + h\nu \rightarrow OH + NO_2$
$HNO_4 + h\nu \rightarrow 0.65\ HO_2 + 0.65\ NO_2 + 0.35\ OH + 0.35\ NO_3$
$NO_3 + h\nu \rightarrow NO + O_2$
$NO_3 + h\nu \rightarrow NO_2 + O(^3P)$
$H_2O_2 + h\nu \rightarrow OH + OH$
$CH_2O + h\nu \rightarrow CO + H_2$
$CH_2O + h\nu \rightarrow HO_2 + HO_2 + CO$
$ALD + h\nu \rightarrow MO_2 + HO_2 + CO$
$OP1 + h\nu \rightarrow CH_2O + HO_2 + OH$
$OP2 + h\nu \rightarrow ALD + HO_2 + OH$
$PAA + h\nu \rightarrow MO_2 + OH$
$KET + h\nu \rightarrow ACO_3 + ETHP$
$GLY + h\nu \rightarrow 0.13\ CH_2O + 1.87\ CO + 0.87\ H_2$
$GLY + h\nu \rightarrow 0.45\ CH_2O + 1.55\ CO + 0.80\ HO_2 + 0.15\ H_2$
$MGLY + h\nu \rightarrow ACO_3 + HO_2 + CO$
$DCB + h\nu \rightarrow HO_2 + TCO_3$
$ONIT + h\nu \rightarrow 0.20\ ALD + 0.80\ KET + HO_2 + NO_2$

Chemical tropospheric reactions

$O(^3P) + M \rightarrow O_3$
$O(^3P) + NO_2 \rightarrow NO + O_2$
$O(^1D) + M \rightarrow O(^3P)$
$O(^1D) + H_2O \rightarrow OH + OH$
$O_3 + NO \rightarrow NO_2 + O_2$
$O_3 + OH \rightarrow HO_2 + O_2$
$O_3 + HO_2 \rightarrow OH + 2.00\ O_2$
$HO_2 + NO \rightarrow NO_2 + OH$
$HO_2 + NO_2 \rightarrow HNO_4$
$HNO_4 \rightarrow HO_2 + NO_2$
$HO_2 + HO_2 \rightarrow H_2O_2$
$HO_2 + HO_2 + H_2O \rightarrow H_2O_2$
$H_2O_2 + OH \rightarrow HO_2 + H_2O$
$NO + OH \rightarrow HONO$
$NO + NO + M \rightarrow NO_2 + NO_2$
$O_3 + NO_2 \rightarrow NO_3$
$NO_3 + NO \rightarrow NO_2 + NO_2$
$NO_3 + NO_2 \rightarrow NO + NO_2 + O_2$
$NO_3 + HO_2 \rightarrow HNO_3 + O_2$
$NO_3 + NO_2 \rightarrow N_2O_5$
$N_2O_5 \rightarrow NO_2 + NO_3$
$N_2O_5 \rightarrow 2.00\ HNO_3$
$OH + NO_2 \rightarrow HNO_3$
$OH + HNO_3 \rightarrow NO_3 + H_2O$
$OH + HNO_4 \rightarrow NO_2 + H_2O + O_2$
$OH + HO_2 \rightarrow H_2O + O_2$
$OH + SO_2 \rightarrow SULF + HO_2$
$CO + OH \rightarrow HO_2 + CO_2$
$CH_4 + OH \rightarrow MO_2 + H_2O$
$ETH + OH \rightarrow ETHP + H_2O$
$HC3 + OH \rightarrow 0.83\ HC3P + 0.17\ HO_2 + 0.009\ CH_2O + 0.075\ ALD + 0.025\ KET + H_2O$
$HC5 + OH \rightarrow HC5P + 0.25\ XO_2 + H_2O$
$HC8 + OH \rightarrow HC8P + 0.75\ XO_2 + H_2O$
$OL2 + OH \rightarrow OL2P$
$OLT + OH \rightarrow OLTP$
$OLI + OH \rightarrow OLIP$
$TOL + OH \rightarrow 0.75\ TOLP + 0.25\ CSL + 0.25\ HO_2$
$XYL + OH \rightarrow 0.83\ XYLP + 0.17\ CSL + 0.17\ HO_2$
$CSL + OH \rightarrow 0.10\ HO_2 + 0.90\ XO_2 + 0.90\ TCO_3\text{-}0.90\ OH$

$CH_2O + OH \rightarrow HO_2 + CO + H_2O$
$ALD + OH \rightarrow ACO_3 + H_2O$
$KET + OH \rightarrow KETP + H_2O$
$GLY + OH \rightarrow HO_2 + 2.00\ CO + H_2O$
$MGLY + OH \rightarrow ACO_3 + CO + H_2O$
$DCB + OH \rightarrow TCO_3 + H_2O$
$OP1 + OH \rightarrow 0.50\ MO_2 + 0.50\ CH_2O + 0.50\ OH$
$OP2 + OH \rightarrow 0.50\ HC3P + 0.50\ ALD + 0.50\ OH$
$PAA + OH \rightarrow ACO_3 + H_2O$
$PAN + OH \rightarrow CH_2O + NO_3 + XO_2$
$ONIT + OH \rightarrow HC3P + NO_2$
$ISO + OH \rightarrow OLTP$
$ACO_3 + NO_2 \rightarrow PAN$
$PAN \rightarrow ACO_3 + NO_2$
$TCO_3 + NO_2 \rightarrow TPAN$
$TPAN \rightarrow TCO_3 + NO_2$
$MO_2 + NO \rightarrow CH_2O + HO_2 + NO_2$
$HC3P + NO \rightarrow 0.75\ ALD + 0.25\ KET + 0.09\ CH_2O + 0.036\ ONIT + 0.964\ NO_2 + 0.964\ HO_2$
$HC5P + NO \rightarrow 0.38\ ALD + 0.69\ KET + 0.08\ ONIT + 0.92\ NO_2 + 0.92\ HO_2$
$HC8P + NO \rightarrow 0.35\ ALD + 1.06\ KET + 0.04\ CH_2O + 0.24\ ONIT + 0.76\ NO_2 + 0.76\ HO_2$
$OL2P + NO \rightarrow 1.60\ CH_2O + HO_2 + NO_2 + 0.20\ ALD$
$OLTP + NO \rightarrow ALD + CH_2O + HO_2 + NO_2$
$OLIP + NO \rightarrow HO_2 + 1.45\ ALD + 0.28\ CH_2O + 0.10\ KET + NO_2$
$ACO_3 + NO \rightarrow MO_2 + NO_2$
$TCO_3 + NO \rightarrow NO_2 + 0.92\ HO_2 + 0.89\ GLY + 0.11\ MGLY + 0.05\ ACO_3 + 0.95\ CO + 2.00\ XO_2$
$TOLP + NO \rightarrow NO_2 + HO_2 + 0.17\ MGLY + 0.16\ GLY + 0.70\ DCB$
$XYLP + NO \rightarrow NO_2 + HO_2 + 0.45\ MGLY + 0.806\ DCB$
$ETHP + NO \rightarrow ALD + HO_2 + NO_2$
$KETP + NO \rightarrow MGLY + NO_2 + HO_2$
$OLN + NO \rightarrow CH_2O + ALD + 2.00\ NO_2$

$CH_2O + NO_3 \rightarrow HO_2 + HNO_3 + CO$
$ALD + NO_3 \rightarrow ACO_3 + HNO_3$
$GLY + NO_3 \rightarrow HNO_3 + HO_2 + 2.00\ CO$
$MGLY + NO_3 \rightarrow HNO_3 + ACO_3 + CO$
$DCB + NO_3 \rightarrow HNO_3 + TCO_3$
$CSL + NO_3 \rightarrow HNO_3 + XNO_2 + 0.50\ CSL$
$OL2 + NO_3 \rightarrow OLN$
$OLT + NO_3 \rightarrow OLN$
$OLI + NO_3 \rightarrow OLN$
$ISO + NO_3 \rightarrow OLN$
$OL2 + O_3 \rightarrow CH_2O + 0.42\ CO + 0.40\ ORA1 + 0.12\ HO_2$
$OLT + O_3 \rightarrow 0.53\ CH_2O + 0.50\ ALD + 0.33\ CO + 0.20\ ORA1 + 0.20\ ORA2 + 0.23\ HO_2 + 0.22\ MO_2 + 0.10\ OH + 0.06\ CH_4$
$OLI + O_3 \rightarrow 0.18\ CH_2O + 0.72\ ALD + 0.10\ KET + 0.23\ CO + 0.06\ ORA1 + 0.29\ ORA2 + 0.09\ CH_4 + 0.26\ HO_2 + 0.31\ MO_2 + 0.14\ OH$
$ISO + O_3 \rightarrow 0.53\ CH_2O + 0.50\ ALD + 0.33\ CO + 0.20\ ORA1 + 0.20\ ORA2 + 0.23\ HO_2 + 0.22\ MO_2 + 0.10\ OH$
$HO_2 + MO_2 \rightarrow OP1$
$HO_2 + ETHP \rightarrow OP2$
$HO_2 + HC3P \rightarrow OP2$
$HO_2 + HC5P \rightarrow OP2$
$HO_2 + HC8P \rightarrow OP2$
$HO_2 + OL2P \rightarrow OP2$
$HO_2 + OLTP \rightarrow OP2$
$HO_2 + OLIP \rightarrow OP2$
$HO_2 + KETP \rightarrow OP2$
$HO_2 + ACO_3 \rightarrow PAA$
$HO_2 + TOLP \rightarrow OP2$
$HO_2 + XYLP \rightarrow OP2$
$HO_2 + TCO_3 \rightarrow OP2$
$HO_2 + OLN \rightarrow ONIT$
$MO_2 + MO_2 \rightarrow 1.50\ CH_2O + HO_2$
$MO_2 + ETHP \rightarrow 0.75\ CH_2O + HO_2 + 0.75\ ALD$
$MO_2 + HC3P \rightarrow 0.75\ CH_2O + HO_2 + 0.15\ ALD + 0.6\ KET$

MO_2 + HC5P → 0.77 CH_2O + HO_2
+ 0.41 ALD + 0.75 KET
MO_2 + HC8P → 0.80 CH_2O + HO_2
+ 0.46 ALD + 1.39 KET
MO_2 + OL2P → 1.55 CH_2O + HO_2
+ 0.35 ALD
MO_2 + OLTP → 1.25 CH_2O + HO_2
+ 0.75 ALD
MO_2 + OLIP → 0.89 CH_2O + HO_2
+ 0.725 ALD + 0.55 KET
MO_2 + KETP → 0.75 CH_2O + HO_2
+ 0.75 MGLY
MO_2 + ACO_3 → CH_2O + 0.50 HO_2
+ 0.50 MO_2 + 0.50 ORA2
MO_2 + TOLP → CH_2O + 2.00 HO_2
+ 0.17 MGLY + 0.16 GLY
+ 0.70 DCB
MO_2 + XYLP → CH_2O + 2.00 HO_2
+ 0.45 MGLY + 0.806 DCB
MO_2 + TCO_3 → 0.50 CH_2O + 0.50 ORA2
+ 0.445 GLY + 0.055 MGLY
+ 0.025 ACO_3 + 0.475 CO
+ 0.46 HO_2 + XO_2
ETHP + ACO_3 → ALD + 0.50 HO_2
+ 0.50 MO_2 + 0.50 ORA2
HC3P + ACO_3 → 0.2 ALD + 0.8 KET
+ 0.50 HO_2 + 0.50 ORA2
+ 0.50 MO_2
HC5P + ACO_3 → 0.14 ALD + 0.86 KET
+ 0.50 HO_2 + 0.50 ORA2
+ 0.50 MO_2
HC8P + ACO_3 → 0.1 ALD + 0.9 KET
+ 0.50 HO_2 + 0.50 ORA2
+ 0.50 MO_2
OL2P + ACO_3 → 0.80 CH_2O + 0.60 ALD
+ 0.50 HO_2 + 0.50 ORA2
+ 0.50 MO_2
OLTP + ACO_3 → ALD + 0.50 CH_2O
+ 0.50 HO_2 + 0.50 ORA2
+ 0.50 MO_2
OLIP + ACO_3 → 0.725 ALD + 0.55 KET
+ 0.14 CH_2O + 0.50 HO_2
+ 0.50 MO_2 + 0.50 ORA2
KETP + ACO_3 → MGLY + 0.50 HO_2
+ 0.50 ORA2 + 0.50 MO_2

$ACO_3 + ACO_3 \rightarrow 2.00\ MO_2$
$ACO_3 + TOLP \rightarrow 0.8\ MGLY + 0.2\ GLY$
$+ 1.00\ DCB + HO_2 + MO_2$
$ACO_3 + XYLP \rightarrow MO_2 + 1.00\ MGLY$
$+ 1.00\ DCB + HO_2$
$ACO_3 + TCO_3 \rightarrow MO_2 + 0.92\ HO_2$
$+ 0.89\ GLY + 0.11\ MGLY$
$+ 0.05\ ACO_3 + 0.95\ CO$
$+ 2.00\ XO_2$
$XO_2 + HO_2 \rightarrow OP2$
$XO_2 + MO_2 \rightarrow CH_2O + HO_2$
$XO_2 + ACO_3 \rightarrow MO_2$
$XO_2 + XO_2 \rightarrow H_2O$
$XO_2 + NO \rightarrow NO_2$
$XNO_2 + NO_2 \rightarrow ONIT$
$XNO_2 + HO_2 \rightarrow OP2$
$XNO_2 + MO_2 \rightarrow CH_2O + HO_2$
$XNO_2 + ACO_3 \rightarrow MO_2$
$XNO_2 + XNO_2 \rightarrow H_2$
$MO_2 + OLN \rightarrow 1.75\ CH_2O + .5\ HO_2$
$+ ALD + NO_2$
$ACO_3 + OLN \rightarrow CH_2O + ALD + 0.50\ ORA2$
$+ NO_2 + 0.50\ MO_2$
$OLN + OLN \rightarrow 2.00\ CH_2O + 2.00\ ALD$
$+ 2.00\ NO_2$

Bibliography

Arya, S.P.S. (1988) *I*ntroduction to Micrometeorology (Academic Press, San Diego). Pp. 307.

Berntsen, Terje and Isaksen, Ivar S. A. (1997) *A* global 3-D chemical transport model for the troposphere, 1, Model description and CO and ozone results. Journal of Geophysical Research, Vol. 102(D17): p. 21 239–21 280.

Brasseur, G. P.; Orlando, J. J. and Tyndall, G. S. (1999) *A*tmospheric Chemistry and Global Change (Oxford University Press).

Calbó, J.; Pan, W.; Webster, M.; Prinn, R. and McRae, G. J. (1998) *P*arameterization of urban subgrid scale processes in global atmospheric chemistry models. Journal of Geophysical Research, Vol. 103(D3): p. 3437–3451.

Cohan, D. S.; Hu, Y. and Russell, A. G. (2006) *D*ependence of ozone sensitivity analysis on grid resolution. Atmospheric Environment, Vol. 40: p. 126–135.

DEFRA (2007) *U*K National Air Quality Archive. http://www.airquality.co.uk/archive/index.php.

DEFRA (2008) *U*K National Air Quality Archive: Data. http://www.airquality.co.uk/archive/data_and_statistics_home.php.

Dore, C. J.; Watterson, J. D.; Murrells, T. P.; Passant, N. R.; Hobson, M. M.; Choudrie, S. L.; Thistlethwaite, G.; Wagner, A.; Jackson, J.; Li, Y.; Bush, T.; King, K. R.; Norris, J.; Coleman, P. J.; Walker, C.; Stewart, R. A.; Goodwin, J. W. L.; Tsagatakis, I.; Conolly, C.; Downes, M. K.; Brophy, N. and Hann, M. R. (2007) *U*K Emissions of Air Pollutants 1970 to 2005. Technical report, AEA Energy and Environment.

Gauss, Michael; Isaksen, Ivar S. A.; Wong, S. and Wang, W. C. (2003) *I*mpact of H2O emissions from cryoplanes and kerosene aircraft on the atmosphere. Journal of Geophysical Research, Vol. 108(D10): p. 4304.

Geng, F.; Zhao, C.; Tang, X.; Lu, G. and Tie, X. (2007) *A*nalysis of ozone and VOCs measured in Shanghai: A case study. Atmospheric Environment, Vol. 41: p. 989–1001.

Gillani, N. V. and Pleim, J. E. (1996) *S*ub-grid-scale features of anthropogenic emissions of NO_x and VOC in the context of regional Eulerian models. Atmospheric Environment, Vol. 30(12): p. 2043–2059.

Grell, Georg A.; Peckham, Steven E.; Schmitz, Rainer; McKeen, Stuart A.; Frost, Gregory; Skamarock, William C. and Eder, Brian (2005) *F*ully coupled "online" chemistry within the WRF model. Atmospheric Environment, Vol. 39: p. 6957–6975.

Guenther, A.B.; Zimmerman, P.R. and Wildermuth, M. (1994) *N*atural volatile organic compound emission rate estimates for US woodland landscapes. Atmospheric Environment, Vol. 28: p. 1197–1210.

Guenther, Alex B.; Zimmerman, Patrick R.; Harley, Peter C.; Monson, Russell K. and Fall, Ray (1993) *I*soprene and monoterpene emission rate variability - Model evaluations and sensitivity analyses. Journal of Geophysical Research, Vol. 98(D7): p. 12 609–12 617.

Hesstvedt, E.; Hov, Ø. and Isaksen, I. S. A. (1978) *Q*uasi-steady-state approximations in air pollution modelling: Comparison of two numerical schemes for oxidant prediction. Int. J. Chem. Kinet., Vol. 10: p. 971–994.

Hov, Ø. (2007) *D*ispersion of air pollutions. Lecture notes from course at University of Oslo.

IPCC (2007) *S*ummary for Policymakers. In *C*limate Change 2007: The Physical Science Basis. Contribution of Working Group I to the Fourth Assessment Report of the Intergovernmental Panel on Climate Change [Solomon, S., D. Qin, M. Manning, Z. Chen, M. Marquis, K.B. Averyt, M. Tignor and H.L. Miller (eds.)] (Cambridge University Press, Cambridge, United Kingdom and New York, NY, USA).

Jacob, Daniel J. (1999) *I*ntroduction to Atmospheric Chemistry (Princeton University Press).

Jacobson, Mark Z. (2005) *F*undamentals of Atmospheric Modeling (Cambridge University Press), 2nd edition.

Junge, C. E. (1963) *A*ir Chemistry and Radioactivity (Academic Press).

Kraabøl, A. G.; Flatøy, F. and Stordal, F. (2000a) *I*mpact of NO_x emissions from subsonic aircraft: Inclusion of plume processes in a three-dimensional model covering Europe, North America, and the North Atlantic. Journal of Geophysical Research, Vol. 105(D3): p. 3573–3581.

Kraabøl, A. G.; Konopka, P.; Stordal, F. and Schlager, H. (2000b) *M*odeling chemistry in aircraft plumes 1: comparison with observations and evaluation of a layered approach. Atmospheric Environment, Vol. 34: p. 3939–3950.

Kraabøl, A. G. and Stordal, F. (2000) *M*odeling chemistry in aircraft plumes 2: the chemical conversion of NO_x to reservoir species under different conditions. Atmospheric Environment, Vol. 34: p. 3951–3962.

Kraabøl, A.G.; Berntsen, T. K.; Sundet, J. K. and Stordal, F. (2002) *I*mpact of NO_x emissions from subsonic aircraft in a global three-dimensional chemistry transport model including plume processes. Journal of Geophysical Research, Vol. 107(D22): p. 4655.

Madronich, Sasha (1987) *P*hotodissociation in the atmosphere. I - Actinic flux and the effects of ground reflections and clouds. Journal of Geophysical Research, Vol. 92: p. 9740–9752.

Mayer, M.; Wang, C.; Webster, M. and Prinn, R. G. (2000) *L*inking Local Air Pollution to Global Chemistry and Climate. Journal of Geophysical Research, Vol. 105(D18): p. 22,869–22,896.

Middleton, P. and Stockwell, W. R. (1990) *A*ggregation and analysis of volatile organic compound emissions for regional modeling. Atmospheric Environment, Vol. 24A(5): p. 1107–1133.

Misenis, C.; Hu, X.; Krishnan, S. and Zhang, Y. (2006) *S*ensitivity of WRF/Chem predictions to meteorological schemes. 14th Joint Conference on the Applications of Air Pollution Meteorology with the Air and Waste Management Association.

Peckham, Steven E.; Grell, Georg A.; Fast, Jerome D.; Gustafson, William I.; Ghan, Steven J.; Zaveri, Rahul; Easter, Richard C.; Barnard, James; Chapman, Elaine; Schmitz, Rainer and Salzmann, Marc (2006) *W*RF/Chem Version 2.2 User's Guide DRAFT.

Petry, H.; Hendricks, J.; Möllhoff, M.; Lippert, E.; Meier, A. and Ebel, A. (1998) *C*hemical conversion of subsonic aircraft emissions in the dispersing plume: Calculation of effective emissions indices. Journal of Geophysical Research, Vol. 103(D5): p. 5759–5772.

RETRO (2006) *R*Eanalysis of the TROpospheric chemical composition over the past 40 years. http://retro.enes.org/.

Sanders, R. (1999) *C*ompilation of Henry's Law Constants for Inorganic and Organic Species of Potential Importance in Environmental Chemistry (Version 3). http://www.henrys-law.org.

Schoenemeyer, T.; Richter, K. and Smiatek, G. (1997) *V*orstudie uber ein raumlich und zeitlich aufgelostes Kataster anthropogener und biogener Emissionenn fuer Bayern mit Entwicklung eines Prototyps und Anwendung fur Immissionsprognosen. Abschluss bericht an das Bayerische Landesamt fur Umweltschutz. Fraunhofer-Institut fuer Atmosphaerische Umweltforschung, Garmisch-Partenkirchen.

Sillman, S. (1995) *T*he use of NO_y, H_2O_2, and HNO_3 as indicators for ozone-NO_x-hydrocarbon sensitivity in urban locations. Journal of Geophysical Research, Vol. 100(D7): p. 14,175–14,188.

Simpson, D.; Guenther, A.; Hewitt, C. N. and Steinbrecher, R. (1995) *B*iogenic emissions in Europe. 1. Estimates and uncertainties.. Journal of Geophysical Research, Vol. 10D: p. 22 875–22 890.

Skamarock, William C.; Klemp, Joseph B.; Dudhia, Jimy; Gill, David O.; Barker, Dale M.; Wang, Wei and Powers, Jordan G. (2007) *A* Description of the Advanced Research WRF Version 2. Technical report, Mesoscale and Microscale Meteorology Division, National Center for Atmospheric Research, Boulder, Colorado, USA.

Sokhi, R. S.; José, R. S.; Kitwiroon, N.; Fragkou, E.; Pérez, J. L. and Middleton, D. R. (2006) *P*rediction of ozone levels in London using the MM5-CMAQ modelling system. Environmental Modelling and Software.

Stedman, J. R. (2004) *T*he predicted number of air pollution related deaths in the UK during the August 2003 heatwave. Atmospheric Environment, Vol. 38: p. 1087–1090.

Stockwell, William R.; Middleton, Paulette and Chang, Julius S. (1990) *T*he second generation regional acid deposition model chemical mechanism for regional air quality modeling. Journal of Geophysical Research, Vol. 95: p. 16 343–16 367.

Stordal, Frode and Hov, Øystein (1993) *L*uftforurensninger (Universitetsforlaget).

Søvde, O. A.; Gauss, M.; Smyshlyaev, S. P. and Isaksen, I. S. A. (2008) *E*valuation of the chemical transport model Oslo CTM2 with focus on Arctic winter ozone depletion. Accepted for Journal of Geophysical Research.

Tie, Xuexi; Madronich, Sasha; Walters, Stacy; Zhang, Renyi; Rasch, Phil and Collins, William (2003) *E*ffect of clouds on photolysis and oxidants in the troposphere. Journal of Geophysical Research, Vol. 108.

UN, DESA, Population Division (2006) *W*orld Population Prospects: The 2005 Revision. United Nations Publication.

Wang, Wei; Barker, Dale; Bray, John; Bruyère, Cindy; Duda, Michael; Dudhia, Jimy; Gill, Dave and Michalakes, John (2007) *A*RW Version 2 Modeling System User's Guide. Mesoscale and Microscale Meteorology Division, National Center for Atmospheric Research, Boulder, Colorado, USA.

Wesley, M.L. (1989) *P*arameterization of surface resistance to gaseous dry deposition in regional numerical models. Atmospheric Environment, Vol. 16: p. 1293–1304.

Wicker, L.J. and Skamarock, W.C. (2002) *T*ime splitting methods for elastic models using forward time schemes. Monthly Weather Review, Vol. 130: p. 2088–2097.

Wild, O.; Zhu, X. and Prather, M. J. (2000) *F*ast-J: Accurate Simulation of In- and Below-Cloud Photolysis in Tropospheric Chemical Models. Journal of Atmospheric Chemistry, Vol. 37: p. 245–282.

Zipser, E. J. (1977) *M*esoscale and Convective-Scale Downdrafts as Distinct Components of Squall-Line Structure. Monthly Weather Review, Vol. 105: p. 1568–1589.